Flash Kinetics in Liquefied Noble Gases: Studies of Alkane Activation and Ligand Dynamics at Rhodium Carbonyl Centers, and a Search for Xenon-Carbene Adducts

by

Jake Simon Yeston

A.B. (Harvard University) 1996

A dissertation submitted in partial satisfaction of the

requirements for the degree of

Doctor of Philosophy

in

Chemistry

in the

GRADUATE DIVISION

of the

UNIVERSITY OF CALIFORNIA, BERKELEY

Committee in charge:

Professor Robert G. Bergman, Co-Chair
Professor C. Bradley Moore, Co-Chair
Professor Enrique Iglesia

Fall 2001

Abstract

Flash Kinetics in Liquefied Noble Gases: Studies of Alkane Activation and Ligand Dynamics at Rhodium Carbonyl Centers, and a Search for Xenon-Carbene Adducts

by

Jake Simon Yeston

Doctor of Philosophy in Chemistry

University of California, Berkeley

Professor Robert G. Bergman, Co-Chair

Professor C. Bradley Moore, Co-Chair

Chapter 1. A general introduction is given to place the subsequent chapters in context for the nonspecialist.

Chapter 2. Results are presented from a low temperature infrared (IR) flash kinetic study of C-H bond activation via photoinduced reaction of Cp*Rh(CO)$_2$ (**1**) with linear and cyclic alkanes in liquid krypton and liquid xenon solution. No reaction was observed with methane; for all other hydrocarbons studied, the rate law supports fragmentation of the overall reaction into an alkane binding step followed by an oxidative addition step. For the binding step, larger alkanes within each series (linear and cyclic) interact more strongly than smaller alkanes with the Rh center. The second step, oxidative addition of the C-H bond across Rh, exhibits very little variance in the series of linear alkanes, while in the cyclic series the rate decreases with increasing alkane size.

Chapter 3. Results are presented from an IR flash kinetic study of the photoinduced chemistry of Tp*Rh(CO)$_2$ (**5**; Tp* = hydridotris(3,5-dimethylpyrazolyl)borato) in liquid xenon solution at –50 °C. IR spectra of the solution taken 2 μs after 308 nm photolysis exhibit two transient bands at 1972-1980 cm^{-1} and 1992-2000 cm^{-1}, respectively. These bands were assigned to (η^3-Tp*)Rh(CO)•Xe and (η^2-Tp*)Rh(CO)•Xe solvates on the basis of companion studies using Bp*Rh(CO)$_2$ (**9**; Bp* = dihydridobis(3,5-dimethyl pyrazolyl)borato). Preliminary kinetic data for reaction of **5** with cyclohexane in xenon solution indicate that both transient bands still appear and that their rates of decay correlate with formation of the product Tp*Rh(CO)(C$_6$H$_{11}$)(H).

Chapter 4. The preparation and reactivity of the new complex Bp*Rh(CO)(pyridine) (**11**) are described. The complex reacts with CH$_3$I to yield the novel Rh carbene hydride complex HB(Me$_2$pz)$_2$Rh(H)(I)(C$_5$H$_5$N)(C(O)Me) (**12**), resulting from formal addition of CH$_3$I across the Rh-C bond concomitant with hydride transfer from B to Rh. Thermolysis of **12** induces migration of the Rh hydride to the α-carbon to give HB(Me$_2$pz)$_2$Rh(I)(C$_5$H$_5$N)(CH(O)Me) (**13**). Both **12** and **13** have been structurally characterized by X-ray diffraction.

Chapter 5. Results are presented from a picosecond pump-probe study designed to measure the impact of added xenon on the singlet-to-triplet intersystem crossing rates of diarylcarbenes. Within the error margins of the measurements, no effect of added xenon was observed.

To my grandfather Charlie Rabkin,

who helped me carry my first kitchen table across

Telegraph Ave. during my first week in Berkeley

and our last together. He showed me the value

of a life well-lived.

Acknowledgments

The work described in this dissertation was publicly funded through the United States Department of Energy, and I am grateful for the support.

On a more personal note, I've been contemplating these acknowledgments—the most important section of the thesis—since around my second month in grad school. Since that time, the number of people to whom I'm grateful has grown to an intimidating extent, and I'm certain I'll forget to mention at least several of them in the coming pages. I apologize and offer them my first thanks.

I was very fortunate to work with two advisors collaboratively, Professors Bob Bergman and Brad Moore. I thank them first for the extraordinary scientific education I received. Both Bob and Brad emphasize depth of understanding, not simply breadth of knowledge, and I particularly appreciate that. I also appreciate their enthusiasm for fundamental chemistry, their patience, and their helpful guidance throughout my graduate career. Professors Jim McCusker and Herb Strauss were also thoughtful and very helpful before, during, and long after my oral exam. I learned a lot from both of them. Professor Enrique Iglesia served as my outside committee member and thoughtfully read this manuscript; I appreciate his input. I'm also grateful to my undergraduate advisor, Professor Eric Jacobsen, and my mentor in his lab, Nat Finney, for pulling me into mechanistic organometallic chemistry and giving me an excellent background.

Dr. Bruce McNamara took me in when I showed up at Berkeley, bursting with enthusiastic ignorance, and he taught me everything I know about excimer lasers, diodes,

and the sheer joy of seeing data on the scope after two months of alignment and equipment repair. He had a tremendous work ethic and a contagious love of metal carbonyl chemistry, and I'm really glad I got to work with him early on. Half of the data presented in Chapter 2 is his; I'm grateful to have had the opportunity to finish that project.

Chapters 3 and 4 stemmed from a collaboration with Professor Charles Harris' group, which I also started working on in my first year of grad school. Working with the Harris group was a terrific experience and I'm grateful to Charles and to all of the students on the liquid side. In particular, I'd like to thank Matt Asplund and Haw Yang, both of whom taught me a lot of physical chemistry and made d-level a tolerable place to work.

In the Moore group, I benefited from helpful discussions with Ralph Tadday and Wai Fan. I'm extremely grateful to Aaron Mann for his help in lab and support over the last two years, particularly surrounding the move to OSU. Aaron's intuitive understanding of laser physics far exceeds my own, and I always appreciated his explanations of various experimental issues. At OSU, I was fortunate to work with Michael Pushkarsky, a talented and very knowledgeable physical chemist. I also appreciate the help I got from Xiangling “Flying-in-the-Air” Chen and Xiaoyong “Frank” Liu.

Upstairs in the Bergman Group, I overlapped with quite a number of wonderful people. When I arrived as a first year, I was literally amazed by the lengths to which Kris McNeill, Mark Aubart, Hans Luecke, and P. J. Alaimo went to help me and to give me an education. They fostered an atmosphere of constructive learning better than any I've seen

in other labs. I thank them not only for the interest they took in my research, but for teaching me the value of taking that sort of interest in other people's work. I am also grateful to P. J. for his specific suggestion to use trimethylamine-N-oxide for oxidative decarbonylation, which led to all of the work presented in Chapter 4.

Robin Fulton graciously shared her hood and Schlenk line with me, even after it became clear that I was going to spill the oil bath at least once a week. She was a good friend, and I appreciate her support in the chemical and personal aspects of my life. Zach Sweeney was also a good friend and a really stimulating person to talk chemistry with. If I'm still saying “Dude” in 20 years, it will be mostly his fault. Steve Klei and I got along so well that he drove all the way across the country with me, but before that, he was always around to grab a meal and talk about anything and everything. If I'm still saying “Money” in 20 years, it will be entirely his fault. Steve Skoog made me laugh hard enough to cry almost daily, yet he was still incredibly supportive. It really hurt to walk by his desk after he left and realize he wasn't there anymore.

My classmates Sara Paisner and Sarah Mullins were great to talk to, and I'm really glad to have shared four years with them. As for my classmate and labmate Dave Tellers, there really aren't enough words to thank him. He's an incredible friend and an inspiring scientist, and his suggestions permeate every aspect of this dissertation.

I appreciate Andy Holland's help setting up the nitrogen purge for my photolysis experiments in pyridine, and I'm grateful to Jen Krumper for her help with the low temperature NMR experiments described in Chapter 4. I wish them both well. I'm grateful to Drew Duncan and Dan Fox for helpful discussions, but more importantly, for their particular appreciation (tolerance?) of my clapping, snapping, singing, and generally

wacky sense of humor. I was lucky to get to know an enthusiastic first year class before moving to Ohio: Reema Thalji always brought a smile to my face; Joe Cordaro shared my passions for singing and straddling the physical/inorganic fence; Stephen Jenkins taught me to appreciate a down-home southern shrimp boil; and Kian Tan inspired me with his excitement and fascination toward chemistry (rivaled only by his excitement and fascination toward the Krispy Kreme doughnut store). To the other Bergman students and postdocs with whom I overlapped, you have my heartfelt thanks—you all helped.

Drs. Fred Hollander and Dana Caulder solved the crystal structures presented in Chapter 4. Rudi Nunlist was very helpful with the deuterium NMR spectra of those same compounds. More generally, I appreciate all the work performed in connection with my research in the Berkeley and OSU glass shops, machine shops, wood shops, and electronic shops. The Bergman and Moore group administrative assistants Catherine Madsen, Tom Livingston, Maria Mongenas, and Becky Gregory (she works for Terry Miller, but close enough) worked incredibly hard, and I'm very grateful for all their help, particularly with the bureaucratic zoo created by the move to OSU.

I spent three very fulfilling months in Professor Karl Kompa's lab in Garching, Germany, and I look forward to six more in the coming year. I'm grateful to Lars Windhorn and to everyone else in the Motzkus/Proch labs for everything I learned there and for the opportunity to return and continue an exciting line of research.

Finally, my warmest thanks go to family and friends for their incredible support throughout my time in graduate school. During particularly stressful periods, my weekly good shabbos calls from my father and brother Max and Sunday morning conversations with my mother were the only way I had of marking time. My college friends Mike

Kahan, Andrew Wright, Stacy Friedman, Kevin Martin, and Elias Aliprandis were always supportive and interested in what I was doing. Lastly, Beth Elson has made the last six months happier than I ever thought life could be. I'm more grateful than she knows.

Table of Contents

Chapter 1. General Introduction

The experiments described in the following chapters most appropriately fall into the category of mechanistic chemistry. To elucidate the general objectives and methods of that field of study, it is first necessary to consider the nature of chemical reactions. Two specific and very common household reactions are illustrative in this regard—burning a wax candle and mixing vinegar with baking soda.[1,2] On the simplest level, we note the visual observations that suggest something has happened: the candle disappears slowly in the vicinity of the flame, while the vinegar/baking soda (vbs) reaction is comparatively rapid and characterized by the sudden formation of numerous small bubbles. For the nonscientist, these processes bear no clear resemblance to one another at all. From a chemical standpoint, however, they are markedly similar in several important ways.

The first step in rigorous analysis of a chemical reaction might seem to be identification of the products. Actually, it is often important to perform a comparably careful assessment of the starting materials, as a reaction may involve components that are not obviously present at first glance. Essentially we need to know exactly what has reacted and what has been produced. In the case of the candle, wax is a simplistic abbreviation for a mixture of several different kinds of molecules, all of which consist essentially of long chains of carbon atoms bound to one another and to hydrogen atoms. The vinegar is acetic acid diluted in water, while the baking soda is sodium bicarbonate. Further characterization of starting materials shows that the candle requires air (specifically oxygen) to react, while the vinegar and baking soda do not. We could reach

these conclusions by carrying out both reactions in closed jars. Thus we can say that the candle reaction is really a reaction between wax and oxygen, while the vbs reaction occurs strictly between acetic acid and sodium bicarbonate in water.

Product identification in both of the above reactions is not entirely trivial. We can show that the candle does not actually "disappear", but rather reacts with oxygen to form a gas, like the air, which may be carefully trapped for analysis. The vbs reaction also produces a gas; in that case the gas bubbles out of the liquid and can also be trapped. All of the gases formed in these reactions are colorless, but there are many modern techniques available to identify them. One method, used often in the nineteenth and early twentieth centuries, involved letting these gases react with other known substances. If the product of the subsequent reaction were familiar, we might thereby identify the gas based on past experience with that reaction. Modern identification methods typically focus less on reactivity and more on molecular structure. Compounds are often analyzed spectroscopically, i.e., assessed on the basis of their absorption of ultraviolet, visible, and infrared light, as well as X-rays and microwaves. The absorption of energy at a particular wavelength (or color in the case of visible light) is characteristic of certain types of atoms and bonding arrangements. Using methods such as these, we discover that both the candle and the vbs reactions produce carbon dioxide gas. Both reactions also produce water; in the candle reaction, the water is hot enough to be released as steam, while in the vbs reaction it remains a liquid and mixes with the water already present. The vbs reaction yields another major product— sodium acetate. The candle reaction yields small amounts of various additional carbon-containing compounds, although carbon dioxide and water account for the primary reaction products.

The starting materials and products are thus analyzed and characterized, but a compelling and provocative question remains. What exactly has happened to the candle and to the baking soda/vinegar solution in order to form the products so carefully identified? What do the reactions have in common that lead to such similar products from such apparently different precursors? Which atoms move where, and which bonds break and form when? These questions refer to the reaction *mechanism* and, as such, lie at the heart of mechanistic chemistry.

At the level of chemistry described in this dissertation, the vbs reaction can be explained fairly rigorously, while the candle reaction (a form of combustion) cannot. The vbs reaction is known to proceed essentially along the lines illustrated in Scheme 1.1.[3] There are two types of molecules separated by water—the bicarbonate, marked **A**, and the acetic acid, marked **B**, which atomically differs from the bicarbonate only by replacement of one oxygen with a methyl group (a carbon bonded to three hydrogens). We can ignore the sodium ion because the water molecules separate it from the bicarbonate when the baking soda first dissolves, and it does not participate in the reaction. What happens, effectively, is that many **A** and **B** molecules move randomly throughout the water, and when they come together, a hydrogen ion is transferred from **B** to **A**. After formation of the new O-H bond, the product **A**-H breaks apart to yield water and carbon dioxide.

Scheme 1.1

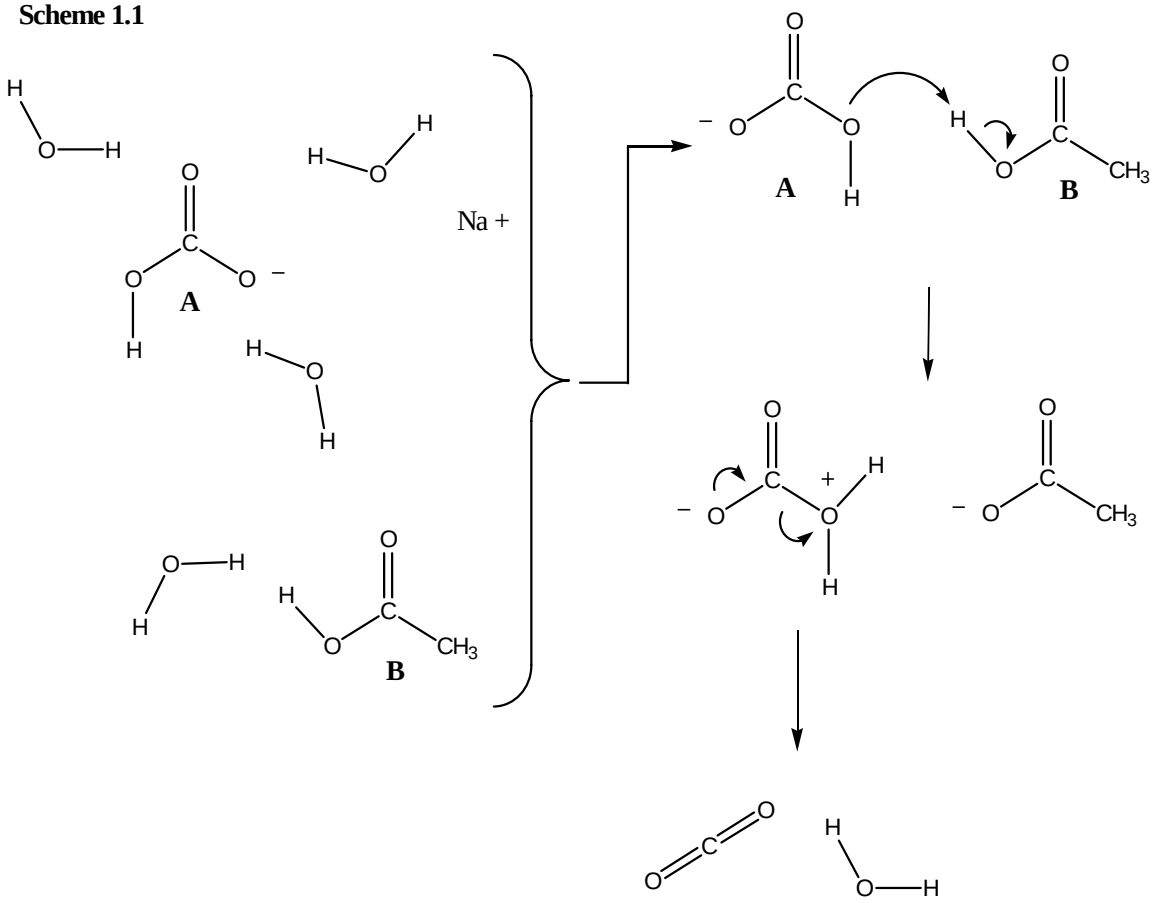

Scheme 1.2

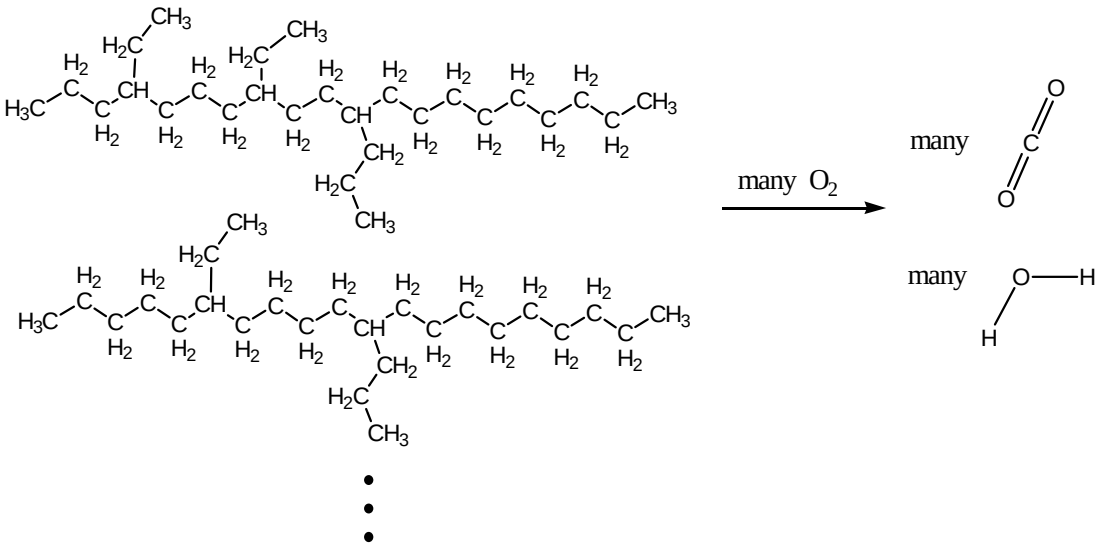

The reaction is in fact slightly more complicated, because water molecules can shuttle the hydrogen ion from **B** to **A** so the two do not have to come in contact. Nonetheless, it is clear in this reaction which bonds are made and which broken, in what order, to form the products from the starting materials. Moreover, this reaction is homogeneous, meaning that all compounds reacting with one another are in the same state (in this case, they are all surrounded by water at the molecular level). It is straightforward to measure and alter their relative abundance in the solution and to account for their motion using a single model. We might say that the molecular choreography is well-defined. It is therefore clear that if we measure the rate of the reaction, we are measuring the rate of changes in molecular bonding.

The burning candle is a much more complex phenomenon. To begin with, the atomic structures of the starting materials are much more dissimilar to those of the products than in the vbs reaction. The vbs reaction involves very little atomic reorganization. The essential structures of water and carbon dioxide are already evident in the structure of bicarbonate—all that is needed to yield the products is formation of one O-H bond and scission of one C-O bond. The candle, in contrast, is composed of long chains of carbon atoms bound to one another and to hydrogen. In order to form the products carbon dioxide and water, every C-H and C-C bond in a given molecule must be broken and as many O-H and O-C bonds formed (Scheme 1.2). Sorting out which step occurs when is a much harder task in this case.

Furthermore, the burning process is heterogeneous, meaning that it involves materials in different states: there is solid wax, liquid wax at the base of the flame, and

gaseous oxygen diffusing into the flame from all directions. Prior to addressing any changes in molecular bonding, it is necessary to sort out the process whereby the wax melts and the oxygen comes in direct contact with it. Factors such as wax surface area become very important, and yet the surface area changes rapidly and unpredictably as the candle melts and burns.

A final challenge is the extremely high temperature of the flame, which causes molecules and atoms to react in ways hard to predict by studying slow reactions at room temperature (somewhat like modeling a riot with a ballet). Preliminary mechanistic studies of combustion processes therefore focus on what sorts of intermediate species appear over the course of the reaction, prior to formation of the final products. Efforts can then be directed toward preparation and analysis of these intermediate species in a context simpler than the burning candle; the goal is to see generally how they interact with one another. At that stage, a sophisticated mathematical model may be used to account for the many different bond-making and bond-breaking pathways operating simultaneously in the flame.[4]

The studies in this dissertation primarily involve measurements of reaction rates in low-temperature homogeneous solutions. Rate measurements, referred to as kinetic studies, offer tremendous aid in understanding reaction mechanisms. A deliberate change in reaction conditions that leads to a change in rate can support one possible mechanism over another. Suppose, for example, that we did not know the sodium ion was irrelevant to the vbs reaction. We might address this question by measuring the rates of carbon dioxide formation upon addition of vinegar to a sodium bicarbonate (baking soda) solution in one flask and a potassium bicarbonate solution in another. A change in

reaction rate would signal that the nature of the ion, sodium or potassium, was relevant to the reaction, and thus the ion must play some mechanistic role.

Unfortunately, rate measurements can be misleading if the reaction occurs rapidly. If we were to add vinegar to the bicarbonate solutions, CO_2 formation would begin while the addition was in progress. In the limiting case, all we would measure would be the rate of vinegar addition, which would shed no light on whether the sodium and potassium ions were playing a role. Consider, for example, that replacement of sodium with potassium might reduce the reaction time from four to two seconds upon mixing, but if the vinegar were added over five minutes, the reaction would seem to take five minutes in either case. This problem is addressed through a technique termed "flash kinetics." In general, rate measurements are performed by initiating the reaction with a short laser pulse and monitoring the subsequent disappearance and formation of molecular species with a second laser.[5] The advantage of this methodology is that the starting point has a short, well-defined duration (the duration of the laser pulse, which can range from millionths to hundred-trillionths of a second) and is extremely precise.

The molecules subjected to flash kinetic studies in the chapters that follow consist generally of a rhodium (Rh) atom bound to several other structures (ligands) composed of a small number of carbon, oxygen, nitrogen, boron, and hydrogen atoms. In particular, each molecule of interest contains two carbonyl (CO) ligands bound to Rh. The CO ligand has several properties particularly well-suited to flash kinetic studies. The first is that exposure of a metal carbonyl complex to UV radiation tends to result in cleavage of the bond between the metal atom and one of the CO ligands. The metal-containing molecule that remains can be remarkably reactive. The Rh complexes in this dissertation

were chosen for study because, upon loss of a CO ligand, the molecules react with hydrocarbons by breaking a C-H bond to form a product with a new Rh-C bond and a new Rh-H bond. This process is of interest because it holds potential for more useful and easily controlled reactions of hydrocarbon chains than the combustion reaction described earlier, which leads indiscriminately to CO_2 and water (combustion is considered useful more for the heat it releases than for the products it yields).

The second useful feature of metal-CO compounds is their capacity to strongly absorb infrared (IR) radiation at a particular wavelength. The absorption wavelength, moreover, is very sensitive to the nature of the metal and of the other ligands (besides CO) bound to the metal. Formation of a Rh-H bond, for example, would change the wavelength of IR radiation absorbed by a CO group bound to that Rh, because the H atom takes electron density away from the CO group. Observation of a change in wavelength therefore affords insight into bonding changes at the metal center.

The above considerations serve as the underpinnings for the flash kinetic studies described in the coming chapters.[6] Briefly, a Rh complex with two CO ligands is exposed to a UV laser; one CO ligand dissociates; the subsequent chemistry of the Rh molecule is monitored using an IR laser to identify intermediates and products based on the IR absorption of the remaining CO ligand (still bound to Rh). Once a particular species has been identified based on its absorption wavelength in the IR, the lifetime of that species can be measured by assessment of how long that particular wavelength continues to be absorbed. Practically, this assessment is made by sending the IR radiation of desired wavelength through the sample to a detector. The higher the

concentration of the absorbing species, the lower the IR power striking the detector will be.

Scheme 1.3 below is taken from Chapter 2.

Scheme 1.3

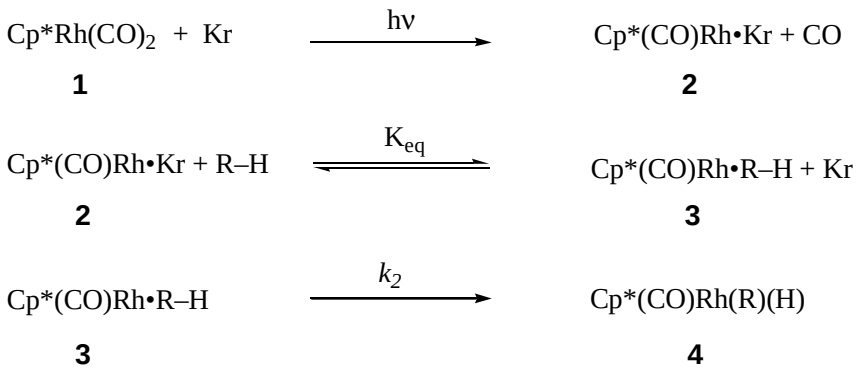

Each numbered compound was identified and monitored throughout the reaction by the IR absorption of its CO group. Cp* is an abbreviation for pentamethylcyclopentadienyl, another ligand bound to the Rh center, while R-H represents a generic hydrocarbon chain. In compound **3**, the hydrocarbon is very weakly bound to the Rh center, while in compound **4** a C-H bond has been broken and Rh-C and Rh-H bonds formed. The reaction was carried out in liquid krypton (Kr) or xenon (Xe) because conventional solvents would have reacted with **1** after loss of the CO ligand. In fact, even these inert gases bind weakly to Rh and other metal centers, though they can be displaced by hydrocarbons.

The above scheme shows three discrete steps. The first step, UV-induced loss of a CO ligand, is relatively rapid. We were interested in the second and third steps, more specifically in their dependence on the structure of the hydrocarbon. The second step has

a double arrow because the compounds on both sides can interchange with one another several times prior to the third step. As described in Chapter 2, we found that both the binding step (**2**→ **3**) and the insertion step (**3**→ **4**) depend on the structure of the hydrocarbon. In general, larger hydrocarbons tend to bind more efficiently but exhibit a slower insertion step.

Chapter 3 examines the reactivity of the Rh compound shown below:

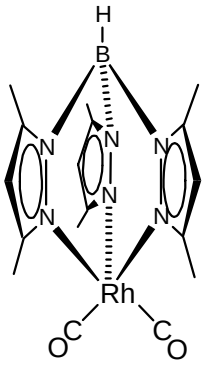

5

This compound also loses a CO group upon UV irradiation, leading to reaction with hydrocarbons. In addition, the ligand above the Rh (abbreviated Tp*) changes its mode of bonding from three nitrogen donors to two, giving rise to the structure below:

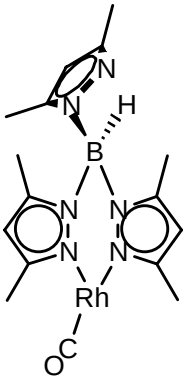

7

Chapter 3 focuses on the interconversion between three-N and two-N binding modes in this compound after UV-induced CO loss in liquid xenon solution. Once again, products were characterized and monitored by IR. Our structural assignments are based on companion studies using a Bp*Rh compound (**9**), which bears a ligand with only two nitrogen donors, as a model for the two-N binding mode of the Tp* compound:

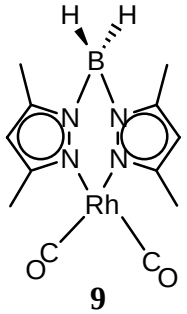

9

The Bp* compound was employed to ascertain the expected IR absorption wavelength of a two-N bound Tp*Rh(CO) species. The result matched the absorption wavelength assigned to compound **7**.

Chapter 4 describes a diversion from flash kinetics, occasioned by the unexpected observation of B-H (boron hydride) reactivity in one of the Bp*Rh compounds that we prepared. Various methods were used to characterize the product and to understand the mechanism for its formation. A labeling study, for which the ligands were prepared with heavy hydrogen (^{2}H) and heavy carbon (^{13}C), was undertaken in order to track the movements of specific atoms over the course of the reaction. The reaction involves H transfer from boron to Rh, and the labeling study confirmed that this transfer is intramolecular, meaning that the hydrogen atom stays within a single molecule, as opposed to moving from the boron in one molecule to the Rh in another.

Finally, Chapter 5 returns to flash kinetics in order to determine whether xenon might bind weakly to a reactive class of carbon molecules termed carbenes (characterized by a central carbon atom with two free valence electrons), in analogy with its binding to Rh and other metal centers. None of the reactive species absorbed strongly in the IR, so the reaction was both induced and monitored using UV radiation. Within the error margin associated with our experimental measurements, no evidence was found for xenon-carbene interaction.

Notes and References

1) For an interesting discussion of candle chemistry, see: Birk, J. P.; Lawson, A. E. *J. Chem. Educ.* **1999**, *76*, 914.

2) The vinegar and baking soda reaction is addressed qualitatively in: Carlson, G. L. *J. Chem. Educ.* **1990**, *67*, 597.

3) The framework for mechanisms such as this one can be found in organic chemistry texts. See, e.g.: March, J. *Advanced Organic Chemistry: Reactions, Mechanisms, and Structure*; Wiley: New York, 1992.

4) For a technical discussion of modern mechanistic studies of combustion, see: Warnatz, J.; Maas, U.; Dibble, R. W. *Combustion: Physical and Chemical Fundamentals, Modeling and Simulation, Experiments, Pollutant Formation*; Springer-Verlag: Berlin, 1996.

5) Espenson, J. H. *Chemical Kinetics and Reaction Mechanisms*; 2nd ed.; McGraw-Hill: New York, 1995.

6) A good review of infrared flash kinetic techniques and their application to organometallic mechanistic studies is: McFarlane, K.; Lee, B.; Bridgewater, J.; Ford, P. C. *J. Organomet. Chem.* **1998**, *554*, 49.

Chapter 2. The Effect of Alkane Structure on Rates of Photoinduced C-H Bond Activation by $Cp^*Rh(CO)_2$ in Liquefied Rare Gas Media

Introduction

Despite great natural abundance, saturated hydrocarbons remain an underutilized resource from a synthetic perspective. The high bond strengths (~100 kcal/mol) and pK_a values (~50) of aliphatic C-H bonds have hindered attempts at broad and selective functionalization. Alkane oxidations catalyzed heterogeneously are used to access alkenes, aromatic hydrocarbons, and various oxygenated compounds, but selectivity in these reactions is relatively low. In contrast, iron-based enzymes such as methane monooxygenase and cytochrome p450 catalyze specific functionalization of alkanes with such high selectivity that the scope of accessible products is rather limited.[1,2]

In this context, there was great excitement at the independent demonstrations by Bergman and Graham in 1982 of aliphatic C-H bond oxidative addition across transition metal centers in soluble, well-defined complexes (Scheme 2.1).[3-7] In the intervening time, quite a number of early and late organotransition metal compounds have been shown to react with simple alkanes.[8-10] The transformation has intrigued researchers both because of its potential as a means of selectively functionalizing hydrocarbons,[11-14] and because of the remarkable facility with which unsaturated metal centers can cleave such strong bonds. There have thus been a great number of kinetic, mechanistic, and theoretical studies focused on aliphatic C-H activation.[15-30]

Scheme 2.1

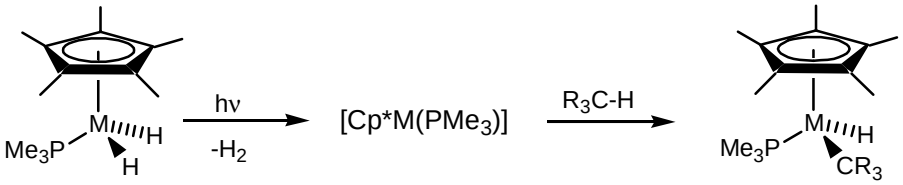

M = Ir: A. H. Janowicz, R. G. Bergman 1982
M = Rh: W. D. Jones, F. J. Feher 1983

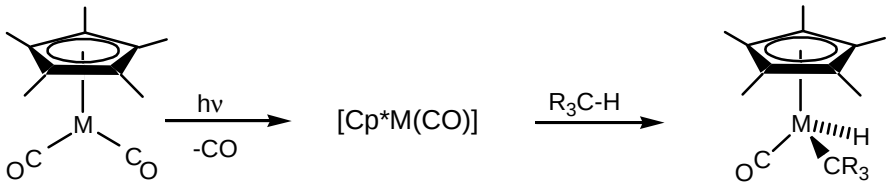

M = Ir: J. K. Hoyano, W. A. G. Graham 1982
M = Rh: A. J. Rest *et al.* 1987

The structural and kinetic features of the metal-alkane interaction prior to oxidative addition remain an area of active inquiry. Theory and experiments suggest that alkanes coordinate to transition metal centers with significant binding energies (*ca.* 5-12 kcal/mol), both in the gas phase and in solution.[31] These species are often referred to as σ-complexes to reflect the coordination of the alkane through a C-H σ-bond. Although none have been isolated, many examples of alkane σ-complexes involving Group 6 and 7 transition metal carbonyls have been extensively characterized (by UV, IR, and NMR spectroscopy) upon transient generation by flash photolysis.[32,33] In these cases, the complexes fall apart on a timescale ranging from microseconds to milliseconds without undergoing oxidative addition.

When oxidative addition does take place, σ-complexes are now firmly established as intermediates.[8,19,21,34,35] Preliminary evidence along these lines was indirect and derived mainly from deuterium-labeling studies. Specifically, the rate of alkane reductive elimination in $Cp^*(PMe_3)M(CDR_2)H$ (M=Rh, Ir) was measurably slower than

the rate of H/D exchange between the metal and the carbon, thus implicating a σ-complex intermediate.[36,37] Also, the reductive eliminations exhibited inverse kinetic isotope effects for perdeutero alkanes, an observation most easily explained by a small normal KIE coupled to a larger equilibrium isotope effect favoring the C-D···M σ-complex. More conclusive evidence was obtained through flash kinetic studies in our group (*vide infra*), which permitted direct spectroscopic characterization of the intermediates on the C-H activation pathway.

These results establish that the ratios of C-H activation products formed in traditional competition studies, in which a metal complex is allowed to react in a mixture of two or more alkanes to probe selectivity, cannot be interpreted as a simple function of two competing C-H activation steps. Rather, the final products are determined both by the binding affinity of each alkane toward the metal center and by the relative rates of the elementary C-H bond insertion steps. Until recently, time-resolved studies in neat alkane solvent rarely permitted a meaningful comparison of binding affinities, because under these conditions the binding step occurs on a picosecond or subpicosecond timescale.[38] Studies in rare gas media, however, have presented a unique opportunity to examine alkane binding energetics independently, and thus to assess their role in controlling C-H activation selectivities.

The work reported here concerns C-H activation achieved by photoinduced reaction of $Cp^*Rh(CO)_2$ (**1**) with alkanes in liquid krypton or xenon solution. The reaction proceeds on a microsecond timescale at low temperature and has been studied in our group previously by infrared flash kinetic spectroscopy. In the earliest studies, Wasserman and Weiller employed a carbon monoxide laser to monitor the CO stretches of intermediates and products formed upon 308 nm photolysis of **1** in Kr solutions of cyclohexane, neopentane, and their perdeuterated analogs.[39] The results supported the mechanism shown in Scheme 2.2.

Scheme 2.2

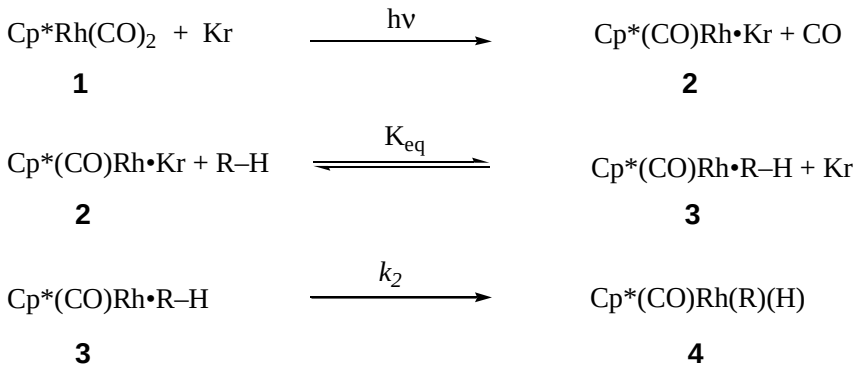

Photolysis induces CO loss from the parent complex to form a krypton-solvated rhodium species **2**; solvation by Kr sequesters the complex until the alkane enters the coordination sphere of the metal. The data are most consistent with a well-defined pre-equilibrium between discrete Rh-Kr (**2**) and Rh-alkane (**3**) solvates. The alkane solvate **3** then reacts thermally by oxidative addition of a C-H bond across the rhodium center to form a rhodium alkyl hydride product (**4**). In subsequent studies, Schultz and Bengali confirmed this mechanism using a diode laser probe, which in the case of perdeutero neopentane permitted spectral and (therefore) temporal resolution of the Kr and alkane complexes.[40,41]

The mechanism outlined in Scheme 2.2 can be analyzed according to a modified Michaelis-Menten model, assuming rapid pre-equilibrium, to give the expression shown in eq 2.1 for k_{obs}, the pseudo-first-order rate constant measured under flooding conditions in alkane (large excess relative to Rh).[39] A derivation of the expression is given in the appendix.

$$k_{obs} = \frac{k_2[\text{R-H}]}{[\text{R-H}] + \frac{[\text{Kr}]}{K_{eq}}} \qquad (2.1)$$

By fitting the rate data to this expression at various alkane concentrations, it is possible to extract two specific parameters: K_{eq}, which characterizes the extent to which the pre-equilibrium favors the alkane complex over the rare gas complex; and k_2, which represents the elementary rate constant for the oxidative addition step from the alkane complex. Thus direct and separate comparisons can be made between the binding affinities of various alkanes for the Rh center and between the rates of elementary C-H bond insertion.

A comparison of the parameters for reaction of **1** with cyclohexane[41] and with neopentane[40] indicated a definite impact of alkane structure on both the binding step and the oxidative addition step. A better understanding of this impact is of particular interest in characterizing and predicting selectivities in C-H activation reactions. To this end, we have employed infrared flash kinetic spectroscopy for systematic rate measurements of the photolytic reaction of **1** with series of linear and cyclic alkanes in liquid rare gas solution.

Experimental Methods

The apparatus and techniques employed for flash infrared kinetic studies in our laboratories have been described in detail previously.[41] A schematic diagram is shown in Figure 2.1. Briefly, reactions were performed in a high-pressure, temperature-controlled (± 1 °C) copper cell. Kinetics were measured using a standard pump-probe scheme, with the reaction initiated by a 308 nm pulse from a XeCl excimer laser (Lambda Physik EMG 103 or Compaq 102, pulse fwhm *ca.* 20 ns) and probed collinearly (5.0 cm pathlength) using the tunable output of an IR diode laser (Mütek model MDS 2020) impinging on a liquid N_2-cooled InSb detector (Cincinnati Electronics model SDD-32E0-S1, 100 ns

risetime). IR wavelengths were selected using a monochromator at 4 cm^{-1} resolution (to maximize IR power for an optimal signal-to-noise ratio). Total UV pulse energies were approximately 100 mJ, but the pulses were unfocused in order to irradiate the sample uniformly. The windows of the sample cell were 1 cm^2 in area; therefore only the central 1 cm^2 of the 10 cm^2 beam cross section reached the sample, corresponding to an effective energy per pulse of approximately 10 mJ. The IR beam emergent from the diode was collimated with a lens to a 4-5 mm diameter so as to fit entirely within the area irradiated by the UV beam.

For kinetic runs, the diode laser was tuned to the wavelength of interest, and data from 5-20 laser shots were averaged and corrected by subtraction of an equal number of background scans obtained with the UV beam blocked. Because the system sometimes exhibited sudden, severe noise spikes that the background scans failed to remove, precision was achieved by collecting 4-5 such data sets at each wavelength. Data traces were collected using an oscilloscope (LeCroy 9310, 300 MHz), transferred to PC and fit using nonlinear least squares routines in commercial software (Kaleidagraph, version 3.0, Synergy Software © 1996). Reaction mixtures were also characterized using a Nicolet 550 FTIR spectrometer at 1 cm^{-1} resolution. The FTIR beam was directed through the cell along the transverse axis (1.43 cm pathlength) and detected using a HgCdTe detector (Cincinnati Electronics model MDD-10E0-S1-NP).

Krypton and xenon (99.999%) were purchased from Spectra Gases and used as received. Liquid alkanes (all 99% or greater) were purchased from Aldrich or Acros, stirred over H_2SO_4 and H_2SO_4/permanganate solutions to remove olefinic impurities, dried successively over sodium sulfate and either calcium hydride or elemental sodium, and vacuum-transferred immediately before use. $Cp^*Rh(CO)_2$ (**1**) was either prepared according to a literature procedure[42] or purchased from Strem Chemicals.

The concentration of **1** employed in each kinetic run was approximately 10^{-4} M. Alkane concentrations were determined by integration of appropriate bands in FTIR

spectra of the reaction mixture. For the heavier liquid hydrocarbons, introduction of precise small quantities of alkane into the cell was very difficult (both syringe and vacuum transfer techniques showed poor reproducibility); greater accuracy in determining absorption coefficients was achieved using Beer's Law plots constructed from standard solutions of the alkane in carbon tetrachloride. IR spectra of these standard solutions were acquired at room temperature using a 0.10 cm pathlength cell. These spectra generally matched those of the hydrocarbons in liquid Kr, with the exception of 2 to 5 cm^{-1} peak shifts and narrowing of the hydrocarbon absorption bandwidths in Kr (typical fwhm values were 3-4 cm^{-1} in Kr and 7-8 cm^{-1} in CCl_4). Concentrations were determined by full band integration in the liquid Kr spectra; the same limits of integration were used in both solvents and were chosen so as to fully encompass the wider bands in CCl_4. When possible, concentrations were checked by band integration at two separate wavelengths. Beer's Law data obtained by dissolution of known amounts of cyclohexane in liquid Kr (albeit with moderate precision) confirmed the accuracy of the absorption coefficients obtained in CCl_4 to within 10%.

As the cell temperature was raised from -110 °C to -80 °C in typical experiments, the vapor pressure of the liquid krypton solution increased from 200 to 800 psi (1.4 MPa to 5.5 MPa). The liquid volume visibly increased as well. These changes in experimental conditions were observed to cause a systematic change in the hydrocarbon absorption intensities. Specifically, lowering the solution temperature from -80 °C to -110 °C gave rise to a 20% increase in integrated absorption intensity.[43] Kr/hydrocarbon vapor pressure data suggest that between -80 °C and -110 °C less than 2% of the dissolved alkane evaporates into the head space of the cell, even in the case of ethane.[44,45] Variable temperature ^1H NMR experiments using Kr/ethane solutions in a high pressure NMR tube confirmed this estimate. We therefore attribute the changes in band intensity to actual changes in hydrocarbon concentration. These result from a decrease in the density of the liquid Kr with rising temperature and consequent increase in the overall

solution volume.[46] Alkane concentrations were therefore evaluated independently at each temperature of interest.

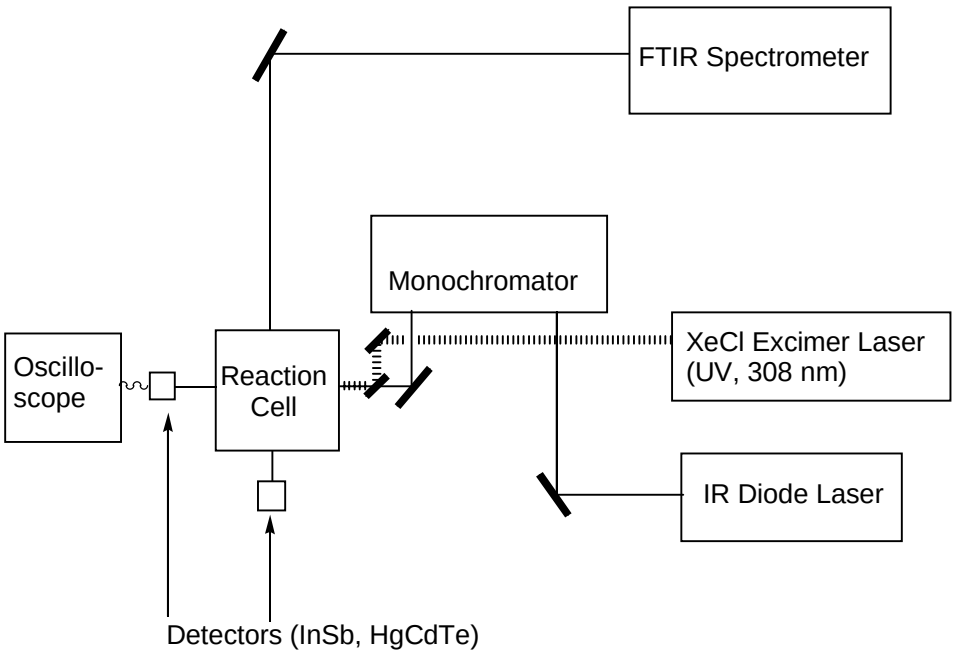

Figure 2.1. Schematic diagram of the apparatus used for IR flash kinetic measurements in liquid noble gas solution.

Results [47]

Photolysis of 1 in liquid krypton/alkane solutions. As shown by previous work in our group, photolysis of **1** in pure liquid krypton results in detector-limited rise of a transient absorption at 1947 cm^{-1}. This species exhibits well-defined, single-exponential decay behavior over a 200 μs interval at -80 °C and has been assigned to Kr solvate **2**, Cp*Rh(CO)•Kr.[41] In the presence of alkane, the observed rate constant for decay of the 1947 cm^{-1} absorbance increases. Furthermore, in the 2000-2008 cm^{-1} region, a new transient absorption grows in with a frequency that shifts slightly with alkane structure and an observed rate constant matching the rate of decay at 1947 cm^{-1}. On the basis of kinetic analysis and literature precedent, this new transient absorption has been assigned to the Rh alkyl hydride **4**, Cp*Rh(CO)(H)(alkyl).[41]

We have found that these observations are general for all alkane studied except methane; we did not observe any reaction of **1** with methane in liquid Kr/CH_4 mixtures, even at methane concentrations in excess of 3 M.[48] Table 2.1 lists the IR absorptions assigned to the Rh alkyl hydride products for reaction of **1** with cyclohexane[41] and with the linear and cyclic[49] alkanes examined in the present study.

Table 2.1. IR Bands Assigned to Cp*Rh(CO)(alkyl)(H) in Liquid Kr

Alkane	ν_{CO} (cm^{-1})
Ethane	2007 (± 2)
Propane	2005 (± 2)
Hexane	2007 (± 2)
Octane	2005 (± 2)
Cyclopentane	2005 (± 2)
Cyclohexane[a]	2003 (± 2)
Cycloheptane	2004 (± 2)
Cyclooctane	2000 (± 2)

a) Ref. 41.

Rates for the above reactions were measured under flooding conditions, with concentrations of **1** below 10^{-3} M and alkane concentrations systematically varied in the 0.001-2 M range. Studies were carried out between -80 °C to -110 °C. Transient absorption traces at 1947 cm^{-1} and in the 2000 cm^{-1} region displayed pseudo-first-order behavior. Representative traces are shown in Figure 2.2. Overall rate constants, k_{obs}, were obtained by single exponential fits to such traces (generally the final values were obtained by averaging the fitting results of at least three separate traces at 1947 cm^{-1} and three in the 2000 cm^{-1} region). The k_{obs} values were then plotted against alkane concentration and the resulting curves fit according to the expression in eq 2.1 by nonlinear least squares methods to afford values for k_2 and K_{eq} at each temperature. Figures 2.3 and 2.4 show plots of k_{obs} vs. alkane concentration for the series of linear hydrocarbons in the –80 °C to –110 °C temperature range.

A clear trend correlating saturation behavior with alkane size is apparent. With ethane as substrate, the reaction rate does not begin to reach saturation until the alkane concentration exceeds 0.5 M. In contrast, the larger alkanes induce rate saturation at much lower concentrations, indicative of larger K_{eq} values. Under the reaction conditions, rate saturation occurs because krypton no longer competes effectively with the alkane for coordination to the rhodium fragment in the pre-equilibrium. At this point k_{obs} may be equated with the rate constant for oxidative addition, k_2. Figures 2.5 and 2.6 show similar plots for reaction of the series of cyclic alkanes. The cyclohexane data[41] at –90 °C have been reproduced for comparison with the data obtained in the present study. Here the impact of alkane size on the pre-equilibrium emerges even more dramatically, as the cycloheptane and cyclooctane reactions evidence rate saturation at close to the lowest alkane concentrations employed. A countervailing trend is evident in the rate of the insertion step characterized by k_2, which is highest for ethane, lowest for cyclooctane.

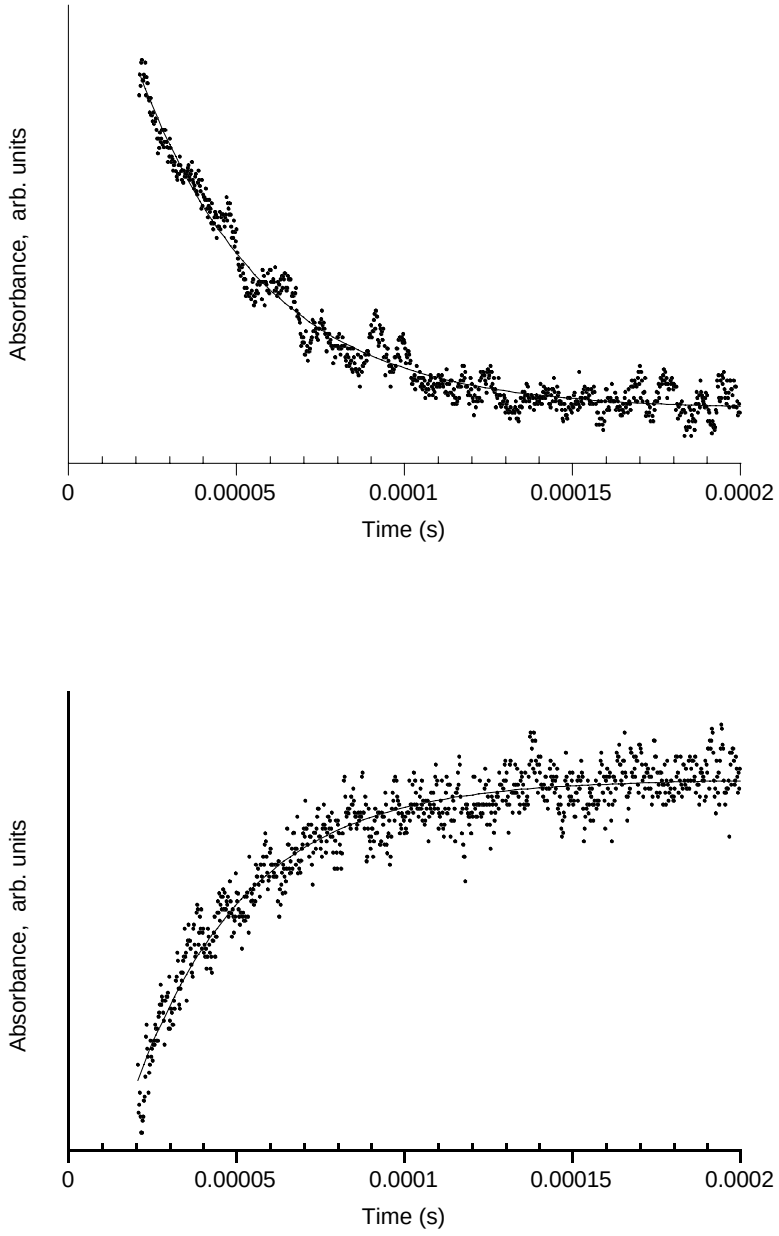

Figure 2.2. Representative kinetic traces for reaction of **1** in the presence of 1.7 mM octane in liquid Kr at –90 °C. The top trace shows decay of the absorbance at 1947 cm^{-1}, due to disappearance of the Cp*Rh(CO)•octane and Cp*Rh(CO)•Kr adducts. The solid line is an exponential fit giving a k_{obs} value of 2.7 (± 0.2) x 10^4 s^{-1}. The bottom trace shows concurrent growth of the absorbance at 2005 cm^{-1}, due to formation of Cp*Rh(CO)(octyl)(H). The solid line is an exponential fit giving a k_{obs} value of 3.0 (± 0.2) x 10^4 s^{-1}.

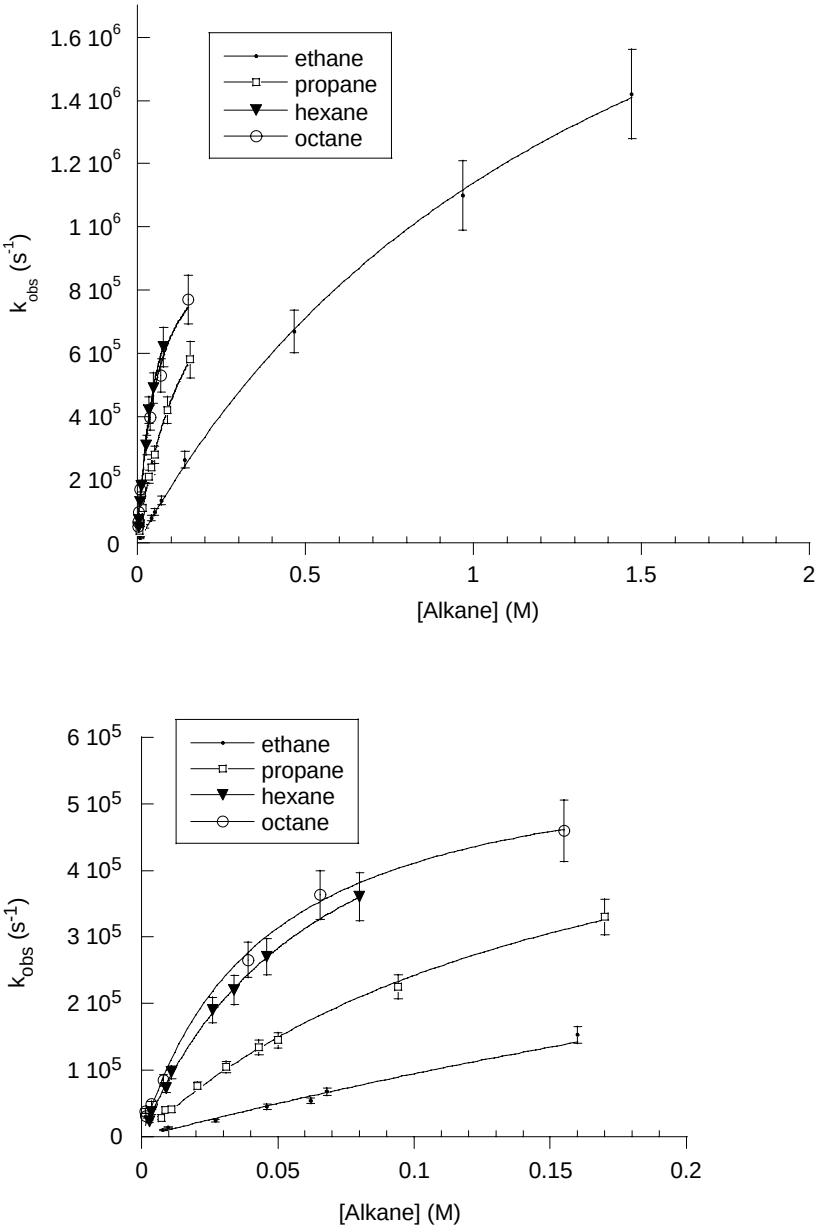

Figure 2.3. Plots of k_{obs} vs. concentration of linear alkanes at –80 °C (top) and –90 °C (bottom). The solid lines represent nonlinear least squares fits of the data to eq 2.1. Data for ethane at high concentrations (above 0.5 M) are shown only at –80 °C, although points at high ethane concentrations were used at every temperature to determine the kinetic parameters.

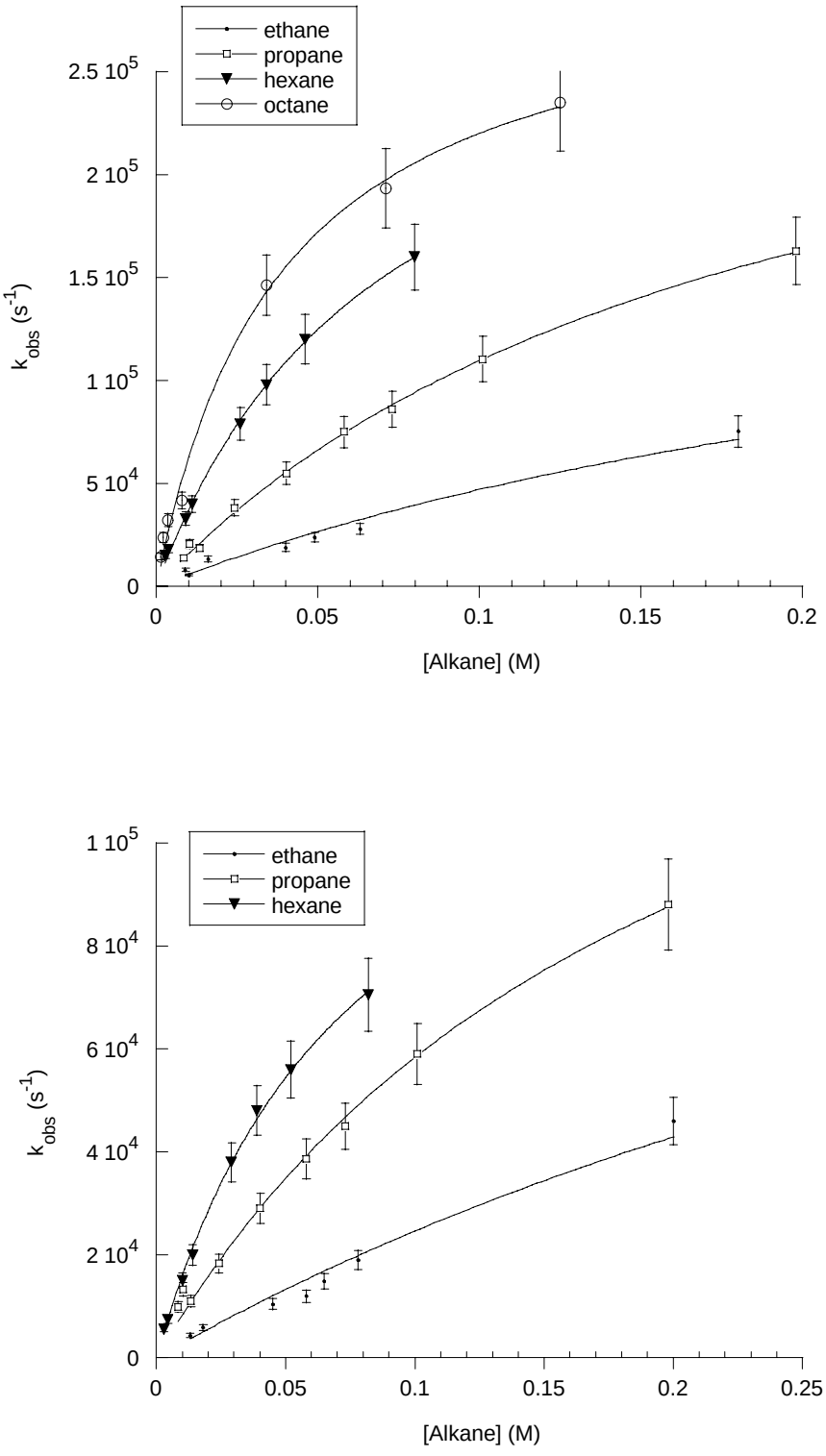

Figure 2.4. Plots of k_{obs} vs. concentration of linear alkanes at –100 °C (top) and –110 °C (bottom). The solid lines represent nonlinear least squares fits of the data to eq 2.1.

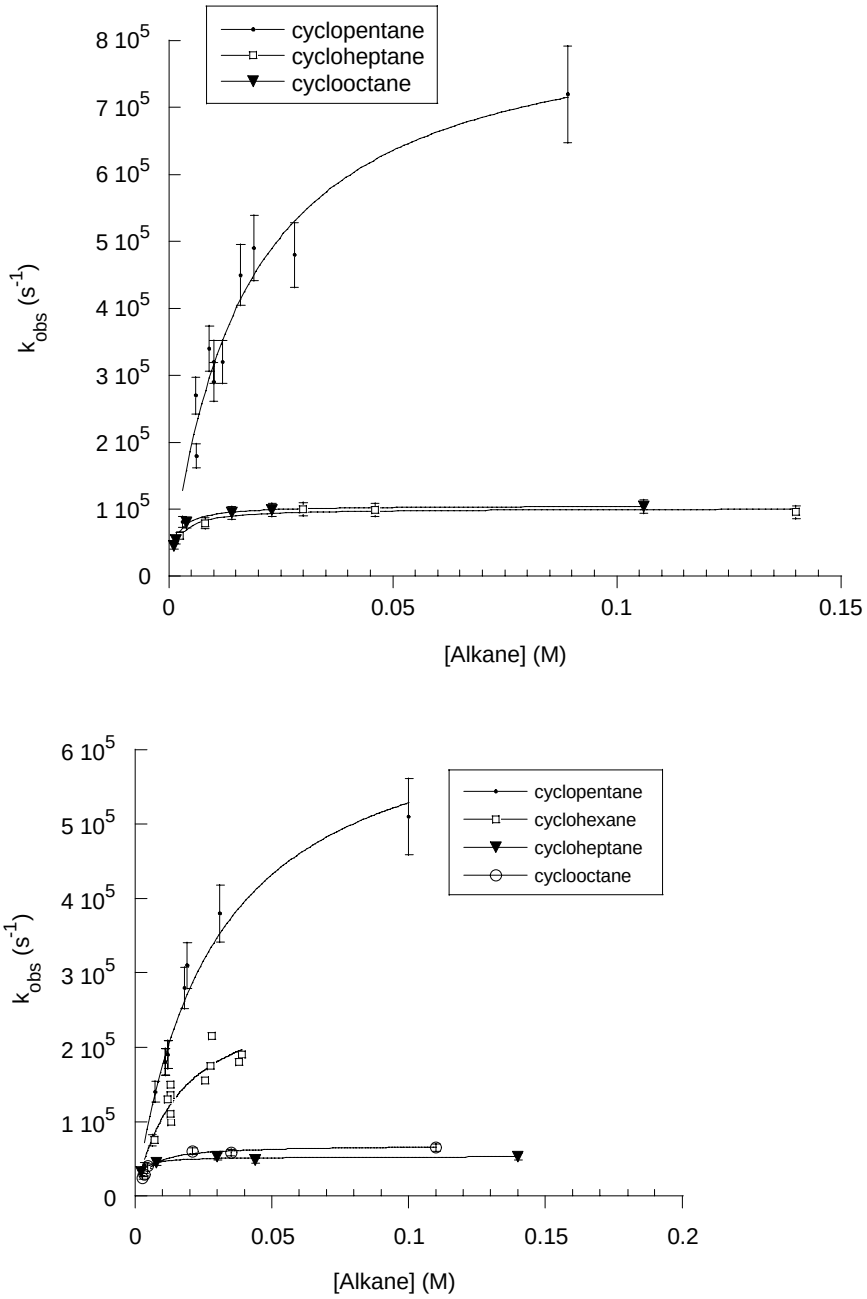

Figure 2.5. Plots of k_{obs} vs. concentration of cyclic alkanes at –80 °C (top) and –90 °C (bottom). The solid lines represent nonlinear least squares fits of the data to eq 2.1. Cyclohexane data at –90 °C are reproduced from Ref. 41.

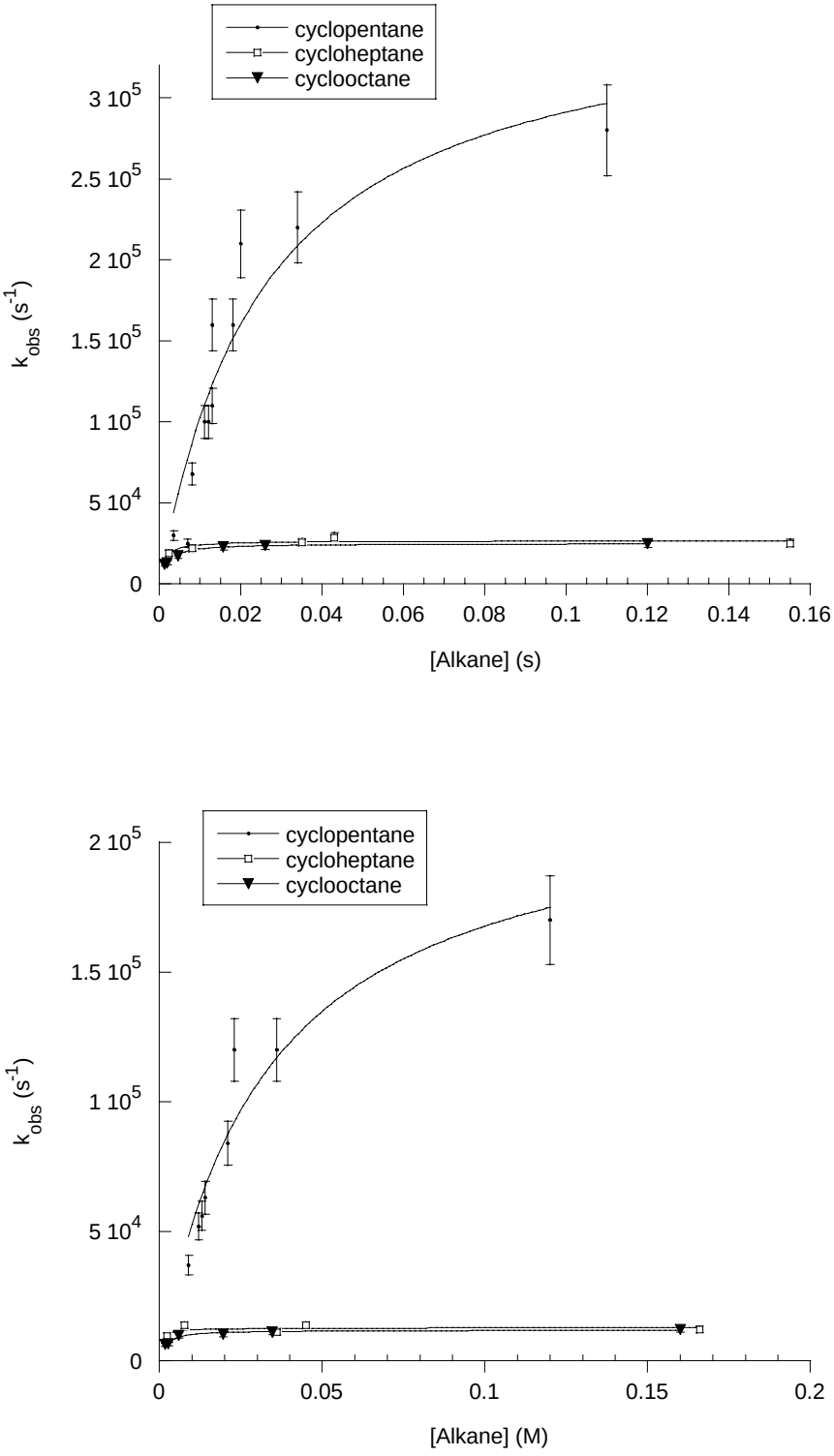

Figure 2.6. Plots of k_{obs} vs. concentration of cyclic alkanes at –100 °C (top) and –110 °C (bottom). The solid lines represent nonlinear least squares fits of the data to eq 2.1.

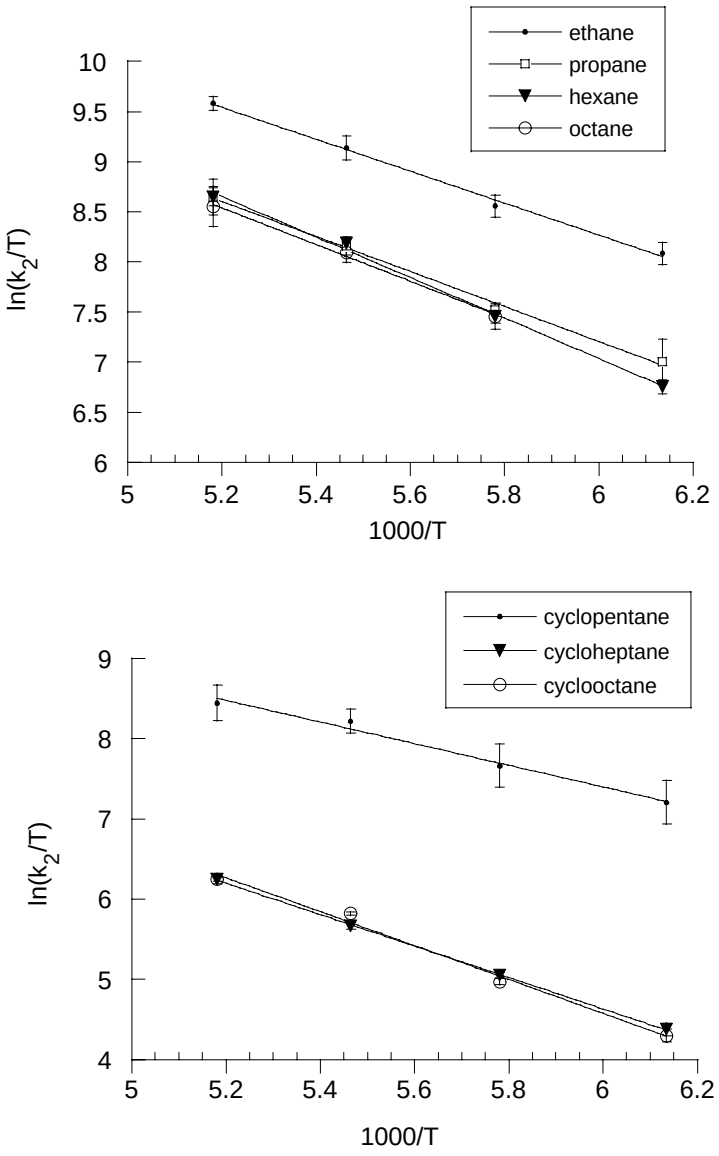

Figure 2.7. Eyring plots of the temperature dependence of k_2 values for the oxidative addition of linear alkanes (top) and cyclic alkanes (bottom) to the Cp*Rh(CO) fragment in the temperature range from –80 °C to –110 °C.

Table 2.2. Equilibrium and Rate Constants for Reaction of Alkanes with **1** in Liquid Kr[a]

Alkane	K_{eq}	k_2 (10^5 s^{-1})	K_{eq}	k_2 (10^5 s^{-1})
	-80 °C		-90 °C	
Ethane	14 ± 1	28 ± 2	13 ± 1	17 ± 2
Propane	140 ± 10	11 ± 1	140 ± 10	6.4 ± 0.6
Hexane	350 ± 50	11 ± 2	340 ± 20	6.6 ± 0.4
Octane	400 ± 100	10 ± 1	500 ± 100	6.0 ± 0.3
Cyclopentane	1200 ± 300	8.5 ± 1	800 ± 100	6.8 ± 1
Cyclohexane[b]	900 ± 200	7.0 ± 0.8	1500 ± 300	2.8 ± 0.3
Cycloheptane	12,000 ± 2000	1.0 ± 0.06	15,000 ± 3000	0.53 ± 0.02
Cyclooctane	15,000 ± 1000	1.0 ± 0.02	15,000 ± 1000	0.62 ± 0.01
	-100 °C		-110 °C	
Ethane	12 ± 1	9 ± 1	11 ± 1	5.3 ± 0.6
Propane	120 ± 10	3.2 ± 0.2	120 ± 20	1.8 ± 0.4
Hexane	330 ± 20	3.0 ± 0.2	320 ± 30	1.4 ± 0.1
Octane	600 ± 100	3.0 ± 0.2	[d]	[d]
Cyclopentane	900 ± 250	3.7 ± 1	800 ± 200	2.2 ± 0.6
Cyclohexane	2000 ± 500	1.2 ± 0.1	1500 ± 300	0.69 ± 0.06
Cycloheptane	[c]	0.27 ± 0.01	[c]	0.13 ± 0.01
Cyclooctane	14,000 ± 1000	0.25 ± 0.01	13,000 ± 2000	0.12 ± 0.01

a) Errors represent ± σ.

b) Ref. 41.

c) Rate saturation occurred at such low [cycloheptane] that the data did not afford meaningful K_{eq} values.

d) Octane was insufficiently soluble in Kr at –110 °C to permit kinetic measurements.

Table 2.3. Activation Parameters for Oxidative Addition of Alkanes to the Cp*Rh(CO) Fragment

Alkane	$\Delta H^{\ddagger}$ (kcal/mol)	$\Delta S^{\ddagger}$ (cal/mol•K)
Ethane	3.6 ± 0.4	-9 ± 3
Propane	3.9 ± 0.4	-10 ± 2
Hexane	4.6 ± 0.6	-8 ± 3
Octane	3.6 ± 1	-11 ± 6
Cyclopentane	2.7 ± 1	-16 ± 5
Cyclohexane[b]	4.6 ± 0.6	-7 ± 6
Cycloheptane	3.9 ± 0.4	-12 ± 2
Cyclooctane	4.6 ± 0.4	-11 ± 2

a) Errors represent ± σ. b) Ref. 41

Table 2.2 shows the K_{eq} and k_2 values extracted from the plots in Figures 2.3-2.6. Eyring plots of the temperature dependence of k_2 (Figure 2.7) afford activation parameters for the oxidative addition step; these are summarized in Table 2.3. The errors in K_{eq} values are sufficiently large relative to the variation of these values with temperature that we felt a rigorous van't Hoff treatment was not warranted. We note only that for every alkane studied, van't Hoff analysis yields a *positive* entropy change in the direction of the alkane complex, with values ranging from approximately 5-20 eu.

Photolysis of 1 in liquid xenon/alkane solutions. As shown previously in our group, photolysis of **1** in pure liquid xenon produces a transient species absorbing at 1941 cm^{-1}. At -80 °C this transient is longer lived than the analogous Kr species and has been assigned to the xenon solvate, Cp*Rh(CO)•Xe.[41] We have observed in the present study that photolysis of **1** in mixtures of xenon/methane, xenon/ethane or xenon/propane leads only to the single transient band at 1941 cm^{-1}. Moreover, the decay of this absorbance appears to remain unchanged from that in pure liquid Xe, even at relatively high concentrations of alkane. In contrast, upon photolysis of **1** in Xe solutions containing butane and larger alkanes, rates of decay of the 1941 cm^{-1} absorption increase with increasing alkane concentration. Furthermore, absorption by an alkyl hydride product, Cp*Rh(CO)(alkyl)(H), is observed in the 2000 cm^{-1} region. Kinetic data for the reaction of **1** with cyclohexane in liquid Xe were published in an earlier study.[41]

Discussion

Trends in the pre-equilibrium binding of alkanes to Rh. The data reported here supplement our earlier studies, in which rates were measured for the photoinduced reaction of **1** in rare gas solutions of cyclohexane and neopentane. When the data are considered as a whole, the clearest trend that emerges is a shift in the pre-equilibrium from the krypton complex toward the alkane complex as alkane size increases. This effect is precedented in a study by Rayner, Hackett, and co-workers on alkane binding

affinities toward photogenerated $W(CO)_5$ in the gas phase.[50] In contrast to the rhodium system studied here, the electronically unsaturated tungsten complex does not induce oxidative addition of C-H bonds, but rather forms transiently stable alkane adducts of the type postulated in the rhodium pre-equilibrium (Scheme 2.2). The Rayner study demonstrated that the equilibrium between naked $W(CO)_5$ and $W(CO)_5$(alkane) shifts toward the alkane complex as alkane size increases. The hydrocarbons in that study ranged in size from methane to hexane and cyclohexane, and the magnitudes of increase in the observed equilibrium constants agree reasonably well with those reported here. Significantly, methane appeared not to bind to the tungsten species at all, consistent with our failure to observe any interaction between methane and the Rh-Kr solvate.

The authors of the tungsten study attributed the size effect to improved orbital interaction between the LUMO on tungsten and the C-H σ molecular orbital on the alkane. They argued that as alkane size increases, so, too, does the energy of the C-H σ MO (as determined by photoelectron spectroscopy); as a result, the energy gap shrinks between this orbital and the tungsten LUMO, leading to a more favorable W-alkane interaction. Table 2.4 lists the first ionization potentials for each alkane considered in the present study.[51-54] The values decrease with increasing alkane size, indicative of rising orbital energies.

Table 2.4. Rare Gas and Alkane Ionization Potentials and Polarizabilities and Free Energies for the Kr/Alkane Complex Equilibria at –90 °C

Substrate	First IP (eV)	Polarizability[e] ($Å^3$)	$\Delta G_{183\,K}$ (kcal/mol)
Kr	14.00[a]	2.74	–
Xe	12.13[a]	4.46	–
Methane	12.75[b]	2.61	> 0
Ethane	11.56[b]	4.5	-0.9
Propane	10.9[b]	6.36	-1.8
Hexane	9.97[c]	11.9	-2.1
Octane	9.71[d]	15.6	-2.3
Cyclopentane	10.33[d]	9.11	-2.4
Cyclohexane	9.82[c]	10.96	-2.6
Cycloheptane	9.96[c]	12.1	-3.5
Cyclooctane	9.75[c]	13.9	-3.5

a) Ref. 51. b) Ref. 52. c) Ref. 53. d) Ref. 54. e) Ref. 58.

The above argument is consistent with treating the metal-alkane interaction as fundamentally "soft", in accordance with hard/soft acid base principles.[55,56] The small (or nonexistent) dipole moments, low basicities, and high ionization potentials associated with alkanes and with the larger noble gases lend prominence to an induced distortion of electron clouds in the bonding between these weak ligands and transition metal centers.[57] Binding affinities should then correlate with polarizabilities. As the polarizability of the ligand increases, so, too, should the strength of interaction between that ligand and the soft metal center. The polarizabilities of Kr, Xe, and the alkanes employed as substrates are also listed in Table 2.4, accompanied by the free energies characterizing the pre-equilibria at -90 °C.[58] It is noteworthy that Kr and methane have comparable polarizabilities, as do Xe, ethane, and propane. These numbers support the hypothesis that coordinative competition between hydrocarbons and rare gas atoms for the unsaturated rhodium center is influenced by the relative polarizabilities of these ligands. Thus methane does not effectively compete with the equally polarizable Kr, given that

the Kr is present in ten- to thousandfold excess, and similarly ethane and propane compete poorly with excess Xe. In contrast, the larger, softer, more polarizable alkanes interact more strongly with the unsaturated Rh center than do the rare gas atoms, and thus the equilibria are driven toward the alkane complexes.

For propane, hexane, and octane, binding affinities correlate well with polarizability. However, the cyclic alkanes uniformly exhibit higher K_{eq} values than their linear counterparts, despite comparable polarizabilities. Furthermore, the increase in polarizability with carbon number is roughly constant, whereas the data evidence a large discontinuity in the relative K_{eq} values between cyclopentane and cyclooctane. Clearly alternative physical phenomena augment polarizability in determining the binding energetics of cyclic substrates.

It is likely that complex steric and conformational factors influence the particularly strong affinity of the Rh center toward the seven- and eight-membered rings. Van der waals attractions between the Rh fragment and distant sites on these larger hydrocarbons may be significant in this regard. Solvent effects may also play a strong role in the equilibrium between the Kr and alkane complexes. In fact it is plausible that our measured binding energies, to a large extent, simply reflect differential solvation of the alkanes in krypton. From an entropic standpoint, binding of the alkane to the Rh center should liberate a number of krypton atoms associated with solvation of the free alkane. As alkane size increases, liberation of these Kr atoms should become increasingly entropically favorable, thus driving the equilibrium toward the metal-alkane complex. This argument is consistent with the positive entropy changes suggested by van't Hoff analysis. Changes in solvation enthalpies for the free alkanes and Rh-alkane complexes could contribute as well. Despite careful consideration of the data, however, a compelling physical model that accounts for all of the binding phenomena remains elusive.

Rates of oxidative addition. The dependence of the k_2 values, reflecting elementary rates of C-H oxidative addition, on alkane structure is roughly opposite to that observed for the binding constants. Thus the ethane reaction is rapid, while longer linear alkanes react at similar, slower rates. Cyclic alkanes react more slowly than their linear counterparts, and the reactions of cycloheptane and cyclooctane are remarkably slow.[59]

It seems most straightforward to interpret this trend as a ground state effect resulting from the same factors that influence binding in the pre-equilibrium. This is illustrated in Figure 2.8, which shows a proposed reaction coordinate diagram for the reactions of **1** with cyclopentane and with cyclooctane at –90 °C. The strong binding of cyclooctane relative to cyclopentane places the Rh-C_8H_{16} complex 1.1 kcal/mole lower in energy than the Rh-C_5H_{10} complex. Whatever the cause of this strong binding, some of it seems to be lost in going from each alkane complex to the corresponding C-H activation transition state. That is, the free energy gap between alkane complexes ($\Delta\Delta G$) is larger than the gap between transition states for oxidative addition ($\Delta\Delta G^{\ddagger}$). Thus the transition states for oxidative addition of the different alkanes lie closer together in energy than do the respective precursor alkane complexes, and the rate of oxidative addition is therefore slowest for the most strongly-bound alkanes. The logic of this argument suggests that oxidative addition of methane from the alkane complex may proceed with the smallest relative barrier. However, in contrast to the other alkane complexes, the Rh-CH_4 complex appears to lie higher in energy than the krypton complex; consequently it forms in such low abundance that reaction with methane is not observed.

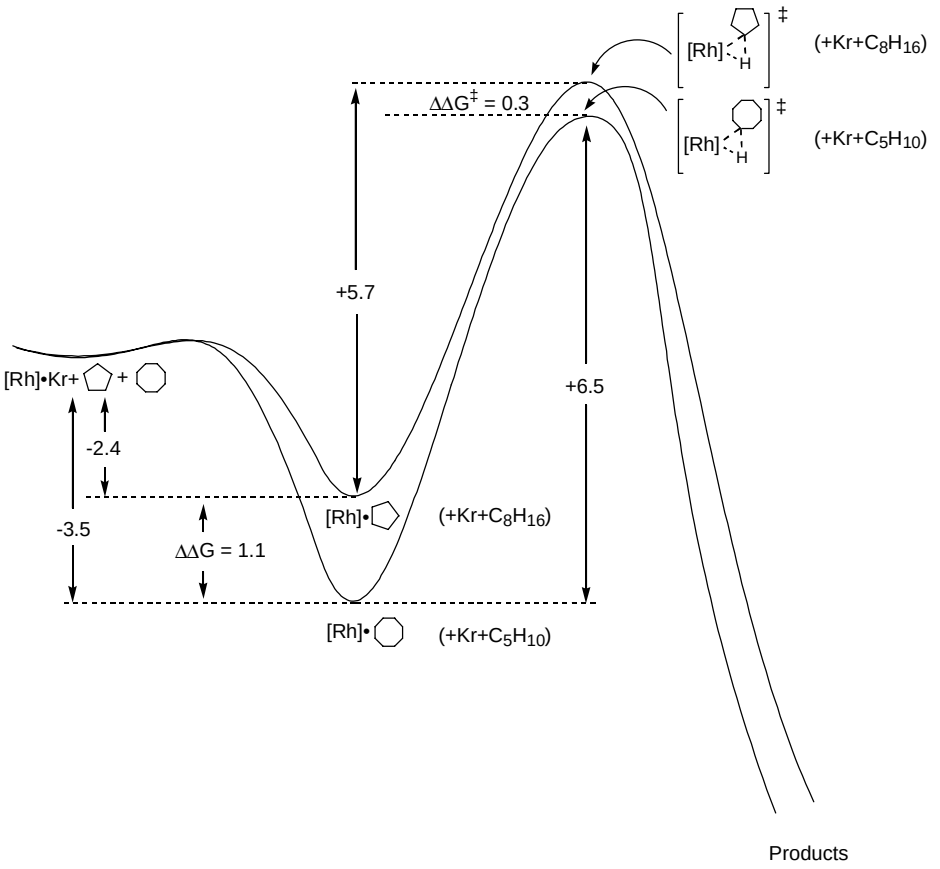

Figure 2.8. Reaction coordinates for reaction of **1** with cyclopentane and with cyclooctane in liquid Kr solution at –90 °C. Free energies listed are in kcal/mol. [Rh] = Cp*Rh(CO). The diagram is not drawn precisely to scale.

Steric factors probably also play a role in determining relative oxidative addition rates. In the cyclic series, the transition states for formation of cycloheptyl and cyclooctyl Rh hydride species may be particularly conformationally demanding. Regarding the trend in the linear series, propane is more hindered than ethane, but the longer chain hydrocarbons may not suffer significantly more hindrance than propane, particularly if activation occurs predominantly at the terminal CH_3 groups. This reasoning is consistent with the similarity in rates for propane, hexane, and octane. Unfortunately, such a hypothesis is difficult to confirm, since the methodology employed in this study does not distinguish between activation at primary and secondary sites.

It was hoped that Eyring analysis of the k_2 data would give further insight into the trend in oxidative addition rates. However, an examination of the activation enthalpies and entropies in Table 2.3 reveals no obvious trend across the full series of hydrocarbons. It is worth noting that: (1) a negative activation entropy is consistent with the stereoelectronic demands of oxidative addition; and (2) the small activation enthalpies (*ca.* 4 kcal/mol) for the cleavage of such strong bonds support significant Rh-C and/or Rh-H interaction in the transition state.

Conclusions

The kinetic data for the photoinduced reaction of $Cp^*Rh(CO)_2$ with linear and cyclic saturated hydrocarbons support a strong influence of alkane structure on the binding affinity of the alkane toward the unsaturated rhodium center in the $Cp^*Rh(CO)$ fragment. In the initially formed alkane or σ-complex, larger alkanes interact more strongly with the Rh fragment than do smaller alkanes. Methane does not appear to bind at all, while ethane binds an order of magnitude less strongly than the longer chain hydrocarbons. Cyclic alkanes appear to bind more strongly than comparably sized linear alkanes. Furthermore, while the binding energetics of cyclopentane and cyclohexane

differ by less than a factor of two, the 7- and 8-membered rings exhibit an order of magnitude greater affinity.

Elementary rates of C-H oxidative addition follow an opposing trend. Thus reaction of the Rh-ethane complex to form Cp*Rh(CO)(ethyl)(H) is most rapid, while reactions of the cycloheptane and cyclooctane complexes are particularly slow. It is likely that solvent effects in the noble gas media play a significant role in the above trends. Nonetheless, the results highlight the general importance of treating C-H bond activation at late metal centers as a two-step process, with potentially different factors influencing the binding and activation steps.

Notes and References

1) Olah, G. A.; Molnar, A. *Hydrocarbon Chemistry*; Wiley: New York, 1995.

2) Shilov, A. E.; Shul'pin, G. B. *Activation and Catalytic Reactions of Saturated Hydrocarbons in the Presence of Metal Complexes*; Kluwer: Boston, 2000.

3) Janowicz, A. H.; Bergman, R. G. *J. Am. Chem. Soc.* **1982**, *104*, 352.

4) Hoyano, J. K.; Graham, W. A. G. *J. Am. Chem. Soc.* **1982**, *104*, 3723.

5) Jones, W. D.; Feher, F. J. *Organometallics* **1983**, *2*, 562.

6) Periana, R. A.; Bergman, R. G. *Oganometallics* **1984**, *3*, 508.

7) Rest, A. J.; Whitewell, I.; Graham, W. A. G.; Hoyano, J. K.; McMaster, A. D. *J. Chem. Soc., Dalton Trans.* **1987**, 1181.

8) Recent reviews include this and the subsequent two references: Stahl, S. S.; Labinger, J. A.; Bercaw, J. E. *Angew. Chem., Int. Ed. Eng.* **1998**, *37*, 2181.

9) Shilov, A. E.; Shulpin, G. B. *Chem. Rev.* **1997**, *97*, 2879.

10) Arndtsen, B. A.; Bergman, R. G.; Mobley, T. A.; Peterson, T. H. *Acc. Chem. Res.* **1995**, *28*, 154.

11) Recent examples of alkane functionalization via transition metal C-H activation include this and the subsequent three references: Chen, H.; Schlecht, S.; Semple, T. C.; Hartwig, J. F. *Science* **2000**, *287*, 1995.

12) Liu, F. C.; Goldman, A. S. *Chem. Commun.* **1999**, *7*, 655.

13) Periana, R. A.; Taube, D. J.; Gamble, S.; Taube, H.; Satoh, T.; Fujii, H. *Science* **1998**, *280*, 560.

14) Sen, A. *Acc. Chem. Res.* **1998**, *31*, 550.

15) Ti: Bennett, J. L.; Wolczanski, P. T. *J. Am. Chem. Soc.* **1997**, *119*, 10696.

16) Re: Jones, W. D.; Rosini, G. P.; Maguire, J. A. *Organometallics* **1999**, *18*, 1754.

17) Re: Brown, S. N.; Myers, A. W.; Fulton, J. R.; Mayer, J. M. *Organometallics* **1998**, *17*, 3364.

18) Os: Osman, R.; Pattison, D. I.; Perutz, R. N.; Bianchini, C.; Casares, J. A.; Peruzzini, M. *J. Am. Chem. Soc.* **1997**, *119*, 8459.

19) Rh: Wick, D. D.; Reynolds, K. A.; Jones, W. D. *J. Am. Chem. Soc.* **1999**, *121*, 3974.

20) Rh: Bromberg, S. E.; Yang, H.; Asplund, M. C.; Lian, T.; McNamara, B. K.; Kotz, K. T.; Yeston, J. S.; Wilkens, M.; Frei, H.; Bergman, R. G.; Harris, C. B. *Science* **1997**, *278*, 260.

21) Ir: Mobley, T. A.; Schade, C.; Bergman, R. G. *Organometallics* **1998**, *17*, 3574.

22) Pt: Fekl, U.; Zahl, A.; van Eldik, R. *Organometallics* **1999**, *18*, 4156.

23) Pt: Wick, D. D.; Goldberg, K. I. *J. Am. Chem. Soc.* **1997**, *119*, 10235.

24) Pt: Stahl, S. S.; Labinger, J. A.; Bercaw, J. E. *J. Am. Chem. Soc.* **1996**, *118*, 5961.

25) Recent theoretical studies include this and the subsequent five references: Su, M. D.; Chu, S. Y. *Chem.-Eur. J.* **1999**, *5*, 198.

26) Su, M. D.; Chu, S. Y. *International Journal of Quantum Chemistry* **1998**, *70*, 961.

27) Su, M. D.; Chu, S. Y. *J. Phys. Chem. A* **1997**, *101*, 6798SEP 4.

28) Zaric, S.; Hall, M. B. *J. Phys. Chem. A* **1998**, *102*, 1963.

29) Wittborn, A. M. C.; Costas, M.; Blomberg, M. R. A.; Siegbahn, P. E. M. *J. Chem. Phys.* **1997**, *107*, 4318.

30) Siegbahn, P. E. M. *J. Am. Chem. Soc.* **1996**, *118*, 1487.

31) Hall, C.; Perutz, R. N. *Chem. Rev.* **1996**, *96*, 3125 and references therein.

32) Grills, D. C.; Sun, X. Z.; Childs, G. I.; George, M. W. *J. Phys. Chem. A* **2000**, *104*, 4300.

33) Geftakis, S.; Ball, G. E. *J. Am. Chem. Soc.* **1998**, *120*, 9953.

34) Gross, C. L.; Girolami, G. S. *J. Am. Chem. Soc.* **1998**, *120*, 6605.

35) Schafer, D. F.; Wolczanski, P. T. *J. Am. Chem. Soc.* **1998**, *120*, 4881.

36) Periana, R. A.; Bergman, R. G. *J. Am. Chem. Soc.* **1986**, *108*, 7332.

37) Buchanan, J. M.; Stryker, J. M.; Bergman, R. G. *J. Am. Chem. Soc.* **1986**, *108*, 1537.

38) Bromberg, S. E.; Lian, T. Q.; Bergman, R. G.; Harris, C. B. *J. Am. Chem. Soc.* **1996**, *118*, 2069.

39) Weiller, B. H.; Wasserman, E. P.; Bergman, R. G.; Moore, C. B.; Pimentel, G. C. *J. Am. Chem. Soc.* **1989**, *111*, 8288.

40) Bengali, A. A.; Schultz, R. H.; Moore, C. B.; Bergman, R. G. *J. Am. Chem. Soc.* **1994**, *116*, 9585.

41) Schultz, R. H.; Bengali, A. A.; Tauber, M. J.; Weiller, B. H.; Wasserman, E. P.; Kyle, K. R.; Moore, C. B.; Bergman, R. G. *J. Am. Chem. Soc.* **1994**, *116*, 7369.

42) Kang, J. W.; Maitlis, P. M. *J. Organomet. Chem.* **1971**, *26*, 393.

43) For another example of temperature-dependent alkane IR band intensities, see: Snyder, R. G.; Maroncelli, M.; Strauss, H. L.; Hallmark, V. M. *J. Phys. Chem.* **1986**, *90*, 5623.

44) For a thermodynamic study of binary ethane/Kr mixtures, see: Calado, J. C. G.; Chang, E.; Clancy, P.; Street, W. B. *J. Chem. Phys*, **1987**, *91*, 3914.

45) Gomes de Azevado, E. J. S.; Calado, J. C. G. *Fluid Phase Equilibria* **1991**, *90*, 215.

46) Literature values for liquid Kr densities support a 17% density increase from –80 °C to –110 °C at the pressures pertaining in our experiments: Street, W. B.; Staveley, L. A. K. *J. Chem. Phys.* **1971**, *55*, 2495.

47) The kinetics data for ethane, propane, and hexane and all data in liquid xenon were collected by Dr. Bruce McNamara but have been included here for completeness.

48) At higher concentrations of methane, the solution became opaque in the IR region of interest, precluding a spectroscopic study.

49) Kinetic studies with cyclopropane and cyclobutane as substrates were not undertaken because of potential complications arising from the observation of C-C activation of these strained rings by a related rhodium complex. See: Periana, R. A.; Bergman, R. G. *J. Am. Chem. Soc.* **1986**, *108*, 7346.

50) Brown, C. E.; Ishikawa, Y.; Hackett, P. A.; Rayner, D. M. *J. Am. Chem. Soc.* **1990**, *112*, 2530.

51) Kimura, K.; Katsumata, S.; Achiba, Y.; Yamazaki, T.; Iwata, S. "Ionization Energies, Ab Initio Assignments, and Valence Electronic Structure for 200 Molecules" in *Handbook of HeI Photoelectronic Spectra of Fundamental Organic Compounds*; Japan Scientific Society Press: Tokyo, 1981.

52) Bieri, G.; Burger, F.; Heilbronner, E.; Maier, J. P. *Helv. Chim. Acta* **1977**, *60*, 2213.

53) Sieck, L. W.; Mautner (Meot-Ner), M. *J. Phys. Chem.* **1982**, *86*, 3646.

54) Mautner (Meot-Ner), M.; Sieck, L. W.; Ausloos, P. *J. Am. Chem. Soc.* **1981**, *103*, 5342.

55) Parr, R. G.; Pearson, R. G. *J. Am. Chem. Soc.* **1983**, *105*, 7512.

56) Pearson, R. G. *J. Am. Chem. Soc.* **1988**, *110*, 7684.

57) For a theoretical treatment of the bonding in transition metal rare gas complexes, see: Ehlers, A. W.; Frenking, G.; Baerends, E. J. *Organometallics* **1997**, *16*, 4896.

58)Applequist, J. *J. Phys. Chem.* **1993**, *97*, 6016 and references therein.

59) Compensating variations in the parameters of a dual parameter fit can sometimes simply be artifacts of the fitting equation. In this case, however, we directly observe saturation behavior, and we are therefore confident that physical phenomena differentiate the rates and equilibria in, for example, the cyclohexane and cycloheptane reactions.

Chapter 2 Appendix

Derivation of the Rate Expression in eq 2.1.

The expression in eq 1 can be derived by assuming a rapid pre-equilibrium between the Rh-Kr solvate **2** and Rh-alkane solvate **3** prior to formation of product **4**. It is also assumed that alkane (R-H) and Kr concentrations remain constant throughout the reaction, since both are present in large excess.The overall rate is given by:

$$\frac{d[\mathbf{4}]}{dt} = k_2[\mathbf{3}]$$

With a rapid pre-equilibrium, $[\mathbf{2}] = \frac{[\mathbf{3}][\mathrm{Kr}]}{K_{eq}[\mathrm{R\text{-}H}]}$

The rate can then be expressed as a function of the total concentration of both solvates:

$$[\mathbf{2}+\mathbf{3}] = [\mathbf{3}]\left(1 + \frac{[\mathrm{Kr}]}{K_{eq}[\mathrm{R\text{-}H}]}\right) \quad \text{so} \quad [\mathbf{3}] = [\mathbf{2}+\mathbf{3}]\left(\frac{K_{eq}[\mathrm{R\text{-}H}]}{K_{eq}[\mathrm{R\text{-}H}] + [\mathrm{Kr}]}\right)$$

$$\frac{d[\mathbf{4}]}{dt} = \left(\frac{k_2 K_{eq}[\mathrm{R\text{-}H}]}{K_{eq}[\mathrm{R\text{-}H}] + [\mathrm{Kr}]}\right)[\mathbf{2}+\mathbf{3}]$$

Dividing numerator and denominator by K_{eq} yields the expression for k_{obs} given in eq 1.

The above derivation differs from the traditional Michaelis-Menten model in that it employs a rapid pre-equilibrium assumption, rather than a steady-state assumption. For a good discussion of the Michaelis-Menten kinetic model, as well as the steady-state and rapid pre-equilibrium assumptions, see: Espenson, J. H. *Chemical Kinetics and Reaction Mechanisms, 2nd Ed.;* McGraw-Hill Inc.: New York, 1995, Ch. 4.

Chapter 3. Flash Infrared Kinetics of the Photochemistry of $Tp^*Rh(CO)_2$ and $Bp^*Rh(CO)_2$ in Liquid Xenon Solution

Introduction

The [hydridotris(3,5-dimethylpyrazolyl)borato]dicarbonyl rhodium complex ($Tp^*Rh(CO)_2$, **5**) was shown by Hoyano and Graham to undergo exceptionally photoefficient C-H activation with aliphatic hydrocarbons (eq 3.1).[1-5]

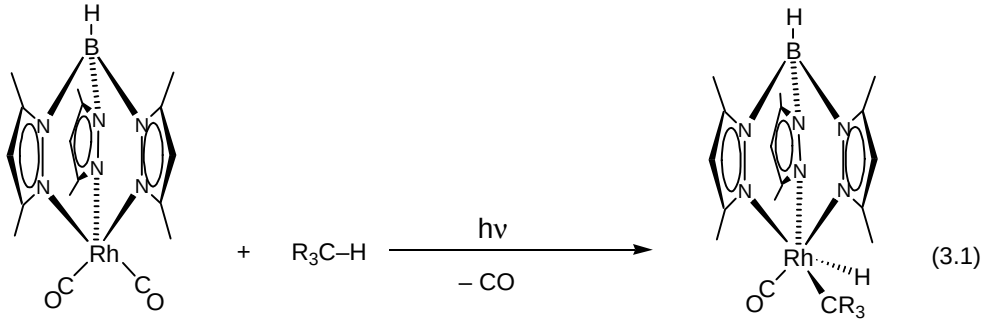

(3.1)

5 **8**

Quantitative measurements in various alkane solvents by Lees and co-workers revealed quantum yields for this reaction in excess of 30 %.[6,7] We therefore chose complex **5** to be the focus of a collaborative study with the C. B. Harris group, the goal of which was to examine the kinetics of C-H bond activation in room-temperature alkane solvent on a picosecond timescale.

Bromberg *et al.* recently published the study, showing that photoextrusion of CO from **5** in cyclohexane solvent leads to two successive, spectroscopically characterized

Scheme 3.1

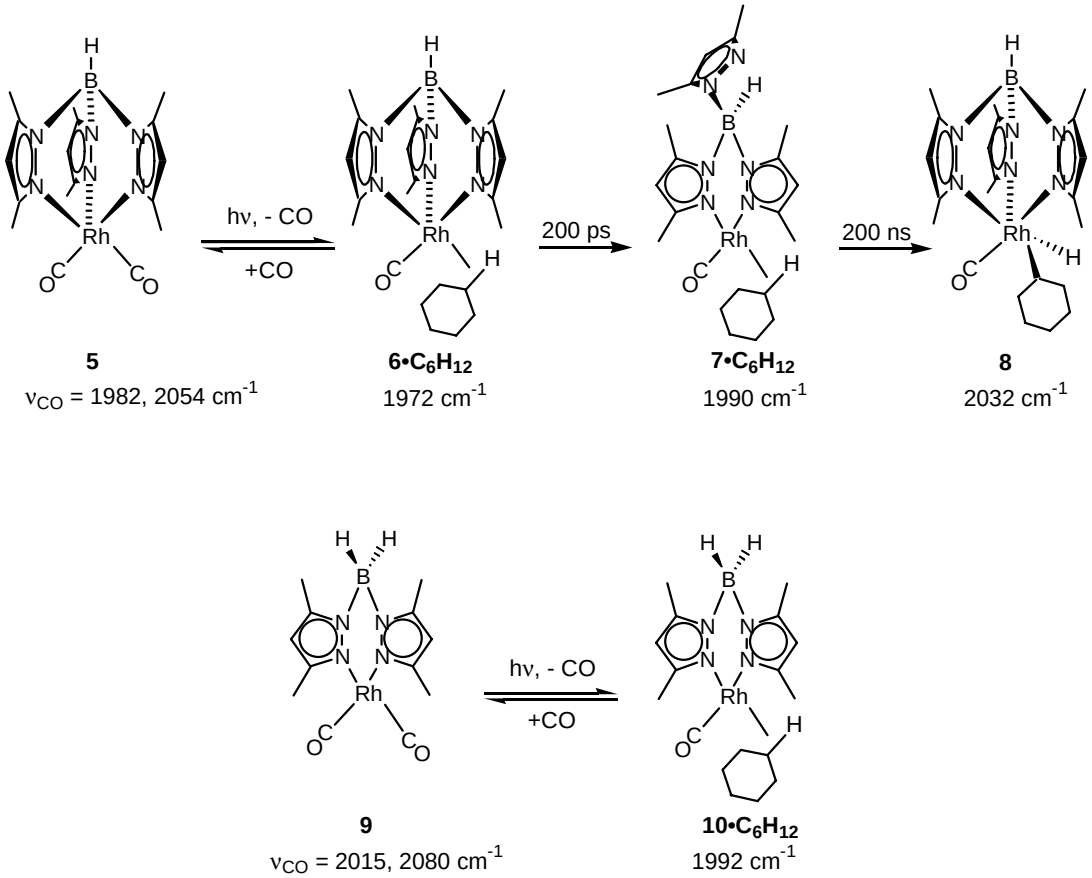

intermediates prior to formation of the Rh alkyl hydride product **8** on a nanosecond timescale.[8] These intermediates (**6•C$_6$H$_{12}$**, **7•C$_6$H$_{12}$**) were proposed to be η^3- and η^2-Tp*Rh(CO) alkane solvates, respectively, differing in the number of pyrazolyl nitrogens coordinated to the metal center (Scheme 3.1). The structural assignments were based in large part on studies of the related bidentate [dihydridobis(3,5-dimethylpyrazolyl)borato] dicarbonyl rhodium complex (Bp*Rh(CO)$_2$, **9**), which was used to model the proposed hapticity change in Tp* coordination to Rh along the C-H activation pathway (Scheme 3.1). An earlier matrix study by Rest and co-workers also examined the photochemistry

of **5** and **9** to probe changes in the coordination geometry of the Tp* ligand after irradiation of **5**.[9]

To complement these studies and to garner further evidence for Tp* hapticity changes in solution, we have employed a UV/IR pump-probe scheme to examine the behavior of **5** and **9** upon photolysis in liquid Xe. Time-resolved infrared spectroscopy of transition metal carbonyls in liquid xenon solution has become a useful method for characterizing the structures and lifetimes of short-lived species.[10-14] The medium is less rigidly confining than a solid matrix and at the same time less reactive than a conventional solvent, although the Xe does appear to stabilize unsaturated metal centers by coordination (bond energies of up to 11 kcal/mol have been measured for such complexes).[15-19] As detailed in the previous chapter, collaborations among the Moore, Bergman, and Pimentel groups have taken advantage of the inertness of Xe to study metal complexes that react rapidly with the C-H bonds in alkanes.[20-27] The photoinduced chemistry of **5** and **9** in liquid Xe solution is described below.

Experimental Methods

The IR flash kinetics apparatus was described in the previous chapter. Transient difference spectra were acquired point-by-point by tuning the diode laser to wavelengths of interest. I_0 values at each wavelength were obtained prior to photolysis by chopping the IR beam at 285 Hz and measuring the signal intensity on the oscilloscope. In the transient spectra and traces presented below, the ordinate represents absorbance change, calculated as log $[I_0/(I_0-I)]$; the ordinate zero therefore refers to zero *change* in absorbance subsequent to UV photolysis and so does not reflect the relative static

absorptions of stable species in the reaction mixture. Exponential fits were refined using a commercially available nonlinear least squares routine (KaleidaGraph, Version 3.0, Synergy Software © 1996). The rate constants were calculated by averaging the values obtained from fits of several traces, and the associated errors represent ±σ about the average value.

Xenon (99.999%) was obtained from Spectra Gases and used as received. Compounds **5**[28] and **9**[29] were prepared using literature methods and stored under dry N_2 prior to use. Reagent concentrations during kinetics experiments were determined by integration of appropriate bands in FTIR spectra using absorption coefficients from gas phase studies (for CO, corrected for index of refraction change in solution)[30] or from spectra of standard solutions prepared in hydrocarbon or chlorinated solvents.

Results

Photochemistry of 5 in Liquid Xe. A xenon solution of Tp*Rh(CO)$_2$ (**5**) (0.1 mM) was irradiated at –50 °C with 20 ns 308 nm pulses. Figure 3.1 shows a transient IR difference spectrum taken 2 μs after the photolysis pulse. The spectrum is characterized by bleaching (diminished intensity) of the parent CO stretching band at 1982-1986 cm^{-1} and by the appearance of two new bands at 1972-1980 cm^{-1} and 1992-2000 cm^{-1}. These transient bands grow in with an instrument-limited risetime of 300 ns, and they both exhibit single exponential decays with rate constants of 2 (± 0.3) x 10^4 s^{-1}.

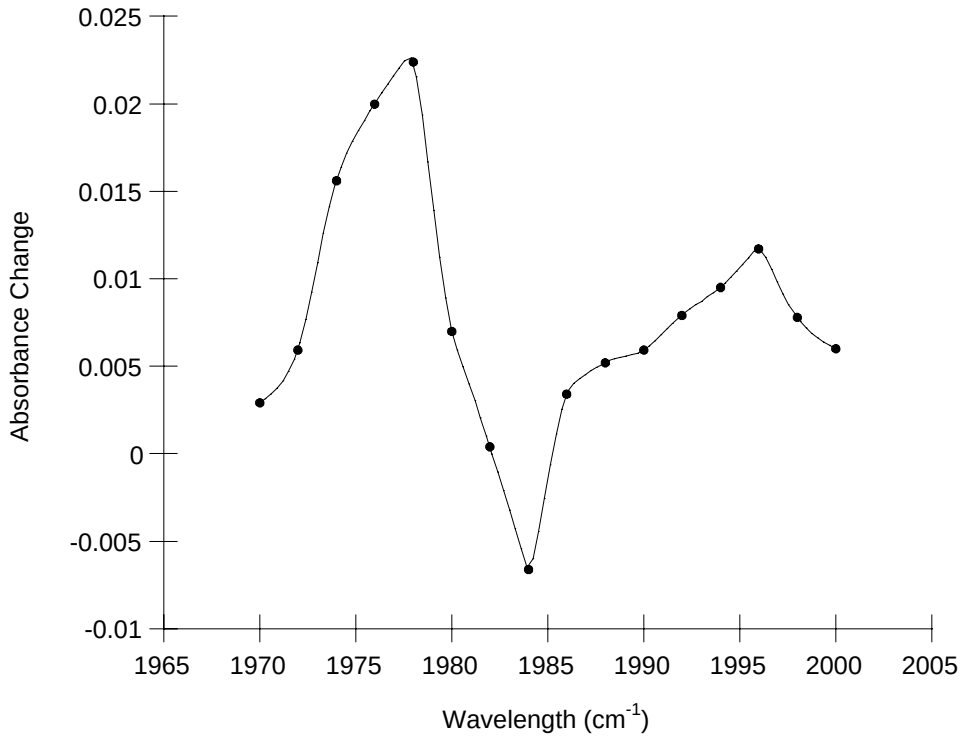

Figure 3.1. Transient IR difference spectrum 2 μs after 308 nm photolysis of **5** in Xe solution.

The data presented in Figure 3.1 do not support a rigorous quantification of the relative intensities of the bands at 1978 and 1996 cm^{-1}. Such treatment is precluded by the steady depletion of substrate during data collection, coupled with power fluctuations and wavelength-dependent signal-to-noise ratios inherent to the probe laser. Consequently, an investigation of the temperature dependence of relative band intensities, leading to an estimate of the free energy gap between the two absorbing species, could not be pursued.

FTIR spectra taken throughout the experiment indicate that **5** decomposes upon photolysis in Xe to yield unknown products. Due to the relatively low solubility of **5** in

Xe, attempts to isolate these products were unsuccessful. Furthermore, no product bands were apparent in FTIR spectra; we observed only disappearance of the CO bands of **5**. Although **5** is more soluble in aromatic and chlorinated solvents than in Xe, photolysis in these solvents results in oxidative addition of C-H or C-Cl bonds across the Rh center, precluding an independent synthesis of the decomposition products formed in Xe.

In an effort to inhibit the decomposition pathway, transient spectra were taken of **5** in Xe solutions containing excess CO (0.4 mM). The 1978 and 1996 cm^{-1} transient bands still appear with instrument-limited risetimes of 300 ns. Both decay with a single exponential rate constant of 2.1 (± 0.2) x 10^5 s^{-1}, while partial recovery of the parent CO band at 1984 cm^{-1} occurs with k = 2.3 (± 0.4) x 10^5 s^{-1}. Traces are shown in Figure 3.2. Under these conditions, the parent CO band recovers only 60 % of its initial intensity, suggesting that some decomposition still occurs.[31]

Figure 3.2 (overleaf). Kinetic traces of the rise and decay of transient absorptions at 1976 cm^{-1} (top) and 1996 cm^{-1} (middle), and of the bleach and recovery of the parent absorption at 1984 cm^{-1} (bottom), after photolysis of **5** in Xe solution buffered with 0.4 mM of CO.

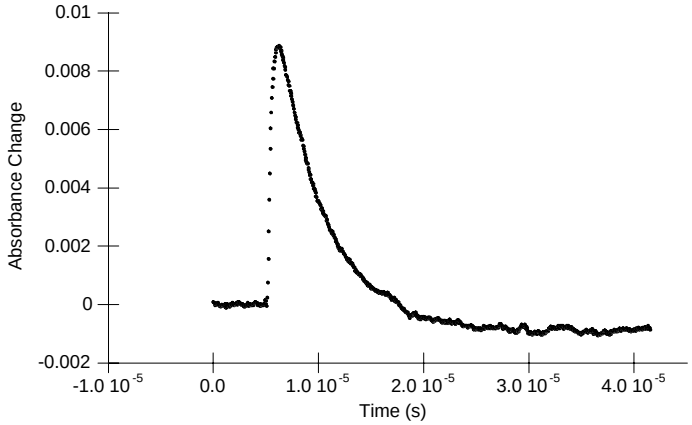
0.01
0.008
0.006
0.004
0.002
0
-0.002
Absorbance Change
-1.0 10-5
0.0
1.0 10-5
2.0 10-5
3.0 10-5
4.0 10-5
Time (s)

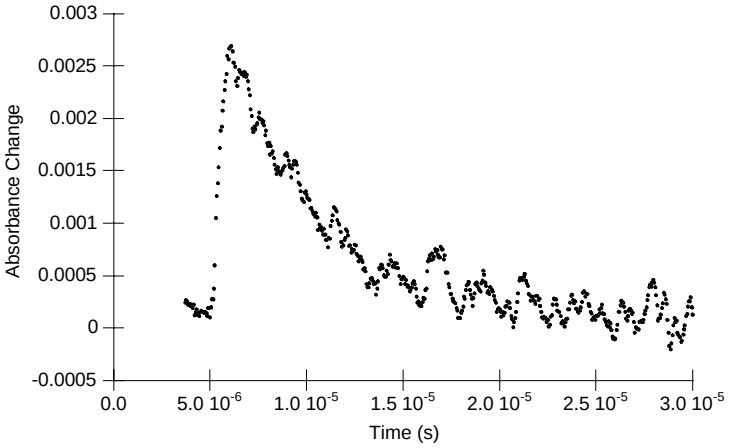
0.003
0.0025
0.002
0.0015
0.001
0.0005
0
-0.0005
Absorbance Change
0.0
5.0 10-6
1.0 10-5
1.5 10-5
2.0 10-5
2.5 10-5
3.0 10-5
Time (s)

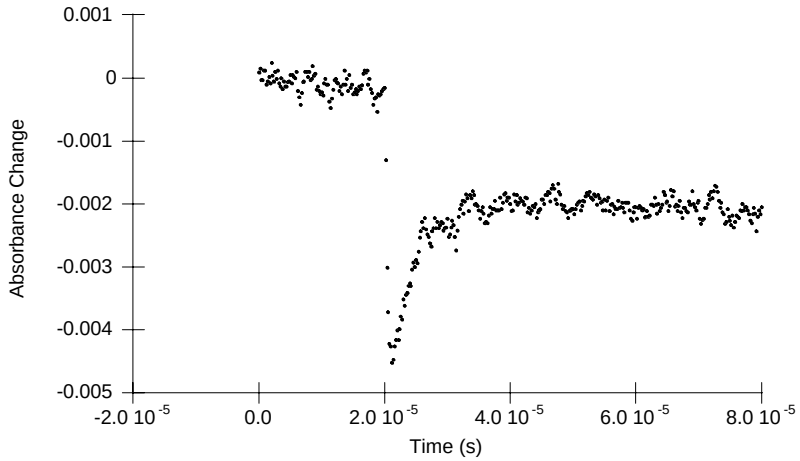
0.001
0
-0.001
-0.002
-0.003
-0.004
-0.005
Absorbance Change
-2.0 10-5
0.0
2.0 10-5
4.0 10-5
6.0 10-5
8.0 10-5
Time (s)

Photochemistry of 5 in Liquid Xe in the Presence of Alkane. The photoinduced reaction of Tp*Rh(CO)$_2$ (**5**) (0.1 mM) with a large excess of cyclohexane (0.32 M) in liquid Xe solution has also been examined. Upon irradiation of the solution at –50 °C, transient peaks still grow in at 1978 and 1996 cm^{-1} concurrent with a bleach of the parent CO band at 1984 cm^{-1}. Both transients exhibit single exponential decays on a microsecond timescale (k_{1978} = 6.9 (± 0.6) x 10^4 s^{-1}, k_{1996} = 7 (± 1.5) x 10^4 s^{-1}). These decays appear to be kinetically coupled to the growth of a new band at 2032 cm^{-1} (k = 7.6 (± 0.7) x 10^4 s^{-1}), which has been assigned to the known CO stretch of the stable C-H activation product Tp*Rh(CO)(cyclohexyl)(H) (**8**).[1] FTIR spectra confirm the conversion of **5** to **8** over the course of the experiment.

Photochemistry of 9 in Liquid Xe. A liquid Xe solution of the related complex Bp*Rh(CO)$_2$ (**9**) (0.3 mM) was also irradiated at –50 °C with 308 nm pulses. A transient difference spectrum is shown in Figure 3.3. The difference spectrum is characterized by a flat baseline in the 1978 cm^{-1} region and a transient band at 1994-2002 cm^{-1}. Bleaching of the parent CO band at 2015 cm^{-1} could not be observed at these experimental conditions because effectively all of the IR power emitted by the diode at that wavelength was absorbed; consequently the change in absorption upon photolysis was not detectable.

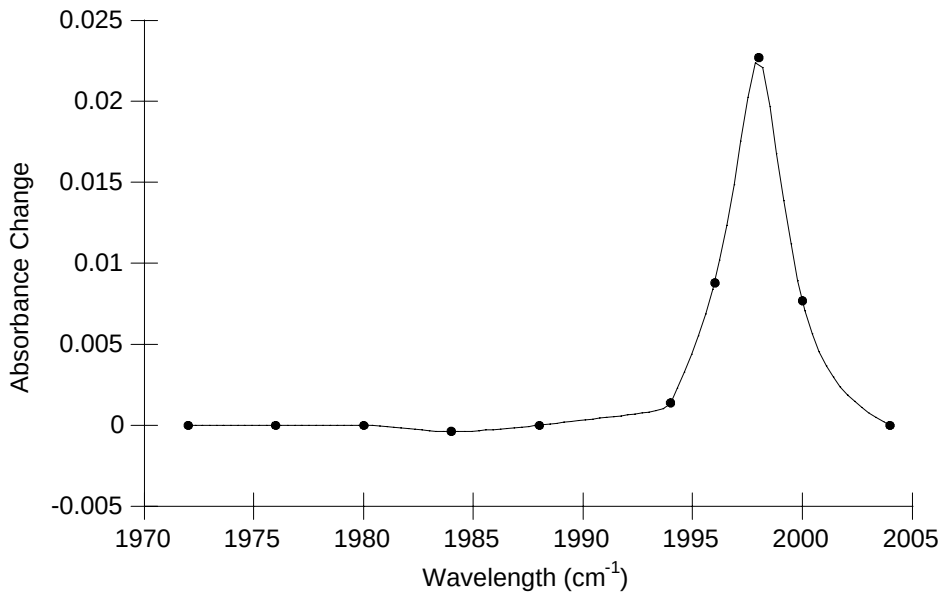

Figure 3.3. Transient IR difference spectrum 2 μs after 308 nm photolysis of **9** in Xe solution.

Like the bands observed upon photolysis of **5**, the absorption band centered at 1998 cm^{-1} grows in with an instrument-limited risetime of 300 ns. The signal then decays with a single exponential rate constant of 4.2 (± 0.3) x 10^3 s^{-1}.[32] In the presence of CO (0.7 mM), the decay of this transient band proceeds an order of magnitude more rapidly (k = 7.7 (± 0.9) x 10^4 s^{-1}).

Photochemistry of 9 in Liquid Xe in the Presence of a Trap. Several attempts were made to photolyze **9** in Xe solution in the presence of free dimethylpyrazole, with the expectation that the base would bind to the transient photoproduct and thereby mimic a species produced upon photolysis of **5**. However, the solubility of dimethylpyrazole in xenon was insufficient to yield conclusive results. We therefore switched to pyridine (py) as the trapping agent. In the presence of pyridine (0.03 M), photolysis of **9** in Xe

solution does in fact lead to the appearance of a new absorption band centered at 1978 cm^{-1}, which grows in with a pseudo-first order rate constant of 1.26 (± 0.04) x 10^4 s^{-1}. The transient band at 1998 cm^{-1} decays concurrently with an exponential rate constant of 1.4 (± 0.1) x 10^4 s^{-1}. Static FTIR spectra demonstrate that the 1978 cm^{-1} band results from absorption by a stable product, Bp*Rh(CO)(py) (**11**), which we were able to independently prepare and characterize. Details of the reaction chemistry of this complex are given in the next chapter.

Discussion

Photolysis of Tp* complex **5** at 308 nm in liquid Xe results in two transient IR bands in the CO stretching region, centered at 1978 and 1996 cm^{-1}. The order of magnitude increase in decay rates upon addition of excess CO, coupled with the similarity in the decay rates of the transients and the recovery rate of the parent, offers compelling evidence that the complex or complexes responsible for these bands are produced via photodissociation of CO from **5**. We have assigned these bands to η^3- and η^2-Tp*Rh(CO)•Xe solvates (**6•Xe** and **7•Xe**), respectively (eq 3.2).

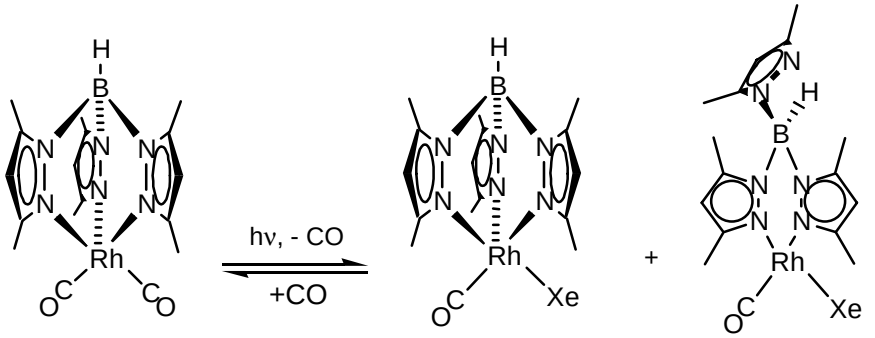

5 ν_{CO} = 1982, 2054 cm^{-1} **6•Xe** 1978 cm^{-1} **7•Xe** 1996 cm^{-1} (3.2)

Consistent with these structural assignments, the lower coordination number of **7** reduces electron density at the metal and thereby accounts for the spectroscopic blue-shift from 1978 cm^{-1} to 1996 cm^{-1} for this complex.

There is ample literature precedent for variation in the hapticity of the Tp* ligand in Rh complexes.[9,33-36] Moreover, the photochemistry of **9** in liquid Xe lends strong support to the hypothesis. The band at 1998 cm^{-1} produced upon photolysis of **9** is most logically assigned to a Bp*Rh(CO)•Xe solvate **10•Xe**, which bears significant structural resemblance to the proposed η^2-Tp* solvate **7•Xe** (1996 cm^{-1}). Binding of a pyridine ligand to **10** (eq 3.3) produces a complex that is structurally analogous to the η^3-Tp* solvate **6**, and both species exhibit CO stretching frequencies of 1978 cm^{-1}. These results (summarized in Table 3.1) strongly reinforce the structural assignments of **6•Xe** and **7•Xe** to the transient species formed upon photolysis of $Tp^*Rh(CO)_2$ (**5**) in liquid xenon.

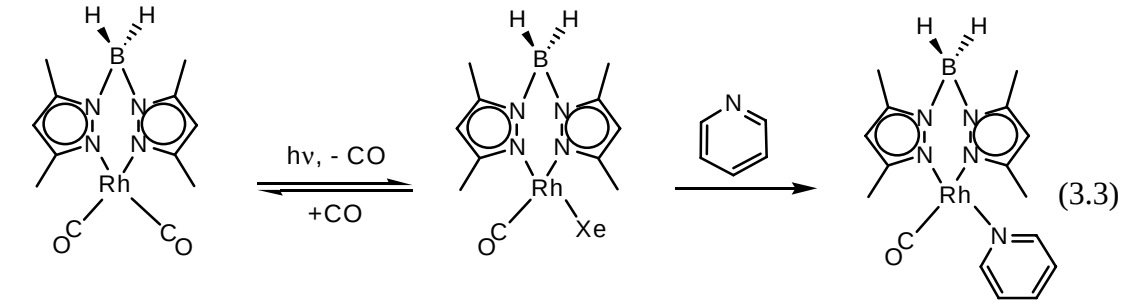

9 ν_{CO} = 2015, 2080 cm^{-1} **10•Xe** 1998 cm^{-1} **11** 1978 cm^{-1} (3.3)

Table 3.1. Structural Assignments for Observed CO Bands Upon Photolysis of 5 and 9

Complex	ν_{CO} (cm^{-1})
Tp*Rh(CO)$_2$ (**5**)	1982, 2054
η^3-Tp*Rh(CO)•C_6H_{12} (**6•C_6H_{12}**)	1972[a]
η^2-Tp*Rh(CO)•C_6H_{12} (**7•C_6H_{12}**)	1990 [a]
Tp*Rh(CO)(C_6H_{11})(H) (**8**)	2032
η^3-Tp*Rh(CO)•Xe (**6•Xe**)	1978
η^2-Tp*Rh(CO)•Xe (**7•Xe**)	1996
Bp*Rh(CO)$_2$ (**9**)	2015, 2080
Bp*Rh(CO)•C_6H_{12} (**10•C_6H_{12}**)	1992 [a]
Bp*Rh(CO)•Xe (**10•Xe**)	1998
Bp*Rh(CO)(pyridine) (**11**)	1978

a) Ref. 25: photolysis in cyclohexane

It is important to note that the IR data alone are insufficient to determine the number of Xe atoms discretely coordinated to the complexes. For simplicity we have drawn the structures with a single Xe atom bound. An alternative explanation for the two transient bands arising from photolysis of **5** would be that they both result from a single species, perhaps a dimer formed from reaction of the Rh monocarbonyl photoproduct with the parent complex. Assuming a risetime of 300 ns and a parent concentration of 0.1 mM, the dimerization would require a second-order rate constant of 10^{10} $M^{-1}s^{-1}$ at -50 °C. This rate constant is not unreasonable for a diffusion-controlled reaction in the low-viscosity liquid Xe medium.[37] Nonetheless, the photochemistry of **9** described above strongly bolsters the change-in-hapticity hypothesis.

There is notable similarity between the CO stretching frequencies of the xenon solvates (**6•Xe**, **7•Xe**) and those of the solvates observed in cyclohexane (**6•C_6H_{12}**, **7•C_6H_{12}**) in the Harris study (Scheme 3.1).[8] However, the time evolution of these species differs significantly. In room temperature cyclohexane, the η^3-Tp* complex is converted quantitatively into the η^2-Tp* complex within 200 ps. In Xe at –50 °C, the bidentate and tridentate complexes have comparable stabilities; they decay together on a microsecond timescale. Since the risetime of the transient bands in the present study is detector-limited to 300 ns, it is reasonable to assume that we observe an equilibrated mixture of **6•Xe** and **7•Xe** in the transient IR spectrum. In Xe, as in cyclohexane, photolysis of **5** may initially produce only the η^3-Tp* solvate**,** which then equilibrates with the bidentate isomer on a timescale much shorter than 300 ns. It thus appears that the equilibrium in room temperature cyclohexane favors the bidentate isomer to a much greater extent than does the equilibrium in low temperature Xe. Several factors could account for this observation. In particular, the steric bulk of cyclohexane (relative to Xe) ought to drive the equilibrium toward the bidentate isomer, since detachment of the pyrazolyl group relieves steric congestion at the metal center. Cyclohexane may also serve as a better σ-donor than Xe (consistent with the red-shifts in the CO stretching frequencies of **6•C_6H_{12}** and **7•C_6H_{12}** relative to **6•Xe** and **7•Xe**) and therefore drive the pyrazolyl ligand dissociation. Additionally, the temperature difference between the Xe and cyclohexane studies may be significant.

Upon reaction of **5** with cyclohexane in liquid Xe, the bidentate and tridentate solvates both decay with the same observed rate constant to yield the Rh alkyl hydride **8**. This observation is consistent with a Curtin-Hammett kinetic scheme[38] involving rate-

limiting C-H bond oxidative addition, which permits fast equilibration of the η^2- and η^3-Tp* solvates prior to the rate-determining step. The kinetics are complicated by the fact that, in addition to the hapticity equilibrium, there is presumably an equilibrium between Xe and cyclohexane solvates of the Tp*Rh(CO) fragment. Past studies in our group have identified such equilibria. Moreover, the studies have shown that it is very difficult to spectroscopically distinguish alkane and noble gas solvates in a liquid noble gas; the CO stretches of the two species can differ by less than 1 cm^{-1}.[24] Consequently, it is not straightforward to compare the ratio of bidentate and tridentate isomers in an Xe/cyclohexane mixture to the analogous ratio in cyclohexane solution.

Conclusions

Photolysis of Tp*Rh(CO)$_2$ (**5**) at 308 nm in liquid Xe solution gives rise to two transient IR bands centered at 1978 cm^{-1} and 1996 cm^{-1}. These bands have been assigned to Tp*Rh(CO)•Xe solvates differing in the coordination geometry of the Tp* ligand. Specifically, the 1978 cm^{-1} absorption is assigned to the CO stretch of the tridentate Tp* complex **6•Xe**, while the band at higher frequency is assigned to the bidentate Tp* complex **7•Xe**. These assignments are based in large part on the 1998 cm^{-1} band observed upon photolysis of the bidentate Bp*Rh(CO)$_2$ (**9**) in Xe, and on the 1978 cm^{-1} band observed when **9** is photolyzed in Xe in the presence of pyridine.

The partitioning between Tp* hapticities in the Xe solvates at -50 °C contrasts markedly with the ligand behavior observed in room temperature alkane solvent. Collaboration with the C. B. Harris group showed that the η^3-Tp*Rh(CO)•C_6H_{12} solvate (**6•C_6H_{12}**), produced upon photolysis of **5** in room temperature cyclohexane, undergoes quantitative isomerization to the bidentate isomer **7•C_6H_{12}** in 200 ps.[8] These differences

point to a solvent and temperature dependence in the equilibrium between bidentate and tridentate Tp*Rh(CO) solvates.

Notes and References

1) Ghosh, C. K.; Graham, W. A. G. *J. Am. Chem. Soc.* **1987**, *109*, 4726.

2) For mechanistic studies of C-H activation by a related Tp*Rh complex, see this and the subsequent reference: Wick, D. D.; Reynolds, K. A.; Jones, W. D. *J. Am. Chem. Soc.* **1999**, *121*, 3974.

3) Wick, D. D.; Jones, W. D. *Organometallics* **1999**, *18*, 495.

4) For a study of C-H activation by a Tp*Pt complex, see: Wick, D. D.; Goldberg, K. I. *J. Am. Chem. Soc.* **1997**, *119*, 10235.

5) For a comprehensive survey of the coordination chemistry of pyrazolylborate ligands, see: Trofimenko, S. *Scorpionates: The Coordination Chemistry of Polypyrazolylborate Ligands*; Imperial College: London, 1999 .

6) Purwoko, A. A.; Lees, A. J. *Inorg. Chem.* **1996**, *35*, 675.

7) Purwoko, A. A.; Tibensky, S. D.; Lees, A. J. *Inorg. Chem.* **1996**, *35*, 7049.

8) Bromberg, S. E.; Yang, H.; Asplund, M. C.; Lian, T.; McNamara, B. K.; Kotz, K. T.; Yeston, J. S.; Wilkens, M.; Frei, H.; Bergman, R. G.; Harris, C. B. *Science* **1997**, *278*, 260.

9) Bloyce, P. E.; Mascetti, J.; Rest, A. J. *J. Organomet. Chem.* **1993**, *444*, 223.

10) Sun, X. Z.; Grills, D. C.; Nikiforov, S. M.; Poliakoff, M.; George, M. W. *J. Am. Chem. Soc.* **1997**, *119*, 7521.

11) Sun, X. Z.; George, M. W.; Kazarian, S. G.; Nikiforov, S. M.; Poliakoff, M. *J. Am. Chem. Soc.* **1996**, *118*, 10525 and references therein.

12) Tacke, M.; Oskam, A.; Stufkens, D. J.; Teuben, J. H.; Luinstra, G. A.; deWolf, J. M.; Tacke, C. *J. Mol. Struct.* **1997**, *408*, 499.

13) Upmacis, R. K.; Poliakoff, M.; Turner, J. J. *J. Am. Chem. Soc.* **1986**, *108*, 3645.

14) Maier, W. B.; Poliakoff, M.; Simpson, M. B.; Turner, J. J. *J. Chem. Soc., Chem. Commun.* **1980**, 587.

15) Grills, D. C.; Sun, X. Z.; Childs, G. I.; George, M. W. *J. Phys. Chem. A* **2000**, *104*, 4300.

16) Weiller, B. H. *J. Am. Chem. Soc.* **1992**, *114*, 10910.

17) Wells, J. R.; Weitz, E. *J. Am. Chem. Soc.* **1992**, *114*, 2783.

18) Jyo-O, M.; Takeda, H.; Omiya, K.; Ishikawa, Y.; Arai , S. *Bull. Chem. Soc. Jpn.* **1993**, *66*, 3618.

19) For a theoretical treatment of the bonding in transition metal rare gas complexes, see: Ehlers, A. W.; Frenking, G.; Baerends, E. J. *Organometallics* **1997**, *16*, 4896.

20) Sponsler, M. B.; Weiller, B. H.; Stoutland, P. O.; Bergman, R. G. *J. Am. Chem. Soc.* **1989**, *111*, 6841.

21) Weiller, B. H.; Wasserman, E. P.; Bergman, R. G.; Moore, C. B.; Pimentel, G. C. *J. Am. Chem. Soc.* **1989**, *111*, 8288.

22) Weiller, B. H.; Wasserman, E. P.; Moore, C. B.; Bergman, R. G. *J. Am. Chem. Soc.* **1993**, *115*, 4326.

23) Schultz, R. H.; Bengali, A. A.; Tauber, M. J.; Weiller, B. H.; Wasserman, E. P.; Kyle, K. R.; Moore, C. B.; Bergman, R. G. *J. Am. Chem. Soc.* **1994**, *116*, 7369.

24) Bengali, A. A.; Schultz, R. H.; Moore, C. B.; Bergman, R. G. *J. Am. Chem. Soc.* **1994**, *116*, 9585.

25) Bengali, A. A.; Bergman, R. G.; Moore, C. B. *J. Am. Chem. Soc.* **1995**, *117*, 3879.

26) Bengali, A. A.; Arndtsen, B. A.; Burger, P. M.; Schultz, R. H.; Weiller, B. H.; Kyle, K. R.; Moore, C. B.; Bergman, R. G. *Pure Appl. Chem.* **1995**, *67*, 281.

27) McNamara, B. K.; Yeston, J. S.; Bergman, R. G.; Moore, C. B. *J. Am. Chem. Soc.* **1999**, *121*, 6437.

28) May, S.; Reinsalu, P.; Powell, J. *Inorg. Chem.* **1980**, *19*, 1582.

29) Bonati, F.; Minghetti, G.; Banditelli, G. *J. Organomet. Chem.* **1975**, *87*, 365.

30) Penner, S. S.; Weber, D. *J. Chem. Phys.* **1951**, *19*, 807.

31) Addition of a larger excess of CO could have increased the parent recovery percentage, but the rates of the recovery and transient decays would have become too fast to measure using our detection system.

32) The transient decay at 1996 cm^{-1} appears to be kinetically coupled to formation of a product band at 1984 cm^{-1}, perhaps indicative of dimer formation. This product band is not observed in the presence of buffering CO.

33) Graham and co-workers observed weak bands in IR spectra of **5**, blue-shifted 30 cm^{-1} from the CO stretching bands, which they assigned to the CO stretches of η^2-Tp*Rh$(CO)_2$: Ball, R. G.; Ghosh, C. K.; Hoyano, J. K.; McMaster, A. D.; Graham, W. A. G. *J. Chem. Soc., Chem. Commun.* **1989**, 341.

34) For a recent study of the solution phase equilibrium between η^3- and η^2-Tp coordination in a Rh complex, see: Moszner, M.; Wolowiec, S.; Trösch, A.; Vahrenkamp, H. *J. Organomet. Chem.* **2000**, *595*, 178.

35) Chauby, V.; Leberre, C. S.; Kalck, P.; Daran, J. C.; Commenges, G. *Inorg. Chem.* **1996**, *35*, 6354.

36) Connelly, N. G.; Emslie, D. J. H.; Metz, B.; Orpen, A. G.; Quayle, M. J. *Chem. Commun.* **1996**, 2289.

37) Espenson, J. H. *Chemical Kinetics and Reaction Mechanisms*; 2nd ed.; McGraw-Hill: New York, 1995 pp. 199-203.

38) Seeman, J. I. *Chem. Rev.* **1983**, *83*, 83.

Chapter 4. Preparation and Reactivity of Bp*Rh(CO)(pyridine)

Introduction

The observed stability of Bp*Rh(CO)(pyridine) (**11**) in liquid Xe solution warranted further investigation. Through isolation of this compound, we sought to gain additional insight into the structural factors favoring C-H bond activation at the analogous Tp*Rh(CO) center. Moreover, while the Tp* fragment has become a versatile and well-studied ancillary ligand in organometallic chemistry,[1-3] the bidentate Bp* analog and its variously substituted derivatives have been utilized less often.[4-9] Synthesis of **11** on a preparative scale offered the opportunity to extend current knowledge of the coordination chemistry of the Bp* ligand. In comparison with other bidentate monoanionic ligands, the Bp* fragment is intriguing in light of the proximity to the coordinated metal center of two potentially reactive hydrides and a latent Lewis acidic center at boron. Investigations of the reactivity of the Bp* pyridine adduct **11** are presented below.

Results

Preparation of Bp*Rh(CO)(pyridine) (11). As discussed in the previous chapter, UV photolysis of a liquid xenon solution of **9** and pyridine gives rise to a new IR band at 1978 cm^{-1}, which we assigned to the CO stretch of Bp*Rh(CO)(pyridine) (**11**). FTIR spectra revealed that this new complex is stable in xenon at -50 °C; however, product isolation was not feasible on such small scale. We therefore attempted to synthesize **11** on a larger scale in a more conventional solvent. While displacement of a

CO ligand in **9** by triphenylphosphine is rapid at room temperature, analogous substitution by pyridine does not proceed thermally.[10] Furthermore, large-scale photolysis of **9** in pyridine solution results in no net reaction, due to the efficiency of CO recombination. To inhibit recombination, an active nitrogen purge was employed during photolysis, but yields in this case were irreproducible because of their acute dependence on the purge rate. Moreover, the dark brown crude product was contaminated with side-products, which could be removed only through an inefficient sublimation procedure.

As an alternate means of effecting the reaction with pyridine, we elected to activate **9** with trimethylamine-N-oxide, which has been shown in many cases to labilize CO ligands by oxidation to CO_2.[11] Treatment of a yellow pyridine solution of dicarbonyl **9** with stoichiometric trimethylamine-N-oxide results in a color change to bright orange. The reaction proceeds over the course of one hour at room temperature, and it leads to yellow-orange Bp*Rh(CO)(pyridine) (**11**) in 77 % yield after crystallization from a toluene/pentane mixture (eq 4.1). In alkane solvent, the CO stretching frequency of **11** shifts to 1972 cm^{-1}. The ^1H NMR spectrum of **11** in benzene solution is characterized by four methyl singlets at 1.50, 2.33, 2.35, and 2.53 ppm, two methyne singlets at 5.50 and 5.66 ppm, and three pyridine resonances at 6.03, 6.50 and 8.45 ppm. The inequivalence of the four pyrazolyl methyl groups and two methyne protons is indicative of a square planar geometry at the metal center.

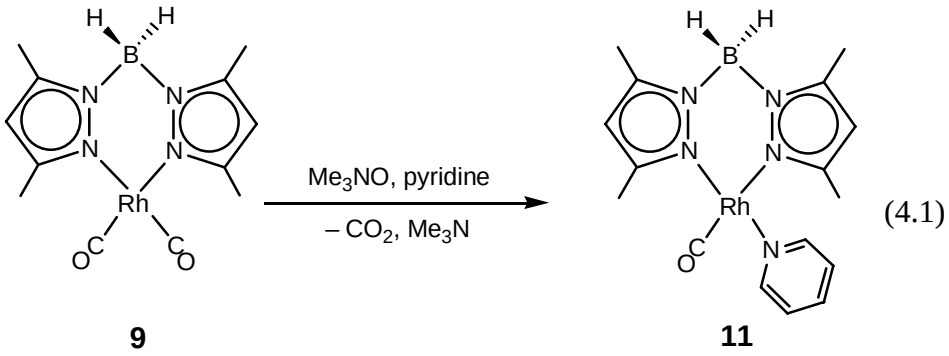

9 **11** (4.1)

We were somewhat surprised to find that pyridine-N-oxide does not effect oxidative decarbonylation of **9**, even at 75 °C. Preparation of **11** with Me_3NO was carried out at N-oxide concentrations on the order of 70 mM; O atom transfer from Me_3NO to **11** must therefore proceed at least 100 times faster than competing pyridine oxidation to pyridine-N-oxide. Treatment of dicarbonyl **9** with Me_3NO in less coordinating solvents (benzene, THF, dichloromethane) resulted in decomposition of the Rh complex as judged by ^1H NMR spectroscopy. Trimethylamine is evidently ineffective as a trap for the Bp*Rh(CO) fragment.

Reactivity of 11 with nucleophiles. Treatment of a solution of **11** (25 mM) with CO (1 atm) at room temperature results in immediate and quantitative formation of dicarbonyl **9** with concomitant liberation of pyridine. Addition of a hundredfold excess of pyridine-d_5 in place of CO leads equally rapidly and efficiently to the pyridine-d_5 analog of **11**. The pyridine ligand in **11** was also displaced by trimethylphosphine and by *p*-dimethylaminopyridine (DMAP).

Treatment of 11 with nonpolar electrophiles. As previously noted, the CO stretching frequency of **11** is the same as that observed for the closely related transient η^3-Tp*Rh(CO) alkane adduct (**6**), which Bromberg *et al.* identified spectroscopically along

the pathway for photoinduced C-H bond activation by Tp*Rh(CO)$_2$ (**5**) (Ch. 3, Scheme 3.1).[12] This similarity suggests a comparable electronic environment at the Rh center in the two species. We therefore anticipated that **11** might prove reactive toward C-H bonds. However, no such reactivity was observed. At room temperature, **11** is stable in alkane or benzene solution; at 75 °C in benzene, **11** decomposes over the course of a day, yet none of the decomposition products show clear evidence of C-H activation. Furthermore, **11** (30 mM in benzene) shows no signs of irreversible reaction at 45 °C upon addition of aldehydes (1 equiv: acetaldehyde, tolualdehyde),[13] hydrogen (1 atm), or tertiary silanes (1 equiv: triethylsilane, triphenylsilane).

Whereas the chelating Tp* ligand enforces a tetrahedral geometry at the metal center in **6**, the free pyridine ligand in **11** permits a square planar arrangement of the three nitrogen donors. It seemed therefore that **11** could simply be trapped in a coordination geometry too stable for reaction with nonpolar electrophiles. To test this hypothesis, we attempted to introduce the pyridine ligand farther along the reaction coordinate for C-H activation. As discussed in the previous chapter, the C-H bond-breaking event in reaction of the Tp* complex **5** with alkanes occurs from an intermediate with η^2-Tp* coordination. In the alkyl hydride product, however, the third pyrazolyl nitrogen recoordinates to the metal center (Ch. 3, Scheme 3.1). Bp*Rh(CO)$_2$ (**9**) was therefore photolyzed in benzene/pyridine mixtures in the hope that the pyridine would trap a transient Bp*Rh(CO)(Ph)(H) species, thus mimicking the recoordination step in reaction of the Tp* complex.[14] However, these experiments led only to isolation of the pyridine adduct **11** and to decomposition products upon extended photolysis.

As a final probe of the striking reactivity difference between **6** and **11**, we attempted to prepare an alkyl hydride complex from **11** indirectly by addition of iodomethane, to be followed by reduction of the iodide ligand with a hydride source (eq 4.2). These efforts were sidetracked, however, by observation of the unexpected complex reaction described below.

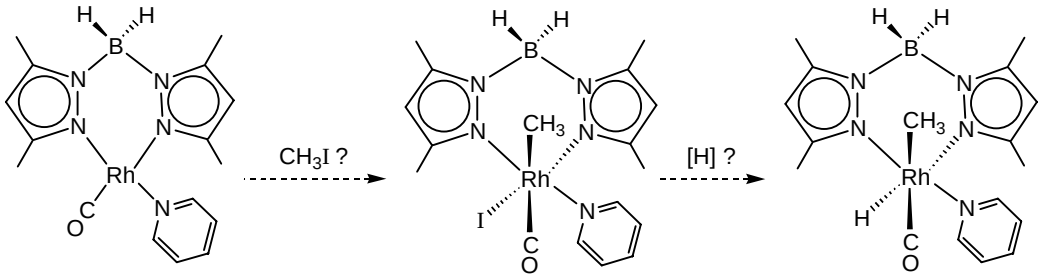

(4.2)

Reactivity of 11 with iodomethane. Treatment of a benzene solution of pyridine complex **11** with iodomethane (25 mM of each reagent) results in immediate reaction at room temperature to form a new product quantitatively, as judged by ^{1}H NMR. The ^{1}H NMR spectrum of this species exhibits five methyl singlets in the 1-3 ppm region, two methyne singlets at 5.48 and 5.70, two pyridine resonances at 6.14 and 6.61, and a doublet at –14.2 ppm characteristic of a hydride bound to Rh. The IR spectrum exhibits a Rh-H stretch at 2060 cm^{-1}. Because we were unable to come to a definitive decision about the structure on the basis of the spectroscopic data, an X-ray diffraction analysis was carried out on crystals obtained from a THF/pentane solution. The product was shown to have the structure **12**, as illustrated in eq 4.3 and Figure 4.1.[19]

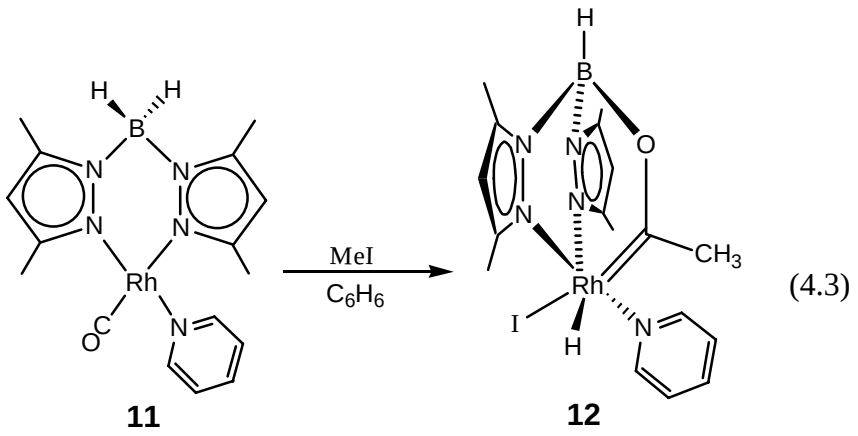

11 **12** (4.3)

Formation of **12** thus involves a surprisingly deep-seated series of overall bonding changes: (i) addition of the C-I bond across the M-C bond of a CO ligand to give an acyl or oxycarbene functionality, which is presumably stabilized by coordination of its oxygen atom to the Bp* boron atom, and (ii) transfer of a hydrogen from the boron center to rhodium. The analogous reaction is observed upon mixing of iodomethane and Bp*Rh(CO)(DMAP); however, neither the dicarbonyl complex **9** nor the phosphine carbonyl complex Bp*Rh(CO)PPh_3 reacts with iodomethane, even after prolonged heating of benzene solutions at 75 °C. The Rh=C–O moiety in **12** bears significant Fischer carbene character, as evidenced by the 300 ppm downfield chemical shift for this carbon in the $^{13}C\{^1H\}$ NMR spectrum ($J_{Rh\text{-}C}$ = 35 Hz),[15] and by its relatively short Rh-C bond length (1.91 Å). For comparison, typical Rh-C single bond lengths in Rh(III) acyl functionalities range from 1.93 to 2.06 Å.[16-18]

Further transformation of **12** yielded a second unexpected result. Thermolysis of the carbene complex in benzene or THF at 45 °C for 36 h leads to formation of a new product in 71 % yield based on internal standard. Crystals of this product, obtained in 60 % yield by vapor diffusion of pentane into a toluene solution at –35 °C, were analyzed

by X-ray diffraction and shown to have the structure **13**, illustrated in eq 4.4 and Figure 4.2.

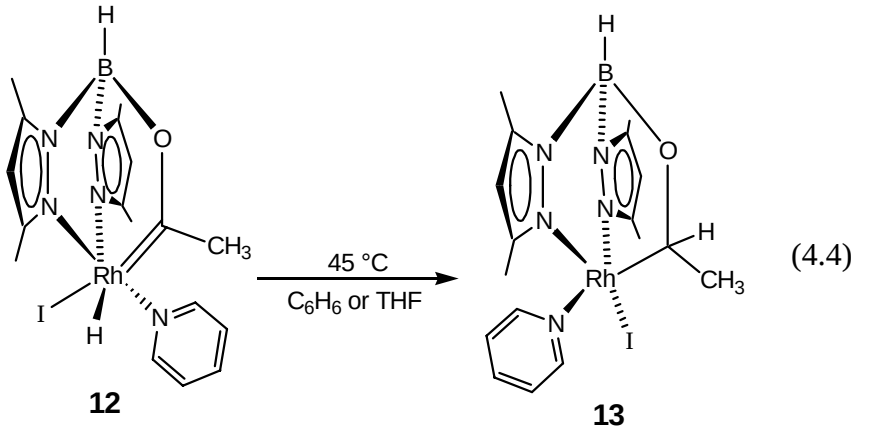

(4.4)

Formation of **13** from **12** thus entails migration of the hydride ligand from the metal center to the carbene carbon (the α-carbon bound to oxygen), leading to a coordinatively unsaturated Rh bearing a boron-stabilized 1-alkoxyethyl group. In the $^{13}C\{^{1}H\}$ NMR spectrum of **13**, the α-carbon resonance appears as a doublet at 89 ppm (J_{Rh-H} = 20 Hz). The proton bound to this carbon exhibits a surprisingly downfield resonance (7.97 ppm); coupling of this resonance to the three equivalent methyl protons (J = 4 Hz) and to Rh (J_{Rh-H}=5 Hz; resolved by presaturation of the methyl resonance) produces an overlapped doublet of quartets, which appears as a quintet. As illustrated in Figure 4.2, complex **13** exhibits a square pyramidal geometry about the 5-coordinate Rh center (the sum of the angles formed by I, the pyridine nitrogen, and the pyrazolyl nitrogens with Rh at the vertex is 359.7°). Conversion of **12** to **13** results in a lengthening of the Rh-C and C-O bonds and concomitant shortening of the O-B bond (Table 4.1).

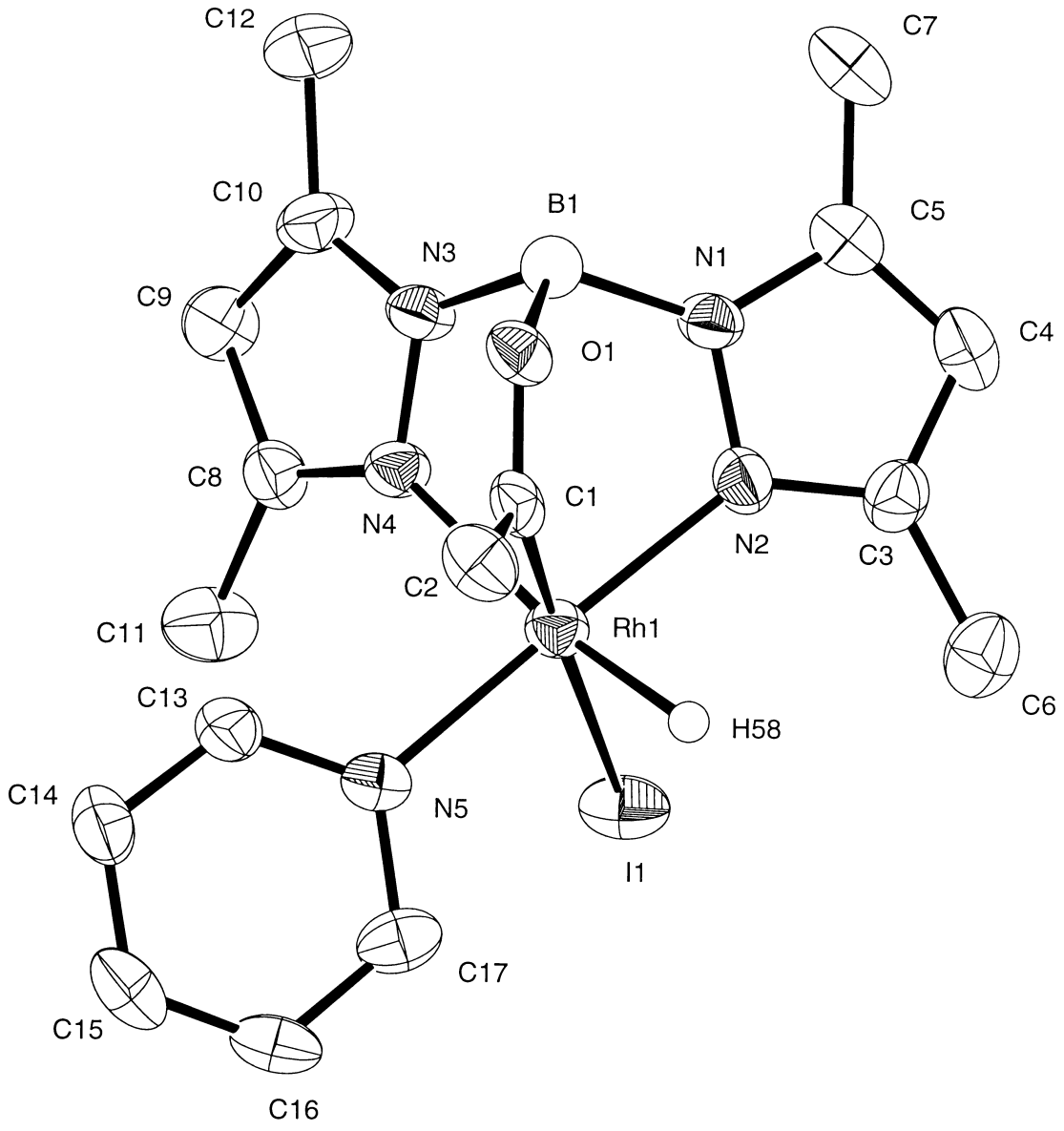

Figure 4.1. ORTEP diagram of **12**. Thermal ellipsoids are shown at 50 % probability.

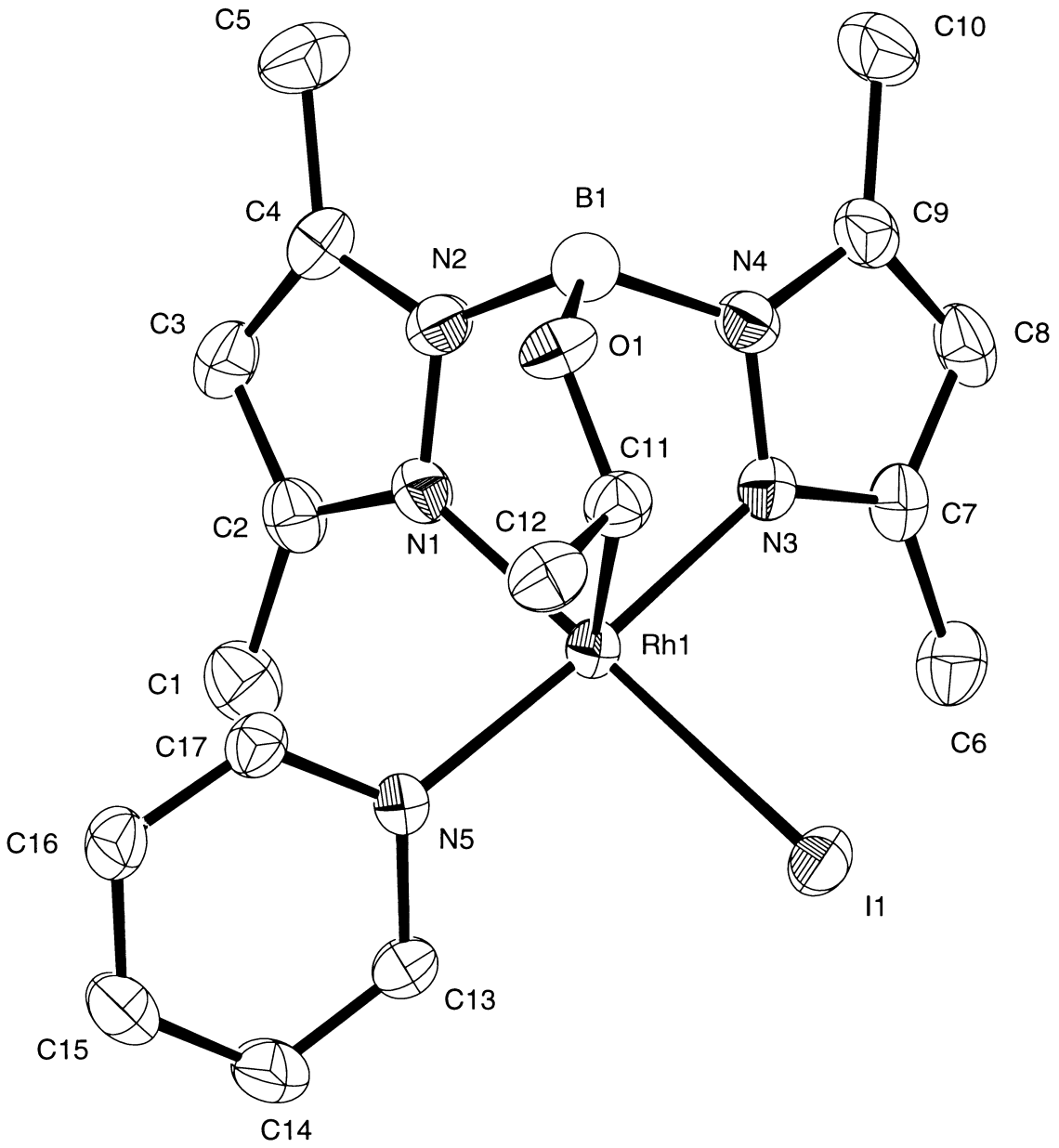

Figure 4.2. ORTEP diagram of **13**. Thermal ellipsoids are shown at 50 % probability.

Table 4.1. Selected Bond Lengths in the Solid State Structures of **12**[a] and **13** (Å)

Bond	**12**	**13**
Rh-C	1.91	2.11
C-O	1.28	1.36
O-B	1.55	1.45
Rh-I	2.81	2.66
Rh-H	1.56	NA

a) Ref. 19

The solid state structures in Figures 4.1 and 4.2 reveal significant steric interaction between the pyridine ligand and one of the pyrazolyl methyl groups. Consistent with this observation, variable temperature ^{1}H NMR studies of **12** and **13** support hindered rotation of the pyridine ligand about the Rh-N bond in solution. In ^{1}H NMR spectra of THF solutions of the complexes at room temperature, the pyridine ortho proton resonances are broadened into the baseline, while the meta protons exhibit one sharp triplet resonance. Spectra of **12** and **13** acquired at –60 °C display five sharp resonances in the 7-10 ppm region, corresponding to five distinct pyridine protons. The ortho proton resonances appear as doublets at 7.5 ppm and 10.1 ppm for **12** and 8.3 ppm and 10.0 ppm for **13**. These characteristics find precedent in the spectra of Tp*Ti(N^{t}Bu)Cl[4-(^{t}Bu)py], prepared by Mountford and co-workers; the large frequency separation between ortho proton resonances is attributed in that study to anisotropic shielding effects from the pyrazole rings.[20] The free energy barriers to rotation about the Rh-py bonds in **12** and **13** were estimated at the coalescence temperatures of the meta

proton resonances, using the relation $k_{rot} = (\delta\nu) \times (\pi / \sqrt{2})$, where $\delta\nu$ is the peak separation in Hz at the slow exchange limit.[21] For **12**, coalescence occurs at –17.5 (±1) °C, corresponding to a barrier at that temperature of 12.1 (±0.5) kcal/mol. For **13**, coalescence occurs at –7.5 (±1) °C, corresponding to a barrier at that temperature of 12.7 (±0.5) kcal/mol. These barriers compare very well with the 12.2 kcal/mol barrier reported for the Ti complex at –6 °C.[20]

Labeling studies of the mechanism for formation of 12 and 13. In order to distinguish intermolecular and intramolecular hydride transfer pathways in the conversions of **11** to **12** and **12** to **13**, we performed a crossover experiment employing unlabeled **11** and doubly labeled d_2-B[$(CH_3)_2$pz]Rh(^{13}CO)(py). In a reaction mixture of these two complexes and iodomethane, an intermolecular hydride migration would lead to a statistical mixture of H and D bound to ^{12}C and ^{13}C in the final product **13**, while an intramolecular mechanism would yield only ^{12}C–H and ^{13}C-D products (Scheme 4.1).

Scheme 4.1

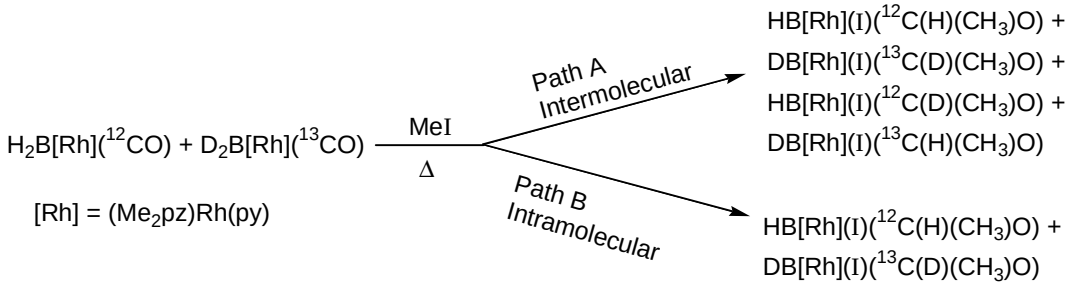

A slight complication arose because the deuterated Bp* ligand, prepared from dimethylpyrazole and $NaBD_4$,[22] could not be isolated without significant hydride incorporation at the boron (possibly from the glassware surface), despite prior deuteration of the pyrazole nitrogen and attempts to deuterate the glassware. This exchange process

was no longer active once the ligand was bound to Rh: IR analysis of doubly labeled **11** revealed > 93 % ^{13}C incorporation and 60 % deuterium incorporation at boron. Equimolar amounts of this complex and unlabeled **11** were dissolved together in benzene-d_6 and treated with iodomethane, after which the solution was thermolyzed at 45 °C for 36 h to form **13**.[23]

Analysis of the product mixture by ^1H and ^2H NMR spectroscopy supported a strictly intramolecular mechanism for both hydride migrations (B to Rh and Rh to C). The ^1H spectrum of the thermolyzed solution exhibited one resonance at 7.97 ppm with an integral of 0.5, corresponding to the proton bound to the unlabeled α-carbon; additionally, two ^{13}C-coupled satellites of this resonance ($J_{C\text{-}H}$ = 170 Hz) were integrated together to 0.2, consistent with the initial 40 % H incorporation at B in the ^{13}C-labelled starting material. In the ^2H spectrum, only a ^{13}C-coupled doublet was evident for the deuterium bound to the α-carbon, indicating that no intermolecular transfer had proceeded to place deuterium on a ^{12}C (Figure 4.3).

Figure 4.3 (overleaf). Excerpts from the ^1H (top) and ^2H (bottom) spectra of the isotopomers of **13** formed from a 1:1 mixture of unlabeled and doubly isotopically labeled precursors. Coupling to Rh and to the methyl protons is broadened out in the ^2H spectrum. The ^2H spectrum shows only a ^{13}C-coupled doublet.

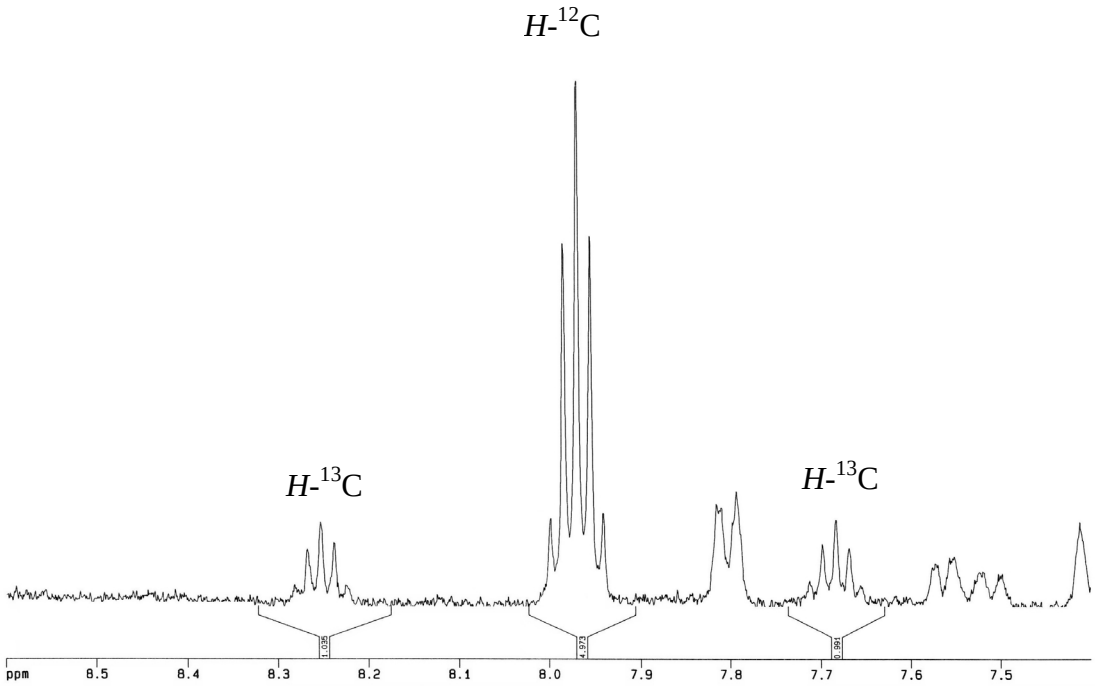
H-12C
H-13C
H-13C
ppm
8.5
8.4
8.3
8.2
8.1
8.0
7.9
7.8
7.7
7.6
7.5

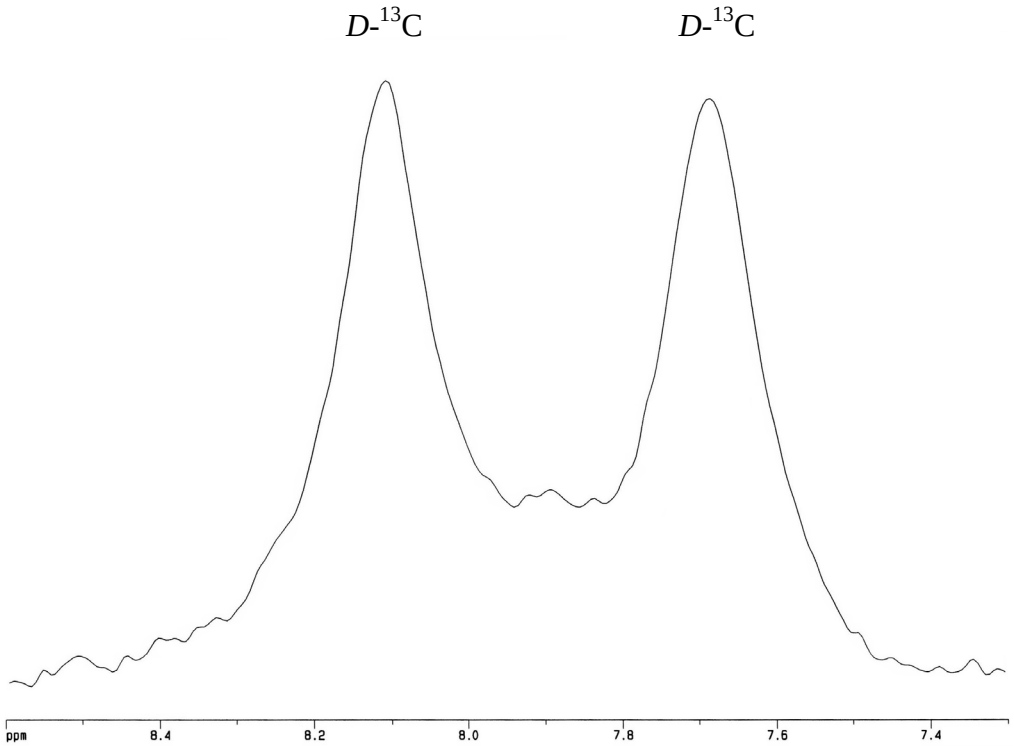
D-13C
D-13C
ppm
8.4
8.2
8.0
7.8
7.6
7.4

Discussion

Inertness of 11 toward C-H activation. As addressed above, we suspect that the reactivity differences between **11** and the isoelectronic Tp*Rh(CO) fragment **6** may in large part be due to the different coordination geometries of the two species. Ligand field arguments favor the square planar geometry in compounds with a d_8 electronic configuration, consistent with a lower energy, and therefore less reactive, HOMO electron pair in **11**.[24] Analogous Group 9 square planar complexes such as Vaska's complex and Wilkinson's catalyst are similarly inert toward aliphatic hydrocarbons.[25] It seems, furthermore, that **11** lies in a sufficiently deep thermodynamic well to preclude pyridine trapping of a transient Bp*Rh(CO)(R)(H) species. This argument is summarized pictorially in the qualitative reaction coordinate diagrams shown in Figure 4.4. It remains unclear whether failure to obtain the pyridine-trapped alkyl hydride **14** is a result of kinetic or thermodynamic constraints. The relative free energies of **11** and **14** were meant to be assessed through independent synthesis of **14**; however, this synthesis was precluded by the unexpected observation of B-H migration in the reaction of **11** with iodomethane.

Figure 4.4 (overleaf). Qualitative free energy diagrams for C-H bond activation at the Tp*Rh(CO) center (top) and pyridine trapping *vs.* C-H activation at the Bp*Rh(CO) center (bottom).

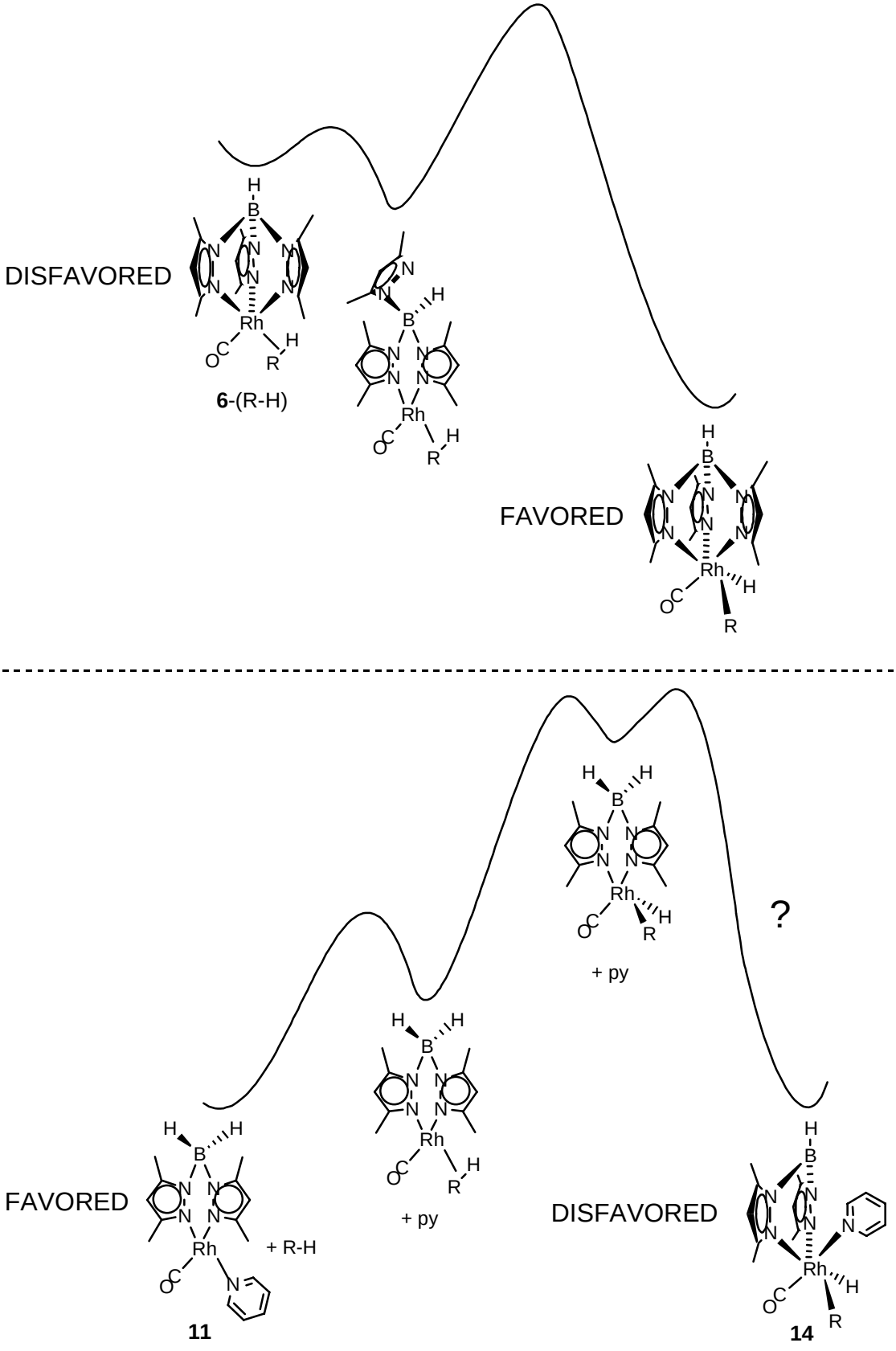
DISFAVORED
6-(R-H)
FAVORED
FAVORED
+ R-H
11
+ py
+ py
?
DISFAVORED
14

Reaction of 11 with Iodomethane. In contrast to C-H bond activation, oxidative addition of polar electrophiles such as iodomethane is a common reaction for d_8 square planar complexes.[25,26] We believe that formation of **12** from **11** proceeds by initial oxidative addition of iodomethane across the Rh center, followed by migratory insertion of the methyl group to form a Rh-acetyl species. As noted above, the reaction proceeds with the pyridine adduct **11** and with the DMAP adduct, though not with dicarbonyl **9** or the triphenylphosphine carbonyl. A ligand field argument may be invoked to rationalize these observations. Specifically, the pyridine ligands can act as weak π-donors and thus enhance the nucleophilicity of the Rh center through electron-electron repulsion; the CO and, to a lesser extent, PPh_3 ligands are π-accepting and thus suppress nucleophilicity.[11] Steric encumbrance could also inhibit the reactivity of the phosphine complex.

The boron hydride transfer step remains intriguing. While most applications of the Bp* ligand have relied on the innocence of the BH_2 moiety, several instances of B-H reactivity have been described.[27-31] A number Bp-substituted transition metal complexes show evidence of an agostic interaction between the boron-bound hydride and the metal center;[32-34] the precedent for such interactions supports a low energy transition state geometry for hydride migration in formation of **12**. It is nonetheless unclear whether hydride transfer precedes or follows the methyl migration (Scheme 4.2).[35] Shriver and co-workers have demonstrated the marked acceleration of migratory insertions upon coordination of Lewis acids to metal-bound CO ligands.[36,37] If hydride

Scheme 4.2

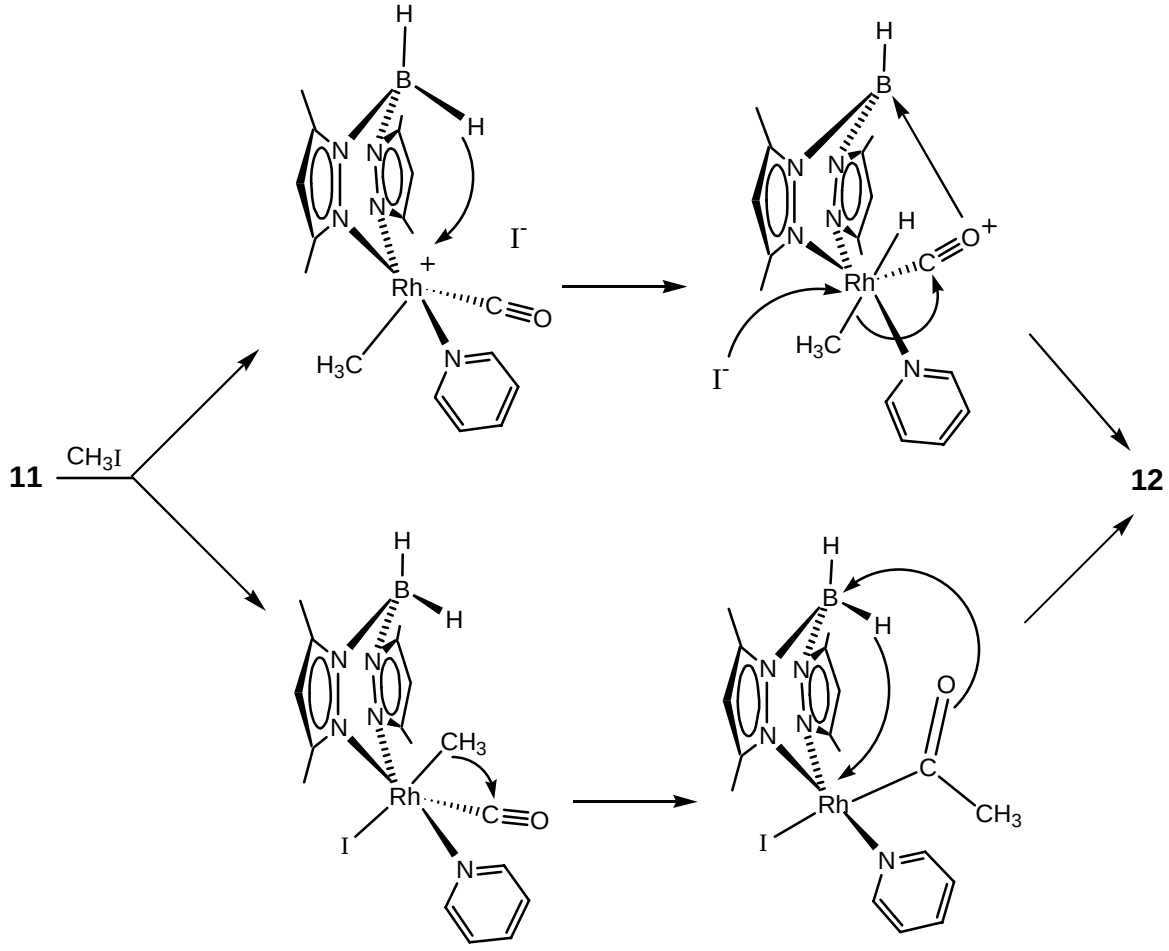

transfer precedes methyl migration (upper pathway above), the boron could serve effectively as a tethered Lewis acid to accelerate the migratory insertion.

To our knowledge, the closest reported structural analogs to the Rh Fischer carbene functionality in **12** are the Rh-Sc heterobimetallic complex **15** and the Rh-Zr_2 trimetallic species **16** (Chart 4.1), neither of which have an acyl oxygen atom coordinated to boron. Complex **15**, prepared by Bercaw and co-workers, was not structurally

characterized but exhibits a carbene-like resonance in its $^{13}C\{^{1}H\}$ NMR spectrum at 279 ppm (d, J_{Rh-C} = 56 Hz).[38] Erker and co-workers structurally characterized complex **16**, which also exhibits a doublet at 279 ppm (J_{Rh-C} = 56 Hz) in the $^{13}C\{^{1}H\}$ NMR spectrum.[39] The bond length reported for the Rh-C double bond in **16** (1.93 Å) compares well with that in **12**.

Chart 4.1

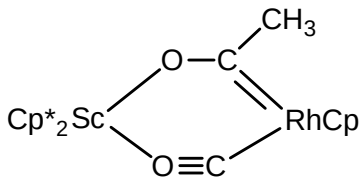

15

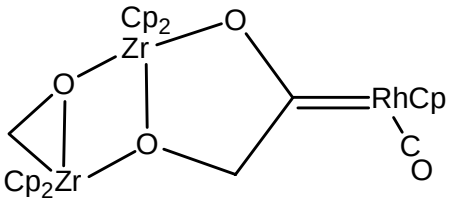

16

Formation of 13. The conversion of **12** to **13** is a rare instance of reverse α-hydride migration. There have been very few direct observations of 1,2-migration from a metal center to a carbene carbon, despite the fact that migration in the opposite direction to form the carbene is common.[25,40-42] In the present case, it is particularly notable that the hydride transfer to carbon is irreversible, despite its resulting in a coordinatively and electronically unsaturated metal center. Once again, coordination of the oxygen to the Lewis acidic boron may help to drive the migration. The overall transformation from **11** to **13** is not unprecedented; Carmona and co-workers showed that thermolysis of $Bp^*Mo(PMe_3)(CO)_2(C(O)Me)$ at 70 °C results in hydride migration from the boron to the acyl carbon (eq 4.5).[30] In this case the Mo center remains coordinatively saturated

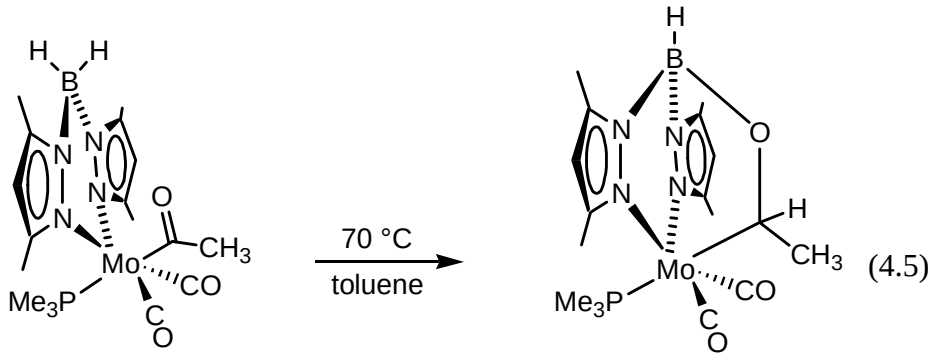

(4.5)

throughout. It is nonetheless possible that the reaction proceeds analogously through a 7-coordinate Mo hydride intermediate, although such a mechanism was not addressed by the authors of that study.

Conclusions

We have prepared the complex Bp*Rh(CO)(pyridine) (**11**) and shown that its reactivity differs profoundly from that of the structurally and electronically similar Tp*Rh(CO) fragment, possibly as a consequence of differing coordination geometries at the Rh center. While **11** does not undergo C-H bond activation, it reacts rapidly with iodomethane via overall addition of CH_3I across the Rh-C bond of the carbonyl ligand. At the same time, the borate functionality in the Bp* ligand participates in the chemistry through hydride transfer from B to Rh and formation of an O-B bond to yield the Fischer carbene-like species **12**. Upon thermolysis of **12**, a reverse α-hydride migration affords the 5-coordinate Rh alkoxyethyl complex **13**. A crossover study supports intramolecular mechanisms for both hydride transfer steps in this unusual reaction sequence.

Experimental Methods

General Procedures. Unless otherwise noted, reactions were performed under dry N_2, either in a glovebox or through the use of standard Schlenk and high vacuum line techniques. Preparative photolyses were carried out using a 450 W medium pressure Hanovia mercury vapor lamp enclosed in a water-cooled, double-jacketed quartz well. Reaction mixtures were maintained at 5-10 °C during photolysis by immersion of the flask and lamp apparatus in an ethylene glycol-filled Endocal refrigerated circulating bath. All NMR spectra were obtained using Bruker AMX-300, AM-400 or DRX-500 MHz spectrometers. Proton, $^{2}H\{^{1}H\}$, and $^{13}C\{^{1}H\}$ chemical shifts (δ) are reported in parts per million (ppm) downfield from tetramethylsilane and were assigned based on internal solvent resonances. ^{11}B NMR spectra were obtained without ^{1}H decoupling, and chemical shifts are reported in ppm downfield from an external $BF_3 \bullet Et_2O$ reference solution. Except where noted, all NMR spectra were acquired at room temperature. Infrared (IR) spectra were recorded using a Mattson Galaxy 3000 spectrometer at 4 cm^{-1} resolution; samples for IR spectroscopy were either mixed with KBr and pressed into pellets or dissolved in an appropriate solvent and added to a standard solution cell with CaF_2 windows and a 750 μm pathlength. Mass spectrometric (MS) analyses were obtained at the U. C. Berkeley Mass Spectrometry Facility. Elemental analyses were performed at the U. C. Berkeley Microanalytical Facility on a Perkin Elmer 2400 Series II CHNO/S Analyzer. X-ray structural data were acquired and analyzed at the U. C. Berkeley CHEXRAY Facility by Dr. Fred Hollander and Dr. Dana Caulder.

Unless otherwise noted, reagents were purchased from commercial suppliers and used without further purification. Potassium bromide (Aldrich) and Celite (Aldrich) were dried *in vacuo* at 250 °C for 48 h. All solvents were purified prior to use. Diethyl ether and tetrahydrofuran (Fisher) were distilled under N_2 from purple sodium/benzophenone ketyl. Pyridine (Mallinckrodt) was distilled under N_2 twice successively, first from CaH_2 and then from sodium. Pentane, hexanes, benzene and toluene (Fisher) were either distilled under N_2 from purple sodium/benzophenone ketyl (no benzophenone was used for toluene), or passed through a column of activated alumina (type A2, size 12 x 32, Purifry Co.) under nitrogen pressure and sparged with N_2. Cyclohexane (Aldrich) and all deuterated solvents (Cambridge Isotope Laboratories) were purified by vacuum-transfer from CaH_2 and stored under N_2. Iodomethane was stored in the dark over copper filings to inhibit radical-induced decomposition and was purified by vacuum transfer immediately prior to use. DMAP (*para*-dimethylaminopyridine) was purified by recrystallization from toluene.

Preparation of compounds.

[Dihydridobis(3,5-dimethylpyrazolyl)borato]dicarbonylrhodium (Bp*Rh(CO)$_2$, 9). Initially, this complex was prepared in accordance with the literature procedure.[10] To a stirred suspension of 510 mg (2.10 mmol) of Bp*K[22] in 50 mL of diethyl ether was added a solution of 400 mg (1.00 mmol) of $[RhCl(CO)_2]_2$ in 12 mL of diethyl ether. The brown reaction mixture was stirred for 1 h and then filtered through a pad of Celite on a fritted funnel. Ether was removed from the filtrate *in vacuo*, and the brownish-yellow residue sublimed at 100 °C (30 mTorr) to give 262 mg (0.724 mmol, 36%) of **9** as a yellow solid. ^{1}H NMR (C_6D_6, 300 MHz) δ 2.08 (s, 3H), 2.13 (s, 3H), 5.46

(s, 1H) ppm. ^{13}C {^{1}H} NMR (C_6D_6, 100 MHz) δ 12.01 (pz*C*H$_3$), 14.03 (pz*C*H$_3$), 105.47 (pz*C*H), 144.75 (pz*C*$_q$), 148.64 (pz*C*$_q$), 185.37 (*C*O, d, $^{1}J_{Rh-C}$ = 66 Hz) ppm. ^{11}B NMR (C_6D_6, 160 MHz) δ -10.4 ppm. IR (KBr) 2966 (m), 2925 (m), 2460 (s, B-H), 2270 (w), 2220 (w), 2080 (vs, CO), 2010 (vs, CO), 1540 (s), 1455 (m), 1420 (m), 1388 (m), 1170 (s), 1110 (s), 1073 (w), 890 (m), 800 (m), 775 (m), 630 (m), 530 (m) cm^{-1}. IR (*n*-pentane) 2080, 2015 cm^{-1} (lit. (pet. ether) 2081, 2015 cm^{-1}).

Side-reaction in the preparation of 9. We found that the above synthesis often resulted in contamination of the desired product with varying amounts of a new species, very similar physically and spectroscopically to **9**. The complexes co-sublime; both are yellow solids at room temperature and exhibit identical CO stretching frequencies in the IR, although the B-H stretching frequency of the new complex is blue-shifted by 100 cm^{-1}. The ^{1}H and ^{13}C NMR spectra of the two compounds are essentially identical in structure, with the resonances of the undesired product offset from the corresponding resonances of **9** by approximately 0.1 ppm in the proton spectrum and 1 ppm in the carbon spectrum. The new species proved to be slightly less soluble in pentane than **9**; thus several recrystallizations afforded sufficiently pure material for mass spectral analysis, which suggested a structure in which one hydrogen in **9** was replaced by a chlorine. In support of this assignment, the ^{11}B NMR spectrum of the compound exhibits a well-resolved doublet, consistent with a single hydrogen bound to boron. Full spectral data are as follows: ^{1}H NMR (C_6D_6, 300 MHz) δ 2.05 (s, 3H), 2.07 (s, 3H), 5.39 (s, 1H) ppm. ^{13}C {^{1}H} NMR (C_6D_6, 125 MHz) δ 13.02 (pz*C*H$_3$), 15.73 (pz*C*H$_3$), 107.08 (pz*C*H), 146.48 (pz*C*$_q$), 151.45 (pz*C*$_q$), 186.13 (*C*O, d, $^{1}J_{Rh-C}$ = 68 Hz) ppm. ^{11}B NMR (C_6D_6, 160 MHz) δ -6.0 (d, J_{B-H}=118 Hz) ppm. IR (KBr): 2980 (m), 2925 (m), 2530 (s, B-H), 2080

(vs, CO), 2010 (vs, CO), 1545 (s), 1450 (m), 1420 (m), 1380 (m), 1200 (s), 1140 (m), 1075 (m), 1033 (m), 835 (m), 820 (m), 775 (m), 690 (m), 625 (s), 530 (m) cm^{-1}. EI MS: *m/z* 396 ($[ClHB(Me_2pz)_2Rh(CO)_2]^+$).

Taken together, these data seemed most consistent with the structure shown below, in which a chlorine has replaced one of the boron hydrides in the Bp* ligand.

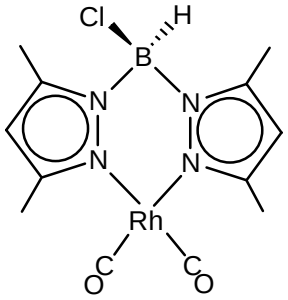

We postulated that this side reaction was due to HCl formed from $[Rh(CO)_2Cl]_2$ and adventitious water. In support of this hypothesis, addition of approximately 0.2 M of triethylamine to the reaction mixture fully suppressed formation of the side-product with no adverse effects toward formation of **9**. The amine appeared to suppress other side reactions as well. The literature preparation required sublimation within several hours of crude product isolation to avoid decomposition; in contrast, reaction mixtures with added amine could simply be filtered and stripped of solvent to afford pure **9** in greatly improved yield (70 %).

Bp*Rh(CO)(pyridine) (11). Photolytic Method: A Pyrex Schlenk flask ($\lambda >$ 300 nm transmission) was charged with a solution of 45.5 mg (0.126 mmol) of **9** in 10 mL of pyridine and capped with a Teflon stopper bored through the center so a glass pipet could be extended into the solution. The reaction mixture was irradiated for 6 h,

during which time a vigorous stream of N_2 was sent through the pipet into the solution and out through the flask sidearm to a mineral oil bubbler. Removal of the pyridine *in vacuo* yielded 51.5 mg of dark brown crude product consisting mainly of **11** as judged by ^{1}H NMR spectra. However, recrystallization attempts in a variety of solvents were unsuccessful, and purification by sublimation (110 °C, 10 mTorr) yielded only 4 mg (0.01 mmol, 8 %) of pure **11** as a yellow solid.

Oxidative Method: A solution of 34.0 mg (0.448 mmol) of Me_3NO in 6 mL of pyridine was added all at once to a solution of 162 mg (0.448 mmol) of **9** in 6 mL of pyridine in a Schlenk flask. The orange reaction mixture was stirred for 1 h, after which the pyridine was removed *in vacuo* to give a brownish-orange residue. The residue was dissolved in toluene and the solution filtered and layered with pentane. Crystallization at –35 °C afforded 143 mg (0.346 mmol, 77 %) of **1** as an orange-yellow solid. ^{1}H NMR (C_6D_6, 400 MHz) δ 1.50 (s, 3H), 2.33 (s, 3H), 2.35 (s, 3H), 2.53 (s, 3H), 5.50 (s, 1H), 5.66 (s, 1H), 6.03 (t, *J*=7.0 Hz, 2H), 6.50 (t, *J*=7.6 Hz, 1H), 8.45 (d, *J*=6.4 Hz, 2H) ppm. ^{13}C {^{1}H} NMR (C_6D_6, 125 MHz) δ 13.1 (pz*C*H$_3$), 13.2 (pz*C*H$_3$), 13.7 (pz*C*H$_3$), 15.9 (pz*C*H$_3$), 105.8 (pz*C*H), 106.1 (pz*C*H), 124.8 (*m*-N*C*$_5$H$_5$), 136.2(*p*-N*C*$_5$H$_5$), 144.2 (pz*C*$_q$), 145.2 (pz*C*$_q$), 148.4 (pz*C*$_q$), 150.2 (pz*C*$_q$), 155.2 (*o*-N*C*$_5$H$_5$), 191.6 (*C*O, d, J_{Rh-H}=76 Hz) ppm. ^{11}B NMR (C_6D_6, 160 MHz) δ -12.07 ppm. IR (KBr) 2954 (m), 2923 (m), 2450 (s, B-H), 1961 (vs, CO), 1536 (s), 1449 (s), 1421 (s), 1383 (m), 1171 (s), 1105 (s), 1060 (w), 890 (w), 783 (m), 753 (w), 693 (m) cm^{-1}. IR (Cyclohexane): 1972 cm^{-1} (CO). Anal. Calc. for $C_{16}H_{21}N_5OBRh$: C 46.52 %, H 5.12 %, N 16.95. Found: C 46.36 %, H 5.43 %, N 16.63 %.

Bp*Rh(CO)(DMAP). A J-Young sealable NMR tube was charged with a solution of 5.9 mg (0.014 mmol) of **11** and 1.8 mg (0.014 mmol) of DMAP in 0.5 mL of C_6D_6. The reaction mixture was heated at 45 °C for approximately 72 h, after which ^{1}H NMR spectra showed a 4:1 ratio of product to **11**. ^{1}H NMR of product (C_6D_6, 400 MHz) δ 1.80 (s, 3H), 1.90 (s, 6H), 2.38 (s, 3H), 2.39 (s, 3H), 2.60 (s, 3H), 5.45 (d, *J*=7.2 Hz, 2H), 5.57 (s, 1H), 5.69 (s, 1H), 8.23 (d, *J*=5.6 Hz, 2H). IR (KBr) 2925 (m), 2455 (m, B-H), 1952 (vs, CO), 1620 (s), 1537 (s), 1445 (m), 1420 (m), 1385 (m), 1225 (m), 1173 (m), 1105 (m), 1068 (m), 1025 (m), 813 (m) cm^{-1}.

HB(Me$_2$pz)$_2$Rh(H)(I)(C(O)Me)(pyridine) (12). To a solution of 55 mg (0.13 mmol) of **11** in 2 mL of benzene was added 9.0 μl (0.13 mmol) of iodomethane via syringe. After 6 h, the solution was frozen and the benzene lyophilized to afford 69 mg (0.12 mmol, 92 %) of **12** as an orange powder. The complex was recrystallized from THF/pentane at –35 °C prior to analysis and co-crystallized with 1 equivalent of THF. At room temperature, the *ortho* pyridyl proton and carbon resonances are broadened into the baseline. ^{1}H NMR (C_6D_6, 400 MHz) δ -14.2 (d, J_{Rh-H}=20Hz, 1H), 1.81 (s, 3H), 2.14 (s, 3H), 2.24 (s, 3H), 2.37 (s, 3H), 2.85 (s, 3H), 5.49 (s, 1H), 5.71 (s, 1H), 6.18 (br, 2H), 6.67 (t, *J*=8 Hz) ppm. ^{1}H NMR of pyridyl resonances at 23 °C (THF-d_8, 500 MHz) δ 7.29 (t, *J*=6 Hz, 2H), 7.83 (t, *J*=8Hz, 1H) ppm. ^{1}H NMR of pyridyl resonances at -80 °C (THF-d_8, 500 MHz) δ 7.25 (t, *J*=5 Hz, 1H), 7.49 (t, *J*=5 Hz, 1H), 7.55 (d, *J*=5 Hz, 1H), 7.92 (t, *J*= 5 Hz, 1H), 10.08 (d, *J*=5 Hz, 1H) ppm. ^{13}C {^{1}H} NMR (C_6D_6, 100 MHz) δ 12.6 (pz*C*H$_3$), 12.8 (pz*C*H$_3$), 16.5 (pz*C*H$_3$), 20.1 (pz*C*H$_3$), 41.7 (RhC(O)*C*H$_3$, d, J_{Rh-H}=4.3 Hz), 108.2 (pz*C*H), 108.4 (pz*C*H), 124.6 (*m*-N*C*$_5$H$_5$), 137.4 (*p*-N*C*$_5$H$_5$), 145.4

(pzC_q), 146.1 (pzC_q), 152.8 (pzC_q), 154.8 (pzC_q), 299.8 (RhC(O)CH_3, d, J_{Rh-H}=35 Hz) ppm. ^{11}B NMR (C_6D_6, 160 MHz) δ -1.15 ppm. IR (KBr) 2985 (m), 2960 (m), 2930(m), 2535 (s, B-H), 2054 (s, Rh-H), 1547 (s), 1446 (s), 1406 (s), 1212 (s), 1160 (s), 1072 (s), 821 (m), 767 (m), 698 (m) cm^{-1}. Anal. Calc. for $C_{21}H_{32}N_5O_2IBRh$ (**12**•THF): C 40.22 %, H 5.14 %, N 11.17. Found: C 40.56 %, H 5.47 %, N 11.07 %.

HB(Me$_2$pz)$_2$Rh(H)(I)(C(O)Me)(DMAP). A J-Young sealable NMR tube was charged with a solution of 5 mg (0.01 mmol) of a 4:1 mixture of Bp*Rh(CO)(DMAP) and **11** in 0.5 mL of C_6D_6. To this solution was added 1.0 μL (0.016 mmol) of iodomethane via syringe. Characterization of the reaction mixture by ^{1}H NMR spectroscopy showed immediate and clean conversion to the Rh hydride product. At room temperature, the *ortho* DMAP-bound proton resonances appeared to be broadened into the baseline. ^{1}H NMR (C_6D_6, 400 MHz) δ -14.22 (d, J_{Rh-H} =24 Hz, 1H), 1.98 (s, 6H), 2.08 (s, 3H), 2.17 (s, 3H), 2.40 (s, 3H), 2.47 (s,3H), 2.92 (s, 3H), 5.51 (m, pzC*H* overlapped with *m*-(DMAP)*H*, 3H), 5.75 (s, 1H).

HB(Me$_2$pz)$_2$Rh(I)(CH(O)Me)(pyridine) (13). A solution of 40 mg (0.072 mmol) of **12** in 1 mL of THF was heated at 45 °C for 36 h. The solution was then filtered and the THF removed *in vacuo* to give a red solid. The crude product was recrystallized at –35 °C from toluene/pentane to yield 24 mg (0.043 mmol, 60 %) of red crystals. The complex crystallized with 0.5 equivalent of toluene, which was evident in the crystal

structure but removed under vacuum prior to analysis. ^{1}H NMR (C_6D_6, 300 MHz) δ 1.11 (s, 3H), 1.72 (d, *J*=4 Hz, 3H), 2.13 (s, 3H), 2.24 (s, 3H), 2.85 (s, 3H), 5.33 (s, 1H), 5.53 (s, 1H), 6.12 (br, 2H), 6.55 (t, *J*=6 Hz, 1H), 7.97 (dq, J_{Rh-H}=5 Hz, J_{H-H}=4 Hz, 1H) ppm. ^{1}H NMR of pyridyl resonances at 23 °C (THF-d_8, 500 MHz) δ 7.36 (t, *J*=6.5 Hz, 2H), 7.89 (t, *J*=8Hz, 1H) ppm. ^{1}H NMR of pyridyl resonances at -60 °C (THF-d_8, 500 MHz) δ 7.34 (t, *J*=5 Hz, 1H), 7.49 (t, *J*=5 Hz, 1H), 7.96 (d, *J*=5 Hz, 1H), 8.27 (t, *J*= 5 Hz, 1H), 10.01 (d, *J*=5 Hz, 1H) ppm. ^{13}C {^{1}H} NMR (THF-d_8, 125 MHz) δ 12.0 (pz*C*H_3), 12.7 (pz*C*H_3), 12.8 (pz*C*H_3), 18.7 (pz*C*H_3), 30.4 (RhCH(O)*C*H_3), 89.0 (Rh*C*H(O)CH_3, d, J_{Rh-H}=20 Hz) , 107.3 (pz*C*H), 107.7 (pz*C*H), 125.4 (*m*-N*C*$_5H_5$), 138.5 (*p*-N*C*$_5H_5$), 143.8 (pz*C*$_q$), 147.2 (pz*C*$_q$), 149.3 (pz*C*$_q$), 154.3 (pz*C*$_q$) ppm. ^{11}B NMR (THF-d_8, 160 MHz) δ -3.9 (d, J_{B-H}=95 Hz) ppm. IR (KBr) 2962 (m), 2905 (m), 2463 (s, B-H), 1538 (s), 1447 (s), 1416 (s), 1381 (s), 1214 (m), 1166 (s), 1129 (s), 1105 (s), 1065 (s), 975 (m), 843 (w), 799 (m), 761 (w), 701 (m), 634 (w) cm^{-1}. Anal. Calc. for $C_{17}H_{24}N_5OIBRh$: C 36.79 %, H 4.36 %, N 12.62 Found: C 37.21 %, H 4.58 %, N 12.66 %.

X-ray Crystal Structure Determinations of 12 and 13. Data collection and refinement parameters are summarized in Table 4.2. Crystal fragments of each compound were mounted on quartz fibers using Paratone N hydrocarbon oil. All measurements were made on a SMART[43] CCD area detector with graphite monochromated MoKα radiation (λ = 0.71069 Å). Data were integrated by the program SAINT[44], corrected for Lorentz and polarization effects, and analyzed for agreement and possible absorption using XPREP.[45] An empirical absorption correction based on

Table 4.2. Crystal data collection and refinement parameters for complexes **12** and **13**

Parameter	**12**•THF	**13**•(0.5 toluene)
empirical formula	$RhIO_2N_5C_{21}H_{32}B$	$RhN_5C_{20.50}IOH_{28}B$
formula weight	627.14	601.10
crystal habit	pale yellow blocks	orange blocks
crystal size, mm	0.27 x 0.27 x 0.07	0.21 x 0.11 x 0.10
crystal system	orthorhombic	monoclinic
lattice type	primitive	primitive
no. rflns. for unit cell (2θ range, °)	5683 (3.00 – 46.00)	5226 (3.00 – 46.00)
lattice parameters:		
a, Å	19.2442 (7)	9.6225(9)
b, Å	15.9667(5)	19.153(2)
c, Å	16.6559(5)	13.7748(14)
β, °	N/A	99.673(2)
V, $Å^3$	5117.8(3)	2502.7(4)
space group	$Pca2_1$ (#29)	$P2_1/n$ (#14)
Z value	8	4
D_{calc}, g/cm^3	1.628	1.595
F_{000}	2496.00	1188.00
μ(MoKα), cm^{-1}	18.99	82.36
detector position, mm	60.00	60.00
temperature, °C	-104	-108
scan type (°/frame)	ω (0.3)	ω (0.3)
scan rate, s/frame	10.0	10.0
$2\theta_{max}$, °	52.2	52.3
no. rflns. measured:		
total	24726	11879
unique (R_{int})	5212 (0.037)	4708 (0.029)
no. observations (I>3.00s(I))	5339	3012
no. variables	535	249
refln./param. ratio	9.98	12.10
R^a; $R_w{}^b$; R_{all}	0.024; 0.025; 0.038	0.033; 0.046; 0.059
GOF indicator	0.93	1.85
max. shift/error in final cycle	0.00	0.00
max. resid. density, $e^-/Å^3$	0.44	0.59
min. resid. density, $e^-/Å^3$	-0.33	-0.55

a) $R = \Sigma||F_0| - |F_c||/\Sigma|F_0|$. b) $R_w = [\Sigma\omega(|F_0| - |F_0|)^2/\Sigma\omega|F_0|^2]^{1/2}$, $\omega = 1/\sigma^2(F_0)$.

comparison of redundant and equivalent reflections was applied using SADABS.[46] Neutral atom scattering factors were taken from Cromer and Waber.[47] Anomalous dispersion effects were included in F_{calc};[48] the values for Δf' and Δf" were those of Creagh and McAuley.[49] The values for the mass attenuation coefficients are those of Creagh and Hubbel.[50] All calculations were performed using the teXan crystallographic software package of Molecular Structure Corporation.[51]

Structure of 12. Yellow block-shaped crystals of **12**•THF were obtained from a THF solution layered with pentane and cooled to –35 °C. Full metrical parameters are given in Appendix A. The compound crystallizes with one equivalent of THF in the non-centrosymmetric orthorhombic space group $Pca2_1$, with eight formula units in the unit cell. There are two formula units in the asymmetric unit. Although the two Rh molecules in the asymmetric unit are related by a pseudo inversion center, inspection of a packing diagram shows that there is no mirror plane perpendicular to the c-axis, and thus the structure is not in the alternative centrosymmetric space group Pbcm. The correct enantiomorph of the space group was chosen based on a comparison of Friedel equivalent reflections.

One of the two THF solvent molecules in the asymmetric unit is disordered over multiple conformations. This disorder was modeled using both half and full occupancy carbon atoms. The location of the oxygen atom could not be determined because of this disorder.

The structure was solved by direct methods[52] and expanded using Fourier techniques.[53] Excluding the B atoms and partial occupancy C atoms, the non-hydrogen atoms were refined anisotropically. The B atoms and partial occupancy C atoms were

refined isotropically. The hydrides were located in the difference electron density map, but were not refined. The remaining hydrogen atoms were included in calculated idealized positions but not refined.

Structure of 13. Orange-red block-shaped crystals of **13•**(0.5 toluene) were grown by slow vapor diffusion of pentane into a toluene solution at –35 °C. Full metrical parameters are given in Appendix B. The compound crystallizes with half an equivalent of toluene in the monoclinic space group $P2_1/n$ with four formula units in the unit cell. The toluene molecule is disordered about a crystallographic inversion center.

The structure was solved by heavy-atom Patterson methods[54] and expanded using Fourier techniques.[53] The non-hydrogen atoms of the Rh molecule were refined anisotropically, while the carbon atoms of the disordered toluene solvent molecule were refined isotropically. Attempts to refine the toluene carbons anisotropically led to unreasonably large thermal parameters, while alternate disorder models were not stable during least squares refinements. The alpha hydrogen atom (H16) on C11 was located in the difference electron density map and its position was refined with fixed thermal parameters. The remaining hydrogen atoms were included in calculated idealized positions but not refined. Hydrogen atoms were not included on the disordered toluene molecule. Four reflections [(1 1 0), (0 0 2), (1 1 –2), (1 3 0)] with $\Delta F/\sigma F > 20$ were rejected as outliers.

Labeling Studies. Labeled isotopomers of compounds **9**, **11**, **12**, and **13** were prepared by methods directly analogous to those described above for the unlabeled species. Incorporation of ^{13}CO into $[Rh(CO)_2Cl]_2$ was achieved by stirring a benzene solution of the Rh dimer under 1 atm of ^{13}CO for 8 h as detailed in the literature.[55] The boron-deuterated Bp* ligand was prepared as the sodium salt by subjecting $NaBD_4$ and 3,5-dimethylpyrazole to the procedure for synthesis of Bp*K.[22] The reaction was run two times using $NaBD_4$ from different sources (Aldrich, Cambridge Isotope Laboratories), and in both cases IR spectroscopy showed >90 % deuteration in the borate starting material but only 50 % deuteration in the product, as judged by integration of the B-H and B-D stretching bands. Prior to the third attempt, the dimethylpyrazole was treated with stoichiometric *n*-butyllithium and then quenched with a D_2O/THF solution to deuterate the acidic nitrogen; furthermore, a 20 % v/v acetic acid-d_4 / D_2O solution was heated to reflux for 3 h in the glassware to be used for preparation of the d_2-Bp*Na. Despite these precautions, only 60 % deuteration at boron was achieved in the final product. All labeled compounds were characterized by ^1H NMR spectroscopy and exhibited pyrazolyl resonances matching those of the respective unlabeled isotopomers.

Labeled 9. IR (KBr) 2032 (^{13}CO), 1969 (^{13}CO), 1795 (br, B-D) cm^{-1}.

Labeled 11. IR (KBr) 1914 (^{13}CO), 1702 (B-D) cm^{-1}.

Labeled 12. IR (KBr) $\nu_{B\text{-}D}$ should appear in 1700-1800 cm^{-1} region (new peaks appear at 1887 and 1605 cm^{-1}), $\nu_{Rh\text{-}D}$ should appear at 1448 cm^{-1} (region is obscured by a strong pyrazolyl or pyridyl absorption).

Notes and References

1) Trofimenko, S. *Scorpionates: The Coordination Chemistry of Polypyrazolylborate Ligands*; Imperial College: London, 1999.

2) Trofimenko, S. *Chem. Rev.* **1993**, *93*, 943.

3) Kitajima, N.; Tolman, W. B. *Prog. Inorg. Chem.* **1995**, *43*.

4) Baena, M. J.; Reyes, M. L.; Rey, L.; Carmona, E.; Nicasio, M. C.; Pérez, P. J.; Gutiérrez, E.; Monge, A. *Inorg. Chim. Acta* **1998**, *273*, 244.

5) Gutiérrez, E.; Nicasio, M. C.; Paneque, M.; Ruiz, C.; Salazar, V. *J. Organomet. Chem.* **1997**, *549*, 167.

6) Gutiérrez, E.; Hudson, S. A.; Monge, A.; Nicasio, M. C.; Paneque, M.; Ruiz, C. *J. Organomet. Chem.* **1998**, *551*, 215.

7) Hill, A. F.; White, A. J. P.; Williams, D. J.; Wilton-Ely, J. D. E. T. *Organometallics* **1998**, *17*, 4249.

8) Diaz-Requejo, M. M.; Nicasio, M. C.; Perez, P. J. *Organometallics* **1998**, *17*, 3051.

9) Diaz-Requejo, M. M.; Belderrain, T. R.; Nicasio, M. C.; Prieto, F.; Perez, P. J. *Organometallics* **1999**, *18*, 2601.

10) Bonati, F.; Minghetti, G.; Banditelli, G. *J. Organomet. Chem.* **1975**, *87*, 365.

11) Crabtree, R. H. *The Organometallic Chemistry of the Transition Metals*; 2nd ed.; Wiley: New York, 1994.

12) Bromberg, S. E.; Yang, H.; Asplund, M. C.; Lian, T.; McNamara, B. K.; Kotz, K. T.; Yeston, J. S.; Wilkens, M.; Frei, H.; Bergman, R. G.; Harris, C. B. *Science* **1997**, *278*, 260.

13) Oxidative addition of aldehydic C-H bonds has been shown to be particularly facile. See: Alaimo, P. J.; Bergman, R. G. *Organometallics* **2000**, *19*, 2130 and references therein.

14) As noted in the previous chapter, Bp*Rh$(CO)_2$ (**9**) forms a transient solvent adduct upon photolytic extrusion of CO; however, the adduct does not lead to C-H bond activation, presumably due to the lack of a third chelating ligand to stabilize the electron-deficient Rh(III) center in the product. Photolysis of **9** with a nitrogen purge to preclude CO recombination leads to extensive decomposition, characterized by the observation of free dimethylpyrazole in ^{1}H NMR spectra of the reaction mixture.

15) Dotz, K. H.; Fischer, E. O. *Transition Metal Carbene Complexes*; Verlag: Weinheim, 1983.

16) Adams, H.; Bailey, N. A.; Mann, B. E.; Manuel, C. P. *Inorg. Chim. Acta* **1992**, *198*, 111.

17) Bennett, M. A.; Jeffery, J. C.; Robertson, G. B. *Inorg. Chem.* **1981**, *20*, 323.

18) Moloy, K. G.; Petersen, J. L. *Organometallics* **1995**, *14*, 2931.

19) The bond lengths given here for **12** are averaged for two inequivalent molecules in the unit cell. The bond lengths and angles for each individual molecule are given in Appendix A.

20) Dunn, S. C.; Mountford, P.; Shishkin, O. V. *Inorg. Chem.* **1996**, *35*, 1006.

21) Sanders, J. K. M.; Hunter, B. K. *Modern NMR Spectroscopy*; Oxford University Press: Oxford, 1987 p. 210.

22) Trofimenko, S. *Inorg. Chem.* **1970**, *9*, 2493.

23) The carbene product **12**-d_2 was independently characterized and exhibited a Rh-D resonance at –14.2 ppm in the ^{2}H NMR spectrum.

24) DeKock, R. L.; Gray, H. B. *Chemical Structure and Bonding*; University Science Books: Sausalito, 1989.

25) Collman, J. P.; Hegedus, L. S.; Norton, J. R.; Finke, R. G. *Applications of Organotransition Metal Chemistry*; University Science Books: Mill Valley, 1987.

26) Labinger, J. A.; Osborn, J. A. *Inorg. Chem.* **1980**, *19*, 3230 and references therein.

27) Recently Hill and co-workers reported intramolecular B-H oxidative addition at Ru from the related hydridotris(2-sulfanyl-1-methylimidazolyl)borate ligand: Hill, A. F.; Owen, G. R.; White, A. J. P.; Williams, D. J. *Angew. Chem. Int. Ed.* **1999**, *38*, 2759.

28) Hill, A. F.; Malget, J. M. *J. Chem. Soc., Dalton Trans.* **1997**, 2003.

29) Das, M. K.; Bhaumik, A. *Indian J. Chem. Sec. B* **1997**, *36B*, 1020.

30) Pizzano, A.; Sánchez, L.; Gutiérrez, E.; Monge, A.; Carmona, E. *Organometallics* **1995**, *14*, 14.

31) Gorrell, I. B.; Looney, A.; Parkin, G.; Rheingold, A. L. *J. Am. Chem. Soc.* **1990**, *112*, 4068 and references therein.

32) Ghosh, P.; Bonanno, J. B.; Parkin, G. *J. Chem. Soc., Dalton Trans.* **1998**, 2779.

33) Reger, D. L.; Lindeman, J. A.; Lebioda, L. *Inorg. Chem.* **1988**, *27*, 1890.

34) King, R. B.; Bond, A. *J. Am. Chem. Soc.* **1974**, *96*, 1338.

35) The question also arises whether pyridine dissociation occurs at any stage along the reaction coordinate. Unfortunately, this possibility could not easily be tested by addition of free pyridine to the reaction mixture, since under those conditions quaternization of the pyridine by iodomethane is a competitive process.

36) Butts, S. B.; Strauss, S. H.; Holt, E. M.; Stimson, R. E.; Alcock, N. W.; Shriver, D. F. *J. Am. Chem. Soc.* **1980**, *102*, 5093.

37) Richmond, T. G.; Basolo, F.; Shriver, D. F. *Inorg. Chem.* **1982**, *21*, 1272.

38) St. Clair, M. A.; Santarsiero, B. D.; Bercaw, J. E. *Organometallics* **1989**, *8*, 17.

39) Erker, G.; Mena, M.; Hoffmann, U.; Menjón, B. *Organometallics* **1991**, *10*, 291.

40) For a recent example of hydride migration from a metal center to an alkylidene carbon, see: Alias, F. M.; Poveda, M. L.; Sellin, M.; Carmona, E. *J. Am. Chem. Soc.* **1998**, *120*, 5816 and references therein.

41) For an example of reversible α-hydride migration, see: Parkin, G.; Bunel, E.; Burger, B. J.; Trimmer, M. S.; Van Asselt, A.; Bercaw, J. E. *J. Mol. Catal.* **1987**, *41*, 21.

42) For a recent example of alkyl migration from a metal center to an alkylidene carbon, see: Muir, J. E.; Haynes, A.; Winter, M. J. *Chem. Commun.* **1996**, 1765and references therein.

43) SMART: Area-Detector Software Package, Siemens Industrial Automation, Inc.: Madison, WI 1995.

44) SAINT: SAX Area-Detector Integration Program, V4.024, Siemens Industrial Automation, Inc.: Madison, WI 1995.

45) XPREP: v 5.03 Part of the SHELXTL Crystal Structure Determination, Siemens Industrial Automation, Inc.: Madison, WI 1995.

46) SADABS: Siemens Area Detector ABSorption correction program, Sheldrick, G. 1996, advance copy, private communication.

47) Cromer, D. T.; Waber, J. T. "International Tables for X-ray Crystallography,", Vol. IV, Birmingham (U. K.): Kynoch Press 1974, Table 2.2 A.

48) Ibers, J. A.; Hamilton, W. C. *Acta Crystallogr.* **1964**, *17*, 781.

49) Creagh, D. C.; McAuley, W. J. in "International Tables for Crystallography", Vol. C, ed. Wilson, A. J. C. Boston: Kluwer Academic Publishers 1992, Table 4.2.6.8 pp. 219-222.

50) Creagh, D. C.; Hubbell, J. H. *ibid.* Table 4.2.4.3, pp. 200-206.

51) teXan: Crystal Structure Analysis Package, Molecular Structure Corporation (1992, 1985).

52) SIR92: Altomare, A.; Cascarano, M.; Giacovazzo, C.; Guagliardi, A. *J. Appl. Cryst.* **1993**, *26*, 343.

53) DIRDIF94: Beurskens, P. T.; Admiraal, G.; Beurskens, G.; Bosman, W. P.; de Gelder, R.; Israel, R.; Smits, J. M. M. The DIRDIF-94 program system, Technical Report of the Crystallography Library, University of Nijmegen, The Netherlands (1994).

54) PATTY: Beurskens, P. T.; Admiraal, G.; Beurskens, G.; Bosman, W. P.; Garcia-Granda, S.; Gould, R. O.; Smits, J. M. M.; Smykalla, C. The DIRDIF program system, Technical Report of the Crystallography Library, University of Nijmegen, The Netherlands (1992).

55) Adams, H.; Bailey, N. A.; Mann, B. E.; Manuel, C. P.; Spencer, C. M.; Kent, A. G. *J. Chem. Soc. Dalton Trans.* **1988**, 489.

Chapter 4 Appendices

Figure A-1. ORTEP diagram of one of two molecules of **12** in the unit cell. Hydrogen atoms have been omitted for clarity. Thermal ellipsoids are shown at 50% probability.

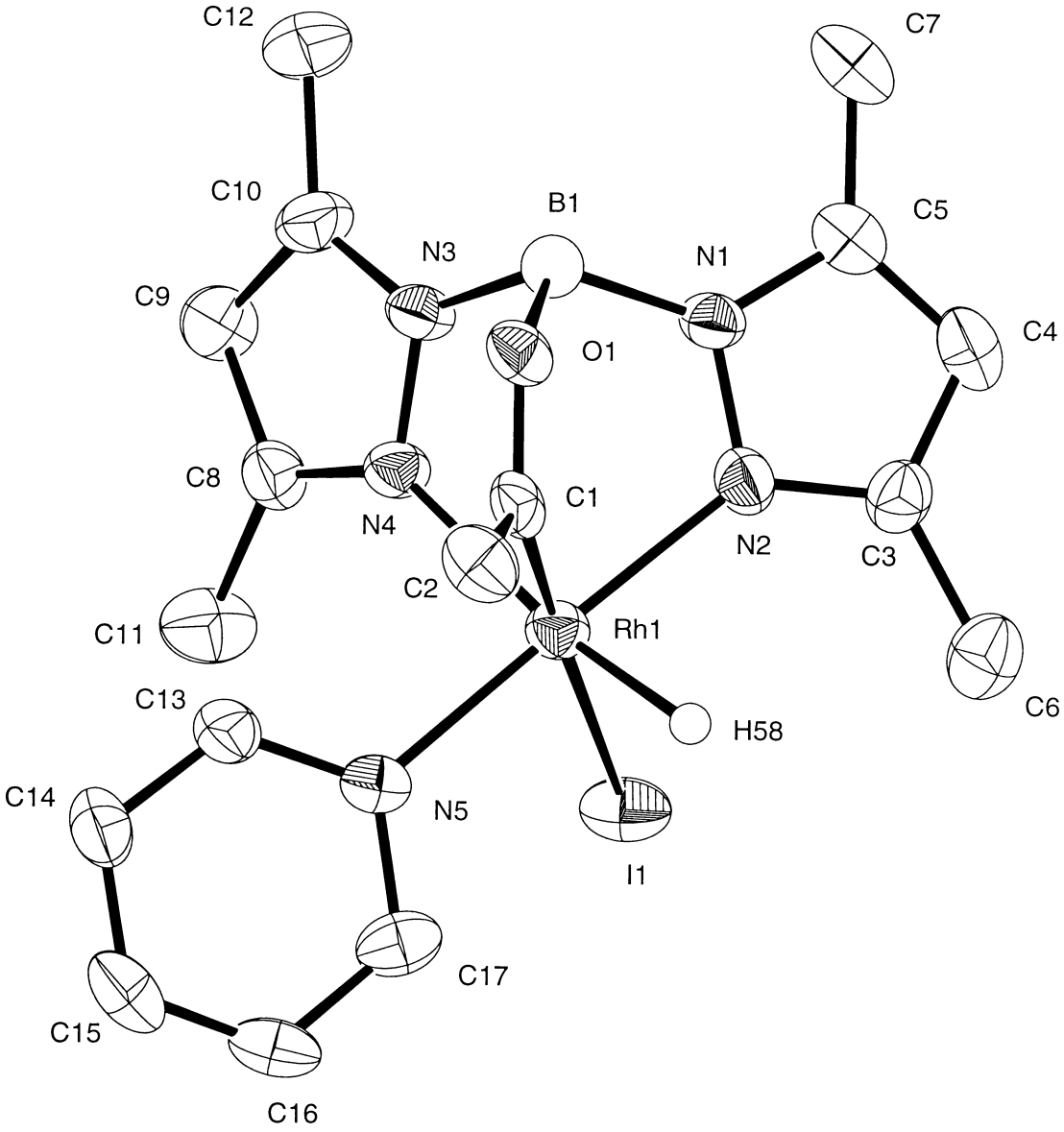

Figure A-2. ORTEP diagram of the second of two molecules of **12** in the unit cell. Hydrogen atoms have been omitted for clarity. Thermal ellipsoids are shown at 50% probability.

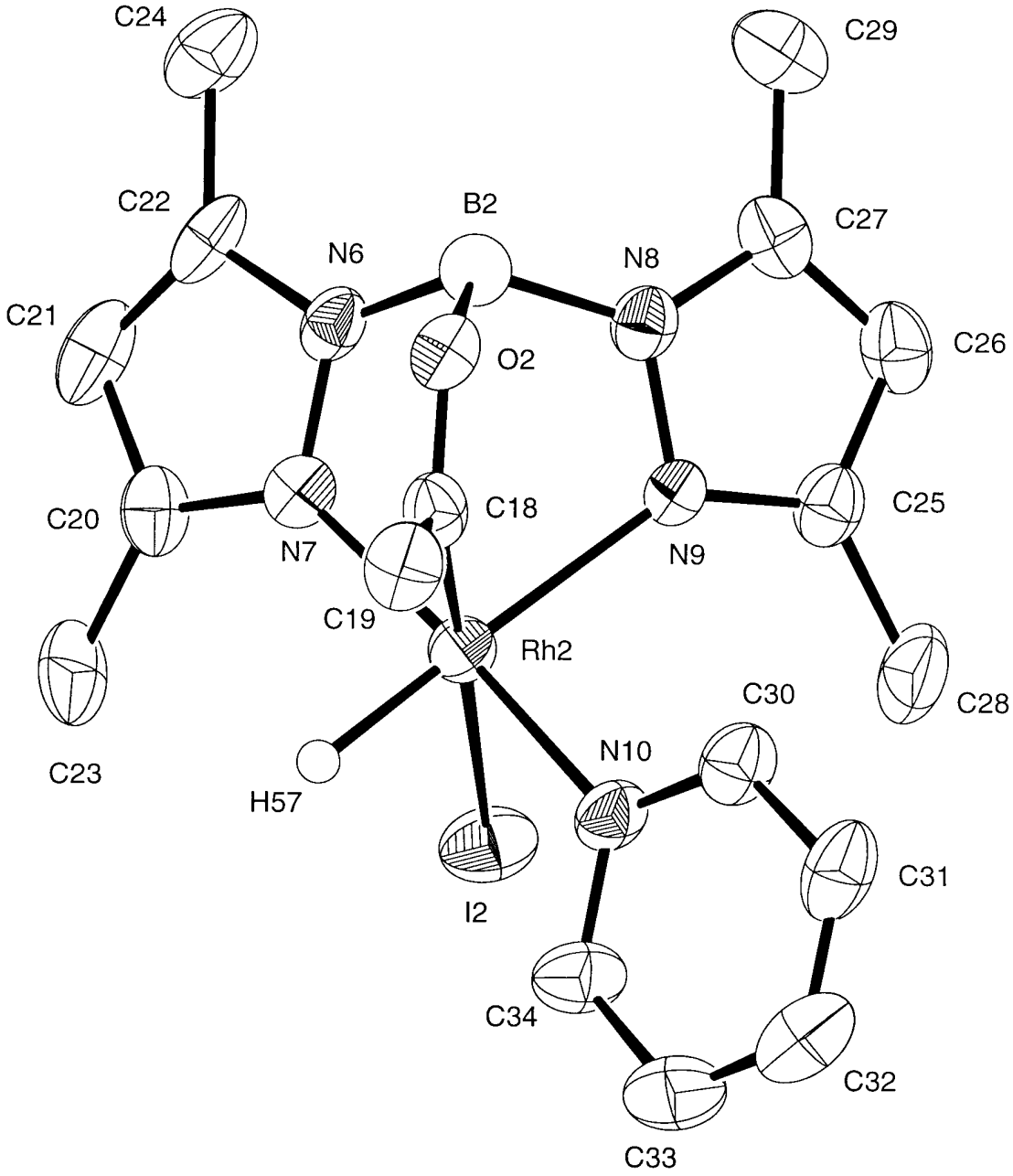

Figure A-3. ORTEP diagram of two THF molecules (one of which is disordered) which co-crystallized with **12** in the unit cell. Hydrogen atoms have been omitted for clarity. Thermal ellipsoids are shown at 50% probability.

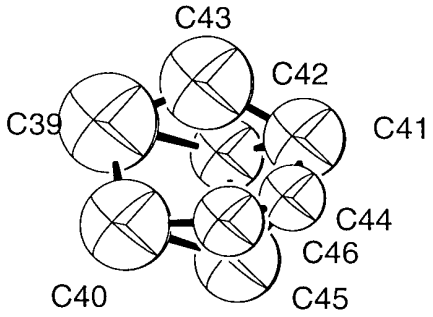

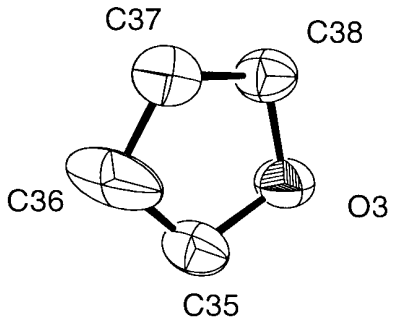

Table A-1. Atomic Coordinates and B_{iso}/B_{eq} for **12**.

atom	x	y	z	B(eq)
I(1)	-1.16948(2)	-0.45589(3)	-0.5005	3.443(11)
I(2)	-0.65409(3)	-0.03452(3)	-0.29376(4)	3.853(12)
Rh(1)	-1.07249(2)	-0.44289(3)	-0.37560(5)	2.307(11)
Rh(2)	-0.74678(3)	-0.05140(3)	-0.42307(5)	2.431(11)
O(1)	-0.9940(2)	-0.3609(2)	-0.2579(3)	2.60(11)
O(2)	-0.8197(2)	-0.1393(3)	-0.5414(3)	2.88(11)
O(3)	-1.0776(2)	-0.4437(3)	-0.1015(3)	4.53(13)
N(1)	-1.0249(3)	-0.2679(3)	-0.3703(4)	2.37(12)
N(2)	-1.0326(3)	-0.3344(3)	-0.4228(4)	2.59(13)
N(3)	-1.1124(3)	-0.3013(3)	-0.2638(3)	2.45(13)
N(4)	-1.1436(3)	-0.3695(3)	-0.2996(4)	2.41(13)
N(5)	-1.1066(3)	-0.5558(3)	-0.3286(4)	2.34(13)
N(6)	-0.7945(2)	-0.2261(3)	-0.4236(4)	2.72(13)
N(7)	-0.7881(3)	-0.1576(3)	-0.3737(4)	2.56(13)
N(8)	-0.7006(3)	-0.1990(3)	-0.5262(3)	2.60(13)
N(9)	-0.6717(3)	-0.1267(3)	-0.4931(4)	2.44(13)
N(10)	-0.7123(3)	0.0609(3)	-0.4717(4)	2.86(14)
C(1)	-1.0045(3)	-0.4318(3)	-0.2923(5)	2.41(14)
C(2)	-0.9592(4)	-0.4993(4)	-0.2587(4)	3.21(17)
C(3)	-1.0077(3)	-0.3097(4)	-0.4927(5)	2.88(16)
C(4)	-0.9868(4)	-0.2260(4)	-0.4888(5)	3.25(18)
C(5)	-0.9962(3)	-0.2017(4)	-0.4099(5)	2.73(16)
C(6)	-1.0044(4)	-0.3658(4)	-0.5666(5)	3.7(2)
C(7)	-0.9842(3)	-0.1202(4)	-0.3711(5)	3.63(17)
C(8)	-1.2097(4)	-0.3706(4)	-0.2731(4)	2.72(17)
C(9)	-1.2210(4)	-0.3038(4)	-0.2210(5)	3.48(18)
C(10)	-1.1586(4)	-0.2609(4)	-0.2162(5)	3.24(18)
C(11)	-1.2599(3)	-0.4369(4)	-0.2959(6)	3.96(18)
C(12)	-1.1407(4)	-0.1849(4)	-0.1681(5)	4.3(2)
C(13)	-1.1240(4)	-0.5637(4)	-0.2503(5)	2.84(17)
C(14)	-1.1471(4)	-0.6365(4)	-0.2160(5)	3.3(2)
C(15)	-1.1526(4)	-0.7082(5)	-0.2642(6)	3.8(2)
C(16)	-1.1358(4)	-0.7016(4)	-0.3431(6)	3.3(2)
C(17)	-1.1125(3)	-0.6258(4)	-0.3751(5)	3.13(16)
C(18)	-0.8118(3)	-0.0676(4)	-0.5080(5)	2.71(15)
C(19)	-0.8585(4)	-0.0021(4)	-0.5446(5)	3.52(18)
C(20)	-0.8160(4)	-0.1766(4)	-0.3025(5)	3.00(17)
C(21)	-0.8401(4)	-0.2593(4)	-0.3071(5)	3.7(2)
C(22)	-0.8261(3)	-0.2887(4)	-0.3821(5)	3.04(17)
C(23)	-0.8229(4)	-0.1169(5)	-0.2355(5)	4.3(2)
C(24)	-0.8391(4)	-0.3727(4)	-0.4193(6)	4.2(2)
C(25)	-0.6050(3)	-0.1283(4)	-0.5132(5)	3.02(17)

Table A-1. Atomic Coordinates and B_{iso}/B_{eq} for **12** (cont.).

atom	x	y	z	B(eq)
C(26)	-0.5904(4)	-0.2005(4)	-0.5576(5)	3.38(18)
C(27)	-0.6518(4)	-0.2432(4)	-0.5637(5)	2.94(17)
C(28)	-0.5551(4)	-0.0580(5)	-0.4899(6)	4.6(2)
C(29)	-0.6661(4)	-0.3248(4)	-0.6047(5)	4.0(2)
C(30)	-0.6954(4)	0.0670(4)	-0.5481(5)	3.3(2)
C(31)	-0.6741(4)	0.1416(5)	-0.5842(6)	4.0(2)
C(32)	-0.6696(4)	0.2119(5)	-0.5367(7)	4.1(2)
C(33)	-0.6872(4)	0.2073(4)	-0.4582(6)	4.1(2)
C(34)	-0.7085(4)	0.1298(4)	-0.4269(5)	3.62(18)
C(35)	-1.1417(4)	-0.4371(5)	-0.0605(5)	4.8(2)
C(36)	-1.1359(5)	-0.3703(8)	0.0015(7)	10.2(4)
C(37)	-1.0637(4)	-0.3489(5)	0.0081(6)	5.0(2)
C(38)	-1.0302(4)	-0.3866(4)	-0.0651(5)	4.1(2)
C(39)	-0.4446(8)	-0.0949(9)	-0.2679(9)	12.5(4)
C(40)	-0.4783(7)	-0.1715(8)	-0.2257(8)	10.4(4)
C(41)	-0.3719(12)	-0.2037(15)	-0.3215(15)	8.2(5)
C(42)	-0.4181(11)	-0.1583(12)	-0.3495(13)	6.7(5)
C(43)	-0.3869(15)	-0.1223(17)	-0.302(2)	10.9(7)
C(44)	-0.3967(11)	-0.2444(11)	-0.2653(13)	5.5(4)
C(45)	-0.4538(13)	-0.2376(14)	-0.2893(18)	9.1(6)
C(46)	-0.4303(12)	-0.2307(12)	-0.2260(14)	6.2(4)
B(1)	-1.0355(4)	-0.2831(4)	-0.2814(5)	2.35(15)
B(2)	-0.7763(4)	-0.2163(4)	-0.5103(6)	2.82(15)

Table A-2. Anisotropic Displacement Parameters for **12**.

atom	**U11**	**U22**	**U33**	**U12**	**U13**	**U23**
I(1)	0.0465(3)	0.0351(2)	0.0492(4)	0.0018(2)	-0.0149(3)	-0.0065(2)
I(2)	0.0595(3)	0.0419(3)	0.0450(3)	-0.0065(2)	-0.0150(3)	0.0014(3)
Rh(1)	0.0285(3)	0.0261(2)	0.0331(3)	0.0002(2)	0.0011(3)	-0.0022(3)
Rh(2)	0.0344(3)	0.0268(2)	0.0312(3)	0.0003(2)	0.0013(3)	0.0032(3)
O(1)	0.026(3)	0.032(2)	0.042(3)	-0.006(2)	0.001(2)	0.001(2)
O(2)	0.032(3)	0.039(3)	0.038(3)	-0.005(2)	0.000(2)	0.005(2)
O(3)	0.047(3)	0.062(3)	0.063(4)	-0.013(3)	0.004(3)	-0.018(3)
N(1)	0.033(3)	0.026(3)	0.030(4)	-0.005(2)	-0.004(3)	-0.002(3)
N(2)	0.036(3)	0.029(3)	0.034(4)	-0.001(2)	0.005(3)	0.005(3)
N(3)	0.028(3)	0.025(3)	0.040(4)	-0.004(2)	0.000(3)	-0.005(3)
N(4)	0.027(3)	0.026(2)	0.039(4)	0.000(2)	0.005(3)	-0.007(3)
N(5)	0.026(3)	0.026(3)	0.037(4)	0.002(3)	-0.004(3)	-0.003(3)
N(6)	0.025(3)	0.028(3)	0.051(4)	0.001(2)	0.004(3)	0.007(3)
N(7)	0.030(3)	0.033(3)	0.034(4)	0.001(2)	-0.004(3)	0.004(3)
N(8)	0.033(3)	0.032(3)	0.034(4)	0.000(3)	0.002(3)	0.007(3)
N(9)	0.028(3)	0.032(3)	0.033(4)	-0.006(2)	0.003(3)	-0.001(3)
N(10)	0.039(4)	0.026(3)	0.043(4)	-0.003(3)	0.003(3)	0.006(3)
C(1)	0.021(4)	0.033(3)	0.037(4)	-0.006(3)	0.007(4)	0.003(4)
C(2)	0.041(4)	0.035(3)	0.046(5)	0.002(3)	-0.006(4)	0.011(3)
C(3)	0.036(4)	0.038(4)	0.035(5)	0.006(3)	0.006(4)	0.000(4)
C(4)	0.035(4)	0.037(4)	0.051(6)	0.000(3)	0.008(4)	0.014(4)
C(5)	0.028(4)	0.032(3)	0.044(5)	0.001(3)	-0.005(4)	0.005(3)
C(6)	0.051(5)	0.052(4)	0.039(5)	0.008(4)	0.002(4)	0.004(4)
C(7)	0.038(4)	0.034(3)	0.065(6)	-0.008(3)	-0.005(5)	0.011(4)
C(8)	0.031(4)	0.033(3)	0.039(5)	-0.002(3)	0.005(4)	0.003(3)
C(9)	0.029(4)	0.039(4)	0.065(6)	0.006(3)	0.017(4)	-0.008(4)
C(10)	0.056(5)	0.030(4)	0.037(5)	0.004(3)	0.003(4)	-0.008(3)
C(11)	0.029(4)	0.053(4)	0.068(6)	0.000(3)	-0.008(5)	-0.014(5)
C(12)	0.066(5)	0.036(4)	0.060(6)	0.005(4)	0.012(5)	-0.015(4)
C(13)	0.033(4)	0.033(4)	0.042(5)	-0.005(3)	0.006(4)	-0.004(4)
C(14)	0.039(5)	0.047(4)	0.040(6)	-0.011(4)	0.004(4)	0.008(4)
C(15)	0.040(5)	0.038(4)	0.066(7)	-0.012(3)	0.004(5)	0.011(4)
C(16)	0.041(5)	0.030(4)	0.056(6)	-0.005(3)	-0.016(5)	-0.007(4)
C(17)	0.037(4)	0.038(4)	0.044(5)	0.010(3)	-0.006(4)	-0.011(4)
C(18)	0.038(4)	0.034(3)	0.032(4)	0.002(3)	0.007(4)	0.006(4)
C(19)	0.039(5)	0.044(4)	0.051(5)	0.004(3)	0.001(4)	0.010(4)
C(20)	0.034(4)	0.051(4)	0.029(5)	0.003(3)	0.001(4)	0.011(4)
C(21)	0.036(4)	0.057(4)	0.048(6)	-0.008(4)	-0.008(5)	0.033(4)
C(22)	0.022(4)	0.038(3)	0.056(6)	-0.007(3)	-0.009(4)	0.022(4)
C(23)	0.059(6)	0.074(5)	0.032(5)	-0.006(5)	0.017(4)	0.013(4)
C(24)	0.049(5)	0.034(4)	0.077(6)	-0.003(3)	-0.004(5)	0.018(4)
C(25)	0.030(4)	0.040(4)	0.045(5)	0.002(3)	0.001(4)	0.008(4)

Table A-2. Anisotropic Displacement Parameters for **12** (cont.).

atom	**U11**	**U22**	**U33**	**U12**	**U13**	**U23**
C(26)	0.039(5)	0.042(4)	0.047(5)	0.014(3)	0.009(4)	0.011(4)
C(27)	0.041(5)	0.038(4)	0.033(5)	0.013(3)	0.003(4)	0.007(3)
C(28)	0.032(4)	0.061(4)	0.082(7)	-0.005(4)	0.015(5)	0.007(5)
C(29)	0.079(6)	0.039(4)	0.036(5)	0.011(4)	0.003(5)	0.004(3)
C(30)	0.041(5)	0.035(4)	0.047(6)	0.000(3)	0.001(4)	0.011(4)
C(31)	0.042(5)	0.048(5)	0.062(7)	-0.003(4)	0.006(5)	0.025(5)
C(32)	0.041(5)	0.041(4)	0.074(8)	-0.006(4)	-0.018(5)	0.018(5)
C(33)	0.060(6)	0.033(4)	0.064(7)	0.003(4)	-0.011(5)	-0.001(4)
C(34)	0.062(5)	0.028(3)	0.047(5)	-0.001(3)	-0.006(5)	0.004(4)
C(35)	0.050(5)	0.071(5)	0.062(6)	-0.012(4)	0.007(5)	0.004(5)
C(36)	0.087(8)	0.208(12)	0.094(9)	-0.077(8)	0.068(7)	-0.097(9)
C(37)	0.062(6)	0.068(5)	0.059(6)	-0.006(4)	-0.006(5)	0.009(5)
C(38)	0.054(5)	0.057(5)	0.045(5)	-0.010(4)	-0.002(4)	-0.003(4)

Table A-3. Bond Lengths (Å) for **12**.

atom	atom	distance	atom	atom	distance
I(1)	Rh(1)	2.8028(7)	C(1)	C(2)	1.496(8)
I(2)	Rh(2)	2.8095(8)	C(3)	C(4)	1.397(8)
Rh(1)	N(2)	2.052(5)	C(3)	C(6)	1.52(1)
Rh(1)	N(4)	2.202(5)	C(4)	C(5)	1.38(1)
Rh(1)	N(5)	2.072(5)	C(5)	C(7)	1.472(9)
Rh(1)	C(1)	1.915(7)	C(8)	C(9)	1.393(9)
Rh(2)	N(7)	2.045(5)	C(8)	C(11)	1.482(8)
Rh(2)	N(9)	2.213(5)	C(9)	C(10)	1.386(9)
Rh(2)	N(10)	2.077(5)	C(10)	C(12)	1.495(9)
Rh(2)	C(18)	1.907(7)	C(13)	C(14)	1.368(9)
O(1)	C(1)	1.285(7)	C(14)	C(15)	1.40(1)
O(1)	B(1)	1.528(8)	C(15)	C(16)	1.36(1)
O(2)	C(18)	1.282(7)	C(16)	C(17)	1.40(1)
O(2)	B(2)	1.574(8)	C(18)	C(19)	1.506(9)
O(3)	C(35)	1.415(8)	C(20)	C(21)	1.403(9)
O(3)	C(38)	1.424(8)	C(20)	C(23)	1.47(1)
N(1)	N(2)	1.383(7)	C(21)	C(22)	1.36(1)
N(1)	C(5)	1.363(7)	C(22)	C(24)	1.498(9)
N(1)	B(1)	1.51(1)	C(25)	C(26)	1.399(9)
N(2)	C(3)	1.319(9)	C(25)	C(28)	1.528(9)
N(3)	N(4)	1.380(6)	C(26)	C(27)	1.368(9)
N(3)	C(10)	1.353(8)	C(27)	C(29)	1.50(1)
N(3)	B(1)	1.536(9)	C(30)	C(31)	1.396(9)
N(4)	C(8)	1.345(8)	C(31)	C(32)	1.38(1)
N(5)	C(13)	1.353(8)	C(32)	C(33)	1.35(1)
N(5)	C(17)	1.365(8)	C(33)	C(34)	1.40(1)
N(6)	N(7)	1.379(7)	C(35)	C(36)	1.49(1)
N(6)	C(22)	1.358(8)	C(36)	C(37)	1.43(1)
N(6)	B(2)	1.50(1)	C(37)	C(38)	1.50(1)
N(7)	C(20)	1.338(9)	C(39)	C(40)	1.55(2)
N(8)	N(9)	1.395(7)	C(39)	C(42)	1.77(2)
N(8)	C(27)	1.331(8)	C(39)	C(43)	1.32(3)
N(8)	B(2)	1.507(9)	C(40)	C(45)	1.57(3)
N(9)	C(25)	1.326(8)	C(40)	C(46)	1.32(2)
N(10)	C(30)	1.317(9)	C(41)	C(42)	1.24(3)
N(10)	C(34)	1.330(8)	C(41)	C(43)	1.37(3)

Table A-3. Bond Lengths (Å) for **12** (cont.).

atom	atom	distance
C(41)	C(44)	1.24(3)
C(41)	C(45)	1.75(3)
C(42)	C(43)	1.15(3)
C(42)	C(45)	1.75(3)
C(44)	C(45)	1.17(3)
C(44)	C(46)	0.95(2)
C(45)	C(46)	1.15(3)

Table A-4. Bond Angles (°) for **12**.

atom	atom	atom	angle	atom	atom	atom	angle
I(1)	Rh(1)	N(2)	91.5(2)	C(22)	N(6)	B(2)	132.3(6)
I(1)	Rh(1)	N(4)	93.0(2)	Rh(2)	N(7)	N(6)	116.8(4)
I(1)	Rh(1)	N(5)	90.3(2)	Rh(2)	N(7)	C(20)	134.5(5)
I(1)	Rh(1)	C(1)	178.2(2)	N(6)	N(7)	C(20)	108.6(5)
N(2)	Rh(1)	N(4)	90.2(2)	N(9)	N(8)	C(27)	110.1(5)
N(2)	Rh(1)	N(5)	176.4(2)	N(9)	N(8)	B(2)	117.9(5)
N(2)	Rh(1)	C(1)	86.8(2)	C(27)	N(8)	B(2)	131.9(6)
N(4)	Rh(1)	N(5)	92.8(2)	Rh(2)	N(9)	N(8)	113.4(4)
N(4)	Rh(1)	C(1)	87.7(2)	Rh(2)	N(9)	C(25)	140.9(5)
N(5)	Rh(1)	C(1)	91.3(2)	N(8)	N(9)	C(25)	105.7(5)
I(2)	Rh(2)	N(7)	91.0(2)	Rh(2)	N(10)	C(30)	121.3(5)
I(2)	Rh(2)	N(9)	92.4(2)	Rh(2)	N(10)	C(34)	120.9(5)
I(2)	Rh(2)	N(10)	90.7(2)	C(30)	N(10)	C(34)	117.8(6)
I(2)	Rh(2)	C(18)	177.0(2)	Rh(1)	C(1)	O(1)	120.8(4)
N(7)	Rh(2)	N(9)	90.9(2)	Rh(1)	C(1)	C(2)	127.1(5)
N(7)	Rh(2)	N(10)	175.5(2)	O(1)	C(1)	C(2)	112.1(6)
N(7)	Rh(2)	C(18)	86.0(2)	N(2)	C(3)	C(4)	110.5(6)
N(9)	Rh(2)	N(10)	93.2(2)	N(2)	C(3)	C(6)	123.5(6)
N(9)	Rh(2)	C(18)	88.0(2)	C(4)	C(3)	C(6)	126.0(7)
N(10)	Rh(2)	C(18)	92.2(2)	C(3)	C(4)	C(5)	105.9(6)
C(1)	O(1)	B(1)	121.3(5)	N(1)	C(5)	C(4)	107.2(6)
C(18)	O(2)	B(2)	119.4(5)	N(1)	C(5)	C(7)	122.5(7)
C(35)	O(3)	C(38)	107.8(6)	C(4)	C(5)	C(7)	130.2(6)
N(2)	N(1)	C(5)	109.4(6)	N(4)	C(8)	C(9)	110.0(6)
N(2)	N(1)	B(1)	118.8(5)	N(4)	C(8)	C(11)	122.8(6)
C(5)	N(1)	B(1)	130.7(6)	C(9)	C(8)	C(11)	127.1(7)
Rh(1)	N(2)	N(1)	116.5(4)	C(8)	C(9)	C(10)	106.1(6)
Rh(1)	N(2)	C(3)	136.6(5)	N(3)	C(10)	C(9)	107.5(6)
N(1)	N(2)	C(3)	106.8(5)	N(3)	C(10)	C(12)	123.3(6)
N(4)	N(3)	C(10)	110.1(5)	C(9)	C(10)	C(12)	129.2(7)
N(4)	N(3)	B(1)	119.1(5)	N(5)	C(13)	C(14)	124.2(7)
C(10)	N(3)	B(1)	130.8(5)	C(13)	C(14)	C(15)	118.6(7)
Rh(1)	N(4)	N(3)	113.5(4)	C(14)	C(15)	C(16)	118.2(7)
Rh(1)	N(4)	C(8)	140.2(4)	C(15)	C(16)	C(17)	120.9(7)
N(3)	N(4)	C(8)	106.3(5)	N(5)	C(17)	C(16)	121.3(8)
Rh(1)	N(5)	C(13)	121.6(5)	Rh(2)	C(18)	O(2)	121.4(5)
Rh(1)	N(5)	C(17)	121.6(5)	Rh(2)	C(18)	C(19)	126.7(5)
C(13)	N(5)	C(17)	116.8(6)	O(2)	C(18)	C(19)	111.9(6)
N(7)	N(6)	C(22)	108.6(6)	N(7)	C(20)	C(21)	107.3(7)
N(7)	N(6)	B(2)	118.5(5)	N(7)	C(20)	C(23)	124.2(6)

Table A-4. Bond Angles (°) for **12** (cont.).

atom	atom	atom	angle
C(21)	C(20)	C(23)	128.4(7)
C(20)	C(21)	C(22)	108.0(6)
N(6)	C(22)	C(21)	107.5(6)
N(6)	C(22)	C(24)	121.5(7)
C(21)	C(22)	C(24)	130.9(7)
N(9)	C(25)	C(26)	110.1(6)
N(9)	C(25)	C(28)	122.0(6)
C(26)	C(25)	C(28)	127.9(6)
C(25)	C(26)	C(27)	106.1(6)
N(8)	C(27)	C(26)	108.0(6)
N(8)	C(27)	C(29)	123.2(7)
C(26)	C(27)	C(29)	128.8(7)
N(10)	C(30)	C(31)	123.5(7)
C(30)	C(31)	C(32)	117.9(8)
C(31)	C(32)	C(33)	119.7(8)
C(32)	C(33)	C(34)	118.7(8)
N(10)	C(34)	C(33)	122.4(8)
O(3)	C(35)	C(36)	108.8(6)
C(35)	C(36)	C(37)	107.2(8)
C(36)	C(37)	C(38)	105.0(7)
O(3)	C(38)	C(37)	109.1(6)
C(40)	C(39)	C(42)	91(1)
C(40)	C(39)	C(43)	107(2)
C(42)	C(39)	C(43)	40(1)
C(39)	C(40)	C(45)	96(1)
C(39)	C(40)	C(46)	106(1)
C(45)	C(40)	C(46)	46(1)
C(42)	C(41)	C(43)	52(2)
C(42)	C(41)	C(44)	108(2)
C(42)	C(41)	C(45)	69(2)
C(43)	C(41)	C(44)	104(2)
C(43)	C(41)	C(45)	92(2)
C(44)	C(41)	C(45)	42(1)
C(39)	C(42)	C(41)	105(2)
C(39)	C(42)	C(43)	48(2)
C(39)	C(42)	C(45)	82(1)
C(41)	C(42)	C(43)	70(2)
C(41)	C(42)	C(45)	69(2)
C(43)	C(42)	C(45)	100(2)
C(39)	C(43)	C(41)	126(3)
C(39)	C(43)	C(42)	91(2)
C(41)	C(43)	C(42)	58(2)
C(41)	C(44)	C(45)	93(2)
C(41)	C(44)	C(46)	132(3)
C(45)	C(44)	C(46)	65(2)
C(40)	C(45)	C(41)	106(2)
C(40)	C(45)	C(42)	91(1)
C(40)	C(45)	C(44)	96(2)
C(40)	C(45)	C(46)	56(2)
C(41)	C(45)	C(42)	41(1)
C(41)	C(45)	C(44)	45(1)
C(41)	C(45)	C(46)	84(2)
C(42)	C(45)	C(44)	84(2)
C(42)	C(45)	C(46)	107(2)
C(44)	C(45)	C(46)	48(2)
C(40)	C(46)	C(44)	130(3)
C(40)	C(46)	C(45)	78(2)
C(44)	C(46)	C(45)	67(2)
O(1)	B(1)	N(1)	108.0(5)
O(1)	B(1)	N(3)	107.5(5)
N(1)	B(1)	N(3)	110.4(6)
O(2)	B(2)	N(6)	106.0(5)
O(2)	B(2)	N(8)	108.2(5)
N(6)	B(2)	N(8)	114.6(6)

Figure B-1. Ortep diagram of **13**. Hydrogen atoms have been omitted for clarity. Thermal ellipsoids are shown at 50% probability.

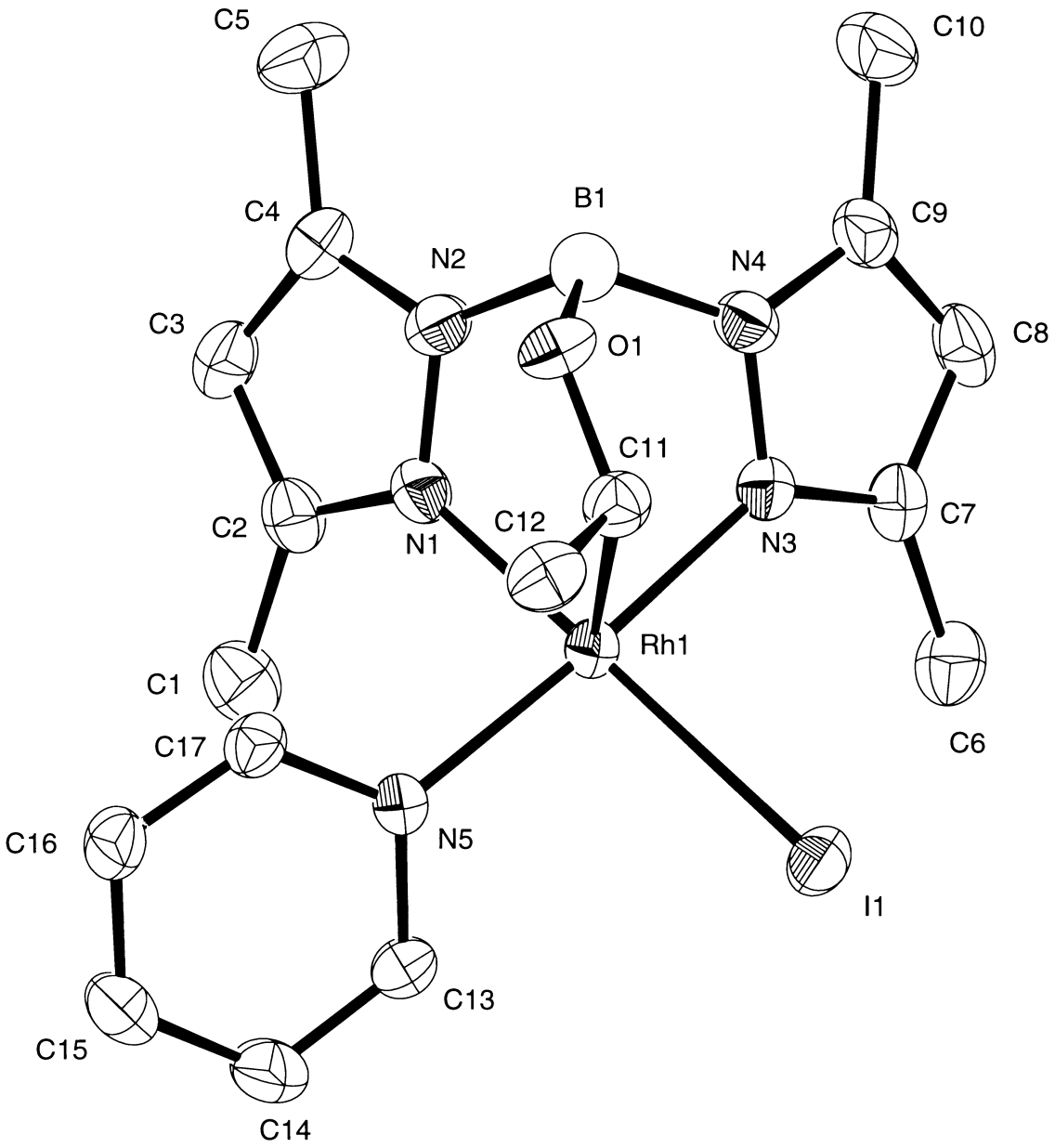

Figure B-2. Ortep diagram of a disordered toluene molecule which co-crystallized in a 1:2 ratio with **13**. Hydrogen atoms have been omitted for clarity. Thermal ellipsoids are shown at 50% probability.

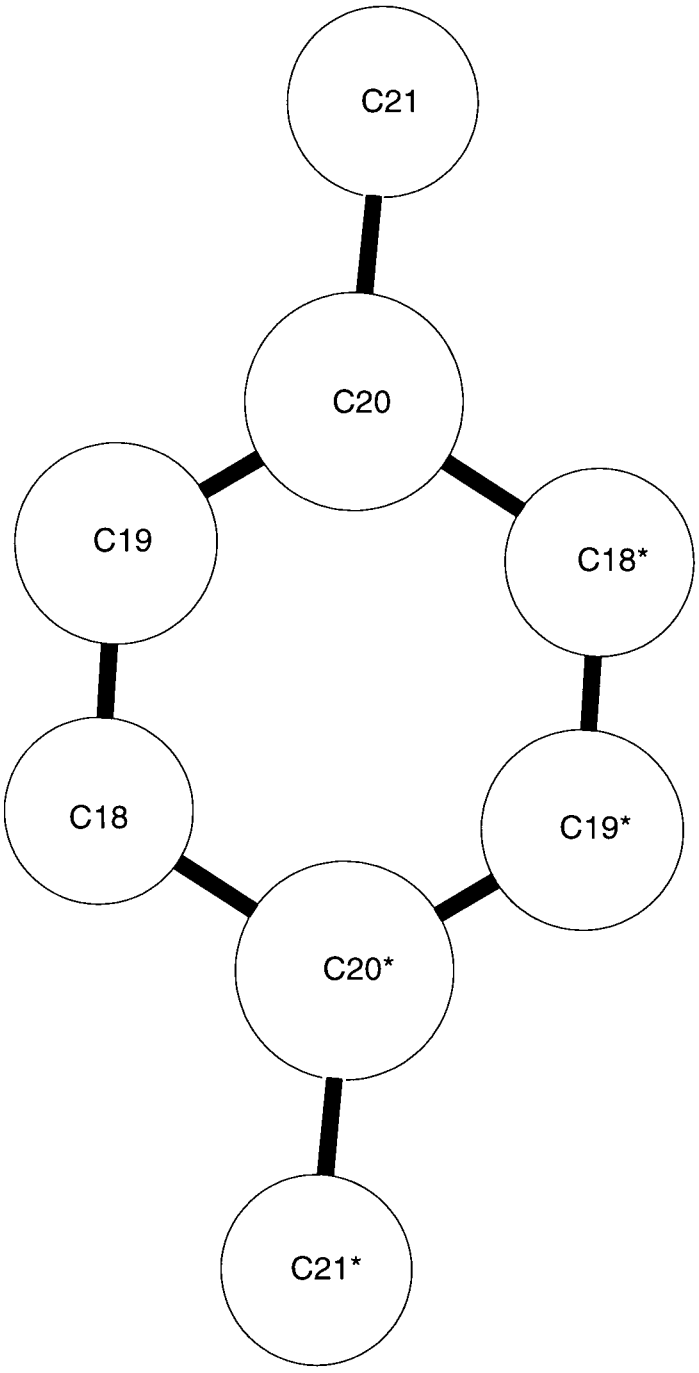

Table B-1. Atomic Coordinates and B_{iso}/B_{eq} for **13**.

atom	x	y	z	B(eq)
I(1)	0.17859(4)	0.14629(2)	0.22833(3)	2.63(1)
Rh(1)	0.29352(5)	0.14876(3)	0.06532(3)	1.87(1)
O(1)	0.2690(5)	0.0198(2)	-0.0422(3)	2.5(1)
N(1)	0.3788(5)	0.1580(3)	-0.0611(4)	2.2(1)
N(2)	0.3267(6)	0.1173(3)	-0.1389(4)	2.3(1)
N(3)	0.1038(5)	0.1549(3)	-0.0267(4)	2.1(1)
N(4)	0.0827(5)	0.1080(3)	-0.1041(4)	2.2(1)
N(5)	0.4934(5)	0.1520(3)	0.1464(3)	2.1(1)
C(1)	0.5483(7)	0.2582(4)	-0.0258(5)	3.3(2)
C(2)	0.4740(6)	0.2015(3)	-0.0890(5)	2.4(1)
C(3)	0.4850(7)	0.1858(4)	-0.1867(5)	2.7(2)
C(4)	0.3913(7)	0.1331(3)	-0.2155(5)	2.5(2)
C(5)	0.3588(8)	0.0958(4)	-0.3123(5)	3.7(2)
C(6)	-0.0204(7)	0.2558(4)	0.0324(5)	3.0(2)
C(7)	-0.0093(6)	0.1964(3)	-0.0352(5)	2.4(1)
C(8)	-0.1039(7)	0.1762(4)	-0.1175(5)	2.9(2)
C(9)	-0.0432(7)	0.1210(4)	-0.1603(5)	2.7(2)
C(10)	-0.0973(8)	0.0824(4)	-0.2525(5)	3.9(2)
C(11)	0.2631(7)	0.0399(3)	0.0518(5)	2.4(2)
C(12)	0.3549(7)	-0.0041(3)	0.1236(5)	2.7(2)
C(13)	0.5260(7)	0.1998(3)	0.2195(5)	2.6(2)
C(14)	0.6609(7)	0.2127(4)	0.2645(5)	3.5(2)
C(15)	0.7699(7)	0.1749(4)	0.2363(5)	3.6(2)
C(16)	0.7398(7)	0.1254(3)	0.1629(5)	2.7(2)
C(17)	0.6016(7)	0.1161(3)	0.1191(4)	2.1(1)
C(18)	0.364(1)	0.0161(6)	0.4449(8)	7.7(3)
C(19)	0.480(1)	0.0538(7)	0.4303(9)	8.9(3)
C(20)	0.618(2)	0.0434(8)	0.483(1)	10.5(4)
C(21)	0.754(3)	0.078(1)	0.459(2)	8.0(6)
B(1)	0.2089(8)	0.0638(4)	-0.1240(5)	2.5(1)

Table B-2. Anisotropic Displacement Parameters for **13**.

atom	**U11**	**U22**	**U33**	**U12**	**U13**	**U23**
I(1)	0.0309(3)	0.0405(3)	0.0303(3)	0.0043(2)	0.0102(2)	-0.0020(2)
Rh(1)	0.0205(3)	0.0254(3)	0.0255(3)	0.0010(2)	0.0047(2)	-0.0019(2)
O(1)	0.045(3)	0.026(2)	0.026(2)	0.003(2)	0.010(2)	-0.003(2)
N(1)	0.024(3)	0.029(3)	0.030(3)	-0.005(2)	0.004(2)	-0.001(2)
N(2)	0.031(3)	0.031(3)	0.024(3)	0.002(3)	0.006(2)	-0.002(2)
N(3)	0.023(3)	0.029(3)	0.028(3)	0.001(2)	0.005(2)	-0.001(2)
N(4)	0.027(3)	0.032(3)	0.025(3)	-0.004(2)	0.002(2)	0.001(3)
N(5)	0.021(3)	0.030(3)	0.028(3)	0.000(2)	0.005(2)	-0.003(3)
C(1)	0.039(4)	0.039(4)	0.048(4)	-0.009(4)	0.007(3)	0.002(4)
C(2)	0.025(4)	0.033(4)	0.034(4)	0.003(3)	0.001(3)	0.006(3)
C(3)	0.034(4)	0.040(4)	0.033(4)	0.004(3)	0.013(3)	0.005(3)
C(4)	0.034(4)	0.031(4)	0.032(4)	0.005(3)	0.011(3)	0.001(3)
C(5)	0.062(5)	0.052(5)	0.031(4)	-0.002(4)	0.014(4)	-0.004(4)
C(6)	0.035(4)	0.033(4)	0.049(4)	0.010(3)	0.010(3)	0.002(3)
C(7)	0.024(4)	0.032(4)	0.034(4)	0.003(3)	0.008(3)	0.008(3)
C(8)	0.021(4)	0.049(4)	0.037(4)	0.001(3)	-0.001(3)	0.011(3)
C(9)	0.028(4)	0.044(4)	0.030(4)	-0.011(3)	0.006(3)	0.002(3)
C(10)	0.039(4)	0.074(6)	0.032(4)	-0.009(4)	-0.002(3)	-0.001(4)
C(11)	0.033(4)	0.029(4)	0.030(4)	-0.002(3)	0.008(3)	-0.001(3)
C(12)	0.045(4)	0.025(4)	0.033(4)	0.002(3)	0.010(3)	0.001(3)
C(13)	0.031(4)	0.033(4)	0.037(4)	0.002(3)	0.008(3)	-0.014(3)
C(14)	0.036(4)	0.047(5)	0.048(4)	-0.002(4)	0.000(3)	-0.022(4)
C(15)	0.029(4)	0.053(5)	0.051(5)	-0.005(4)	-0.002(3)	-0.016(4)
C(16)	0.026(4)	0.033(4)	0.043(4)	0.005(3)	0.008(3)	-0.006(3)
C(17)	0.028(4)	0.024(3)	0.031(4)	0.001(3)	0.009(3)	-0.002(3)

Table B-3. Bond Lengths (Å) for **13**.

atom	atom	distance	atom	atom	distance
I(1)	Rh(1)	2.6649(6)	C(1)	C(2)	1.496(9)
Rh(1)	N(1)	2.053(5)	C(2)	C(3)	1.401(9)
Rh(1)	N(3)	2.043(5)	C(3)	C(4)	1.367(9)
Rh(1)	N(5)	2.056(5)	C(4)	C(5)	1.499(9)
Rh(1)	C(11)	2.109(7)	C(6)	C(7)	1.485(9)
O(1)	C(11)	1.362(7)	C(7)	C(8)	1.384(9)
O(1)	B(1)	1.447(8)	C(8)	C(9)	1.386(9)
N(1)	N(2)	1.352(7)	C(9)	C(10)	1.486(9)
N(1)	C(2)	1.342(8)	C(11)	C(12)	1.475(9)
N(2)	C(4)	1.346(8)	C(13)	C(14)	1.363(9)
N(2)	B(1)	1.567(9)	C(14)	C(15)	1.382(9)
N(3)	N(4)	1.382(7)	C(15)	C(16)	1.381(9)
N(3)	C(7)	1.337(7)	C(16)	C(17)	1.377(8)
N(4)	C(9)	1.346(8)	C(18)	C(19)	1.38(1)
N(4)	B(1)	1.542(9)	C(18)	C(20)	1.50(2)
N(5)	C(13)	1.358(7)	C(19)	C(20)	1.42(2)
N(5)	C(17)	1.354(7)	C(20)	C(21)	1.55(2)

Table B-4. Bond Angles (°) for **13**.

atom	atom	atom	angle	atom	atom	atom	angle
I(1)	Rh(1)	N(1)	176.0(1)	N(1)	C(2)	C(1)	124.6(6)
I(1)	Rh(1)	N(3)	94.0(1)	N(1)	C(2)	C(3)	107.9(6)
I(1)	Rh(1)	N(5)	91.5(1)	C(1)	C(2)	C(3)	127.5(6)
I(1)	Rh(1)	C(11)	89.2(2)	C(2)	C(3)	C(4)	106.6(6)
N(1)	Rh(1)	N(3)	84.9(2)	N(2)	C(4)	C(3)	107.9(6)
N(1)	Rh(1)	N(5)	89.3(2)	N(2)	C(4)	C(5)	122.3(6)
N(1)	Rh(1)	C(11)	94.5(2)	C(3)	C(4)	C(5)	129.7(6)
N(3)	Rh(1)	N(5)	172.6(2)	N(3)	C(7)	C(6)	122.9(6)
N(3)	Rh(1)	C(11)	84.6(2)	N(3)	C(7)	C(8)	108.6(6)
N(5)	Rh(1)	C(11)	100.4(2)	C(6)	C(7)	C(8)	128.4(6)
C(11)	O(1)	B(1)	120.0(5)	C(7)	C(8)	C(9)	107.2(6)
Rh(1)	N(1)	N(2)	118.4(4)	N(4)	C(9)	C(8)	107.4(6)
Rh(1)	N(1)	C(2)	133.3(4)	N(4)	C(9)	C(10)	123.4(6)
N(2)	N(1)	C(2)	108.1(5)	C(8)	C(9)	C(10)	129.1(6)
N(1)	N(2)	C(4)	109.5(5)	Rh(1)	C(11)	O(1)	109.7(4)
N(1)	N(2)	B(1)	116.9(5)	Rh(1)	C(11)	C(12)	116.6(5)
C(4)	N(2)	B(1)	133.6(5)	O(1)	C(11)	C(12)	111.1(5)
Rh(1)	N(3)	N(4)	116.2(4)	N(5)	C(13)	C(14)	122.9(6)
Rh(1)	N(3)	C(7)	135.8(4)	C(13)	C(14)	C(15)	119.2(6)
N(4)	N(3)	C(7)	107.9(5)	C(14)	C(15)	C(16)	119.2(6)
N(3)	N(4)	C(9)	108.9(5)	C(15)	C(16)	C(17)	118.7(6)
N(3)	N(4)	B(1)	118.3(5)	N(5)	C(17)	C(16)	122.9(6)
C(9)	N(4)	B(1)	131.2(6)	C(19)	C(18)	C(20)	119(1)
Rh(1)	N(5)	C(13)	120.1(4)	C(18)	C(19)	C(20)	125(1)
Rh(1)	N(5)	C(17)	121.8(4)	C(18)	C(20)	C(19)	116(1)
C(13)	N(5)	C(17)	117.1(5)	C(18)	C(20)	C(21)	117(2)

Chapter 5. Intersystem Crossing Dynamics of Diarylcarbenes in Liquid Xenon/Hydrocarbon Mixtures: A Search for Xenon-Carbene Complexes

Introduction

In 1962, Bartlett prepared and isolated the first example of a bound xenon complex, $[(XeF)(PtF_6)]$;[1] molecular xenon fluorides (XeF_n, n=2,4,6), xenon oxides, and several mixed oxofluorides were prepared soon afterward.[2] More recently, Frohn and co-workers employed xenon fluorides as precursors to prepare several compounds with Xe-C bonds, specifically linking Xe to perfluoroaryl and perfluorovinyl functionalities.[3,4] Formation of all of these species entails charge transfer from atomic xenon to a highly electronegative oxidant.

As discussed in previous chapters, xenon also binds transiently to low-valent, coordinatively unsaturated transition metal carbonyl complexes. The first such complexes were observed in 1975 by Perutz and Turner: photoextrusion of CO from Group 6 hexacarbonyls in Xe matrices led to formation of $(CO)_5M$-Xe species (M=Cr, Mo, W), which were characterized spectroscopically.[5] In the intervening years, analogous adducts have been observed in the gas phase[6,7] and in liquid and supercritical Xe solutions, with measured bond energies up to 11 kcal/mol.[8-14] Viewed within the hard/soft acid base framework,[15,16] these metal-Xe interactions are relatively soft, corresponding to covalent bonding between two highly polarizable electron-rich species (in the Xe fluoride compounds, the bonding has a “harder” or more ionic character). The Xe-metal bond results essentially from dative donation of xenon electron density into the LUMO of the transition metal carbonyl fragment.[17,18]

In this context, we sought to exploit the isolobal analogy between an unsaturated transition metal carbonyl fragment and a free singlet carbene (:CR_2), and thus to search for evidence of a discrete Xe-carbene interaction. To our knowledge, only one such adduct has been observed. In 1998, Sander and co-workers assigned an IR spectrum to the xenon adduct of difluorovinylidene (F_2C=C:), formed upon photoinduced isomerization of difluoroacetylene in a Xe-doped Ar matrix at 40 K. These authors support their assignment with *ab initio* calculations and characterize the species as "a charge-transfer complex with the Xe atom donating electron density to the in-plane vacant p-orbital of the vinylidene."[19,20] This sort of interaction is clearly similar to the bonding observed with transition metal carbonyl substrates. At the same time, difluorovinylidene is an exceptionally electrophilic species and may interact with Xe in a hard, ionic fashion. We wondered, more generally, what the scope of Xe interaction with carbenes might be.

Platz and co-workers have examined the behavior of *p*-nitrophenylchlorocarbene in Xe matrices and in Xe-saturated Freon and found no evidence of interaction with the noble gas.[21] This carbene, like difluorovinylidene, has a singlet ground state and could have exhibited spectroscopic shifts as a consequence of xenon binding. Rather than screening additional carbenes with singlet ground states, we elected to prepare ground state triplet carbenes in the presence of Xe. We anticipated that Xe would bind to these carbenes in their electronically excited singlet state; binding would then be perceptible kinetically through its impact on intersystem crossing (ISC) dynamics to the triplet ground state.

Chart 5.1

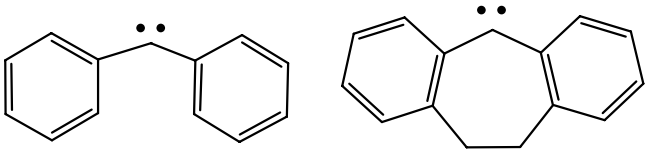

17 **18**

Eisenthal and co-workers have published systematic studies of the ISC rates of diphenylcarbene (**17**) and the related dibenzocycloheptadienylidene (**18**) (Chart 5.1).[22-26] The carbenes can be prepared in the singlet state by photoextrusion of N_2 from their diazo compound precursors, after which ISC to the triplet ground state occurs on a picosecond timescale. It was found that the singlet-to-triplet ISC rates of these carbenes vary inversely with solvent polarity, an effect attributed to a relative lowering of the singlet state energy in polar media.[24] This trend would suggest that ISC rates in the nonpolar medium of liquid Xe ought to be relatively high. However, stabilization of the singlet carbene by complexation with Xe should instead decrease ISC rates. This discrepancy offers a basis for detection of xenon-carbene interaction.

The above argument is somewhat complicated by a phenomenon termed the "heavy atom effect."[27] In many cases, the presence of xenon has been shown to enhance the efficiency of singlet-to-triplet ISC in neighboring molecules.[28-30] The phenomenon may be attributed to intensity borrowing by the transition of interest from a nonresonant xenon transition that benefits from the strong spin-orbit coupling between excited states of the heavy atom.[31] However, the enhanced rate is in general bounded by the rate associated with the oscillator strength of the transition in pure xenon, which is on the

order of 10^9 s^{-1}.[31] The ISC rates of **17** and **18** are on the order of 10^{10} s^{-1}, and thus heavy atom effect perturbations in this case ought to be minimal. Studies directed toward measuring the impact of Xe on the ISC rates of **17** and **18** are presented below.

Experimental Methods

Compounds **17** and **18** were accessed through photolysis of their diazo compound precursors. Both diphenyldiazomethane[32] and diazodibenzocycloheptadienylidene[33] were prepared by literature methods. The methodology for ISC measurements was in most respects the same as that used by Eisenthal.[24] Photolysis of the diazo compound at 266 nm led to formation of the singlet carbene. The rate of appearance of the triplet species was then monitored by $T_1 \rightarrow T_0$ laser-induced fluorescence (LIF) using 355 nm excitation of the nascent ground state triplet (emission λ_{max} = 500 nm). Pump and probe pulses (each 50-100 μJ) were generated from a passively mode-locked Nd:YAG laser (Ekspla model PL2143B, 10 Hz repetition rate) and directed collinearly through the copper cell (1.43 cm pathlength) described in Chapter 2. Figure 5.1 shows a schematic diagram. The beams were focused to a point approximately 10 cm past the cell so as to achieve a 1-2 mm beam diameter at the center of the sample. Fluorescence was collected along the transverse axis using a 2" f/1 lens and detected using a photomultiplier (PMT). A longpass filter (475 nm cutoff) was affixed to the front of the PMT to block scattered light from the laser pulses. Data were collected on an oscilloscope (LeCroy model 9310, 300 MHz), transferred to PC and fit to single exponentials using a commercially available nonlinear least squares routine (KaleidaGraph, Version 3.0, Synergy Software © 1996).

Time resolution was achieved by variable delay of the 355 nm probe pulse using a computer-interfaced translation stage (Physik Instrumente model M-535.22, 0.34 μm

precision). The stage position corresponding to time zero (i.e., precise temporal overlap of pump and probe pulses) was determined from a cross-correlation measured by detection of the LIF signal upon two-photon excitation of wet dioxane.[34] A fit of the cross-correlation (Figure 5.2) to a Gaussian curve (FWHM 23 ± 2 ps) indicates a 15 ps pulsewidth assuming Gaussian temporal intensity profiles of both pulses; it is likely that the actual pulsewidths were slightly longer (20-25 ps).[35]

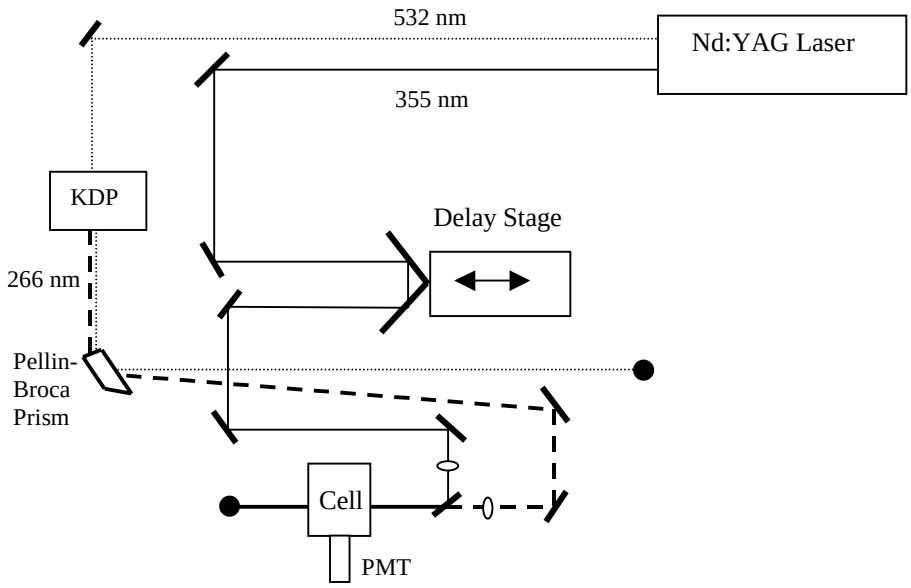

Figure 5.1. Schematic diagram of the apparatus used for picosecond ISC measurements.

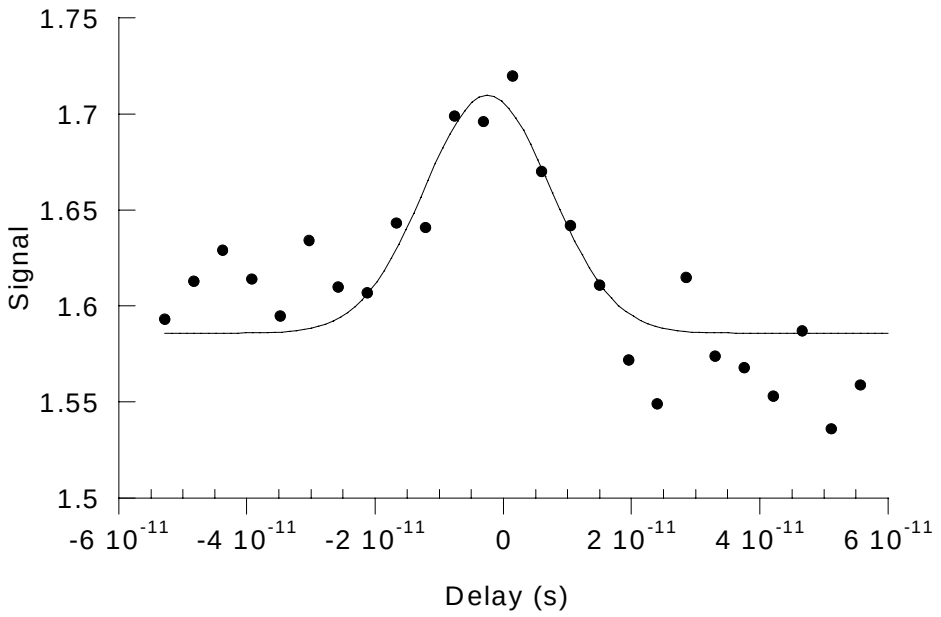

Figure 5.2. Cross-correlation of the 266 nm and 355 nm pulses. The solid line is a Gaussian curve (FWHM 23 ± 2 ps) fit to the data.

Results and Discussion

Dynamics studies of 17. Preliminary efforts were directed toward measurement of the ISC rate of diphenylcarbene (**17**) in the high-pressure cell. Studies by Eisenthal revealed a factor of 3 decrease in the rate of singlet-to-triplet ISC in **17** upon changing the solvent from isooctane (nonpolar) to acetonitrile (highly polar).[24] It was therefore anticipated that xenon might have a measurable impact on the rate. However, experimental exigencies precluded even an accurate reproduction of Eisenthal's measurements in alkane solvent.

The primary difficulty lay in the necessity of scanning the delay stage while photolyzing a very limited quantity of sample. The capacity of the cell employed in our

experiments is approximately 5 ml (flowing of the sample solution could not be implemented at the high pressures and low temperatures necessary for work in liquid Xe). Although solutions were stirred vigorously, it was common for products to build up in the beam path and on the cell windows, thus producing a background signal detrimental to kinetic measurements, which depended vitally on the assumption that the laser pulses impinge on identical sample at each stage position. Dilute solutions of diphenyldiazomethane (0.1-0.5 mM) were therefore employed to minimize product precipitation, and the pump pulse power was attenuated (<100 μJ) to conserve sample over the scan range of the stage. In Eisenthal's studies of **17**, 266 nm was employed as both the pump and probe frequency (due in all likelihood to the low absorption cross-section of **17** at 355 nm), but in our case the limited sample quantity precluded the use of a probe frequency that would lead to further dissociation of the precursor. All of these factors contributed to a signal-to-noise ratio too low for reproducible kinetic measurements.

Dynamics studies of 18. The cycloheptadienyl carbene **18**, which differs from **17** by the presence of an ethylene bridge linking the phenyl rings, exhibits a higher absorption cross-section at 355 nm than the diphenyl complex. Eisenthal and co-workers employed this lower frequency probe in their studies of **18**; significantly, the diazo precursor of **18** does not dissociate upon 355 nm irradiation. The drawback to the use of **18** in the present study is that the reported ISC rates for this carbene in 3-methylpentane and acetonitrile differ only by a factor of 1.3, leaving less margin for error in assessing the impact of Xe on the dynamics.

A kinetic trace of the formation of triplet **18** after photolysis of the diazo precursor at 266 nm is shown in Figure 5.3. The data were taken at room temperature with a precursor concentration of approximately 0.1 mM in 3-methylpentane. A single exponential fit to the trace affords a rate constant of 1.5 (± 0.2) x 10^{10} s^{-1}, in reasonably good agreement with the 1.66 x 10^{10} s^{-1} value measured by Eisenthal.[24]

We next measured the ISC rate of **18** in 3-methylpentane at –60 °C, the temperature at which liquid Xe experiments would be performed. The kinetic trace (Figure 5.4) was fit to a single exponential to afford a rate constant of 1.7 (± 0.3) x 10^{10} s^{-1}, within error of the room temperature measurement. Attempts to measure the ISC rate in pure liquid Xe, however, were unsuccessful. Data were irreproducible and poorly resolved from background signal. The most significant problem seemed to be background fluorescence stemming from precipitation of the carbene precursor on the cell windows during the process of introducing it into the cell (the process entailed addition of a pentane solution of the diazo compound via syringe followed by removal of the solvent *in vacuo*). It is possible, furthermore, that interaction of the probe-excited triplet carbene with xenon resulted in fluorescence quenching through the heavy atom effect, described earlier (*vide supra*).[36] In an effort to improve the signal-to-noise ratio, we elected to measure the ISC rate of **18** in a 3-methylpentane/liquid Xe mixture. Interpretable kinetic data were obtained using a 3:2 alkane/Xe mixture by volume. The trace is shown in Figure 5.5 and affords a rate constant of 1.7 (± 0.4) x 10^{10} s^{-1}, indistinguishable within error from the rate in the absence of xenon.

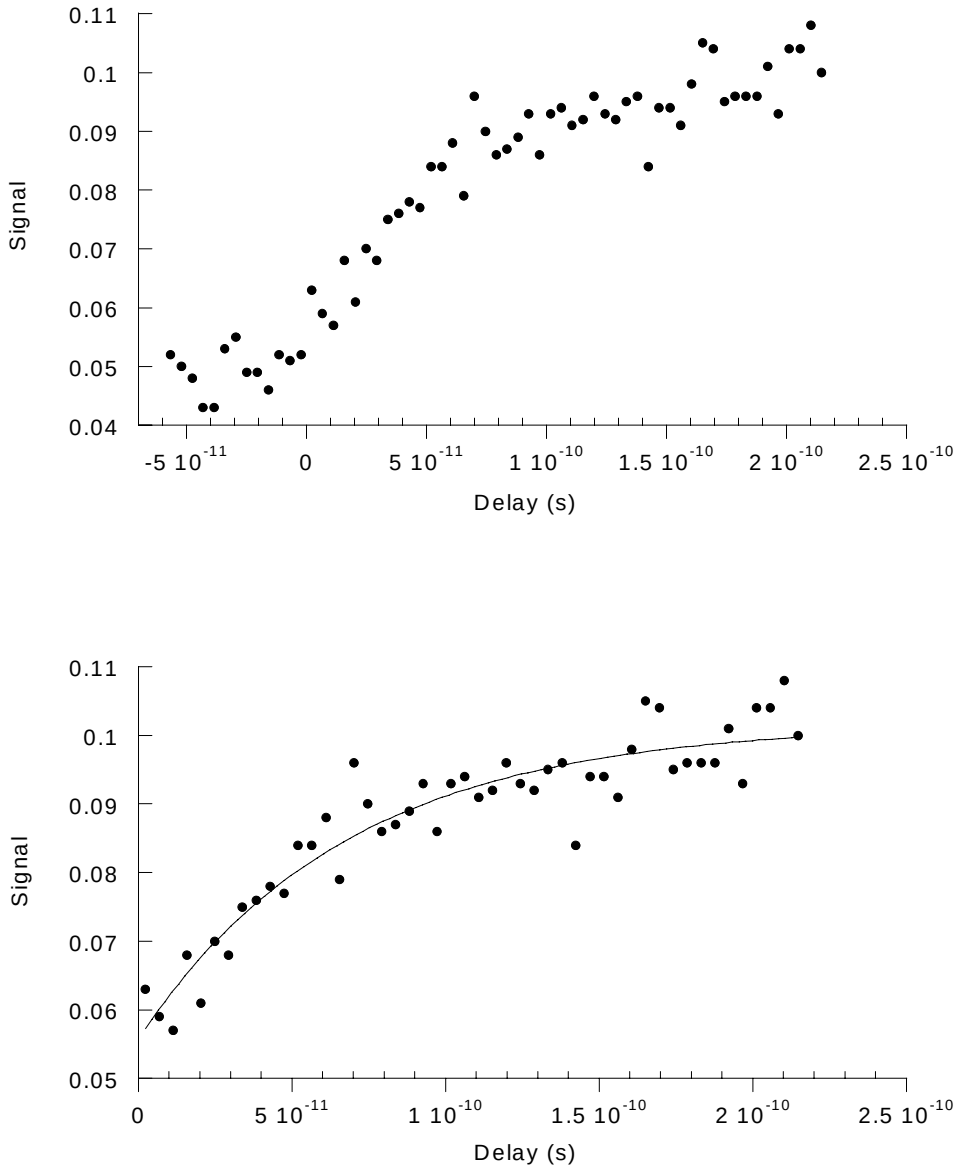

Figure 5.3. Plots of fluorescence signal vs. probe delay for appearance of triplet **18** in 3-methylpentane at room temperature. The bottom graph shows the same data fit to a single exponential (solid line), giving k = 1.5 (± 0.2) x 10^{10} s^{-1}.

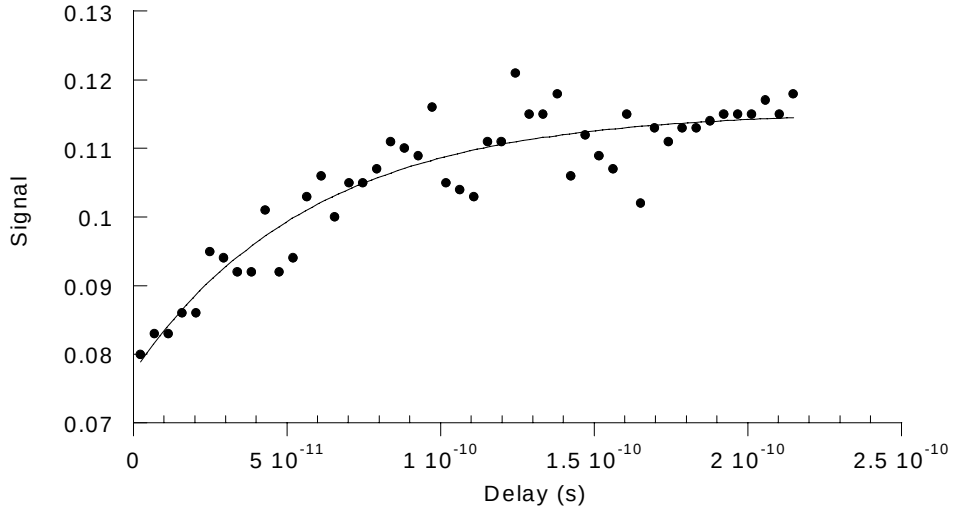

Figure 5.4. Plot of fluorescence signal vs. probe delay for appearance of triplet **18** in 3-methylpentane at –60 °C. The solid line is a single exponential fit giving $k = 1.7 (\pm 0.3) \times 10^{10}\ s^{-1}$.

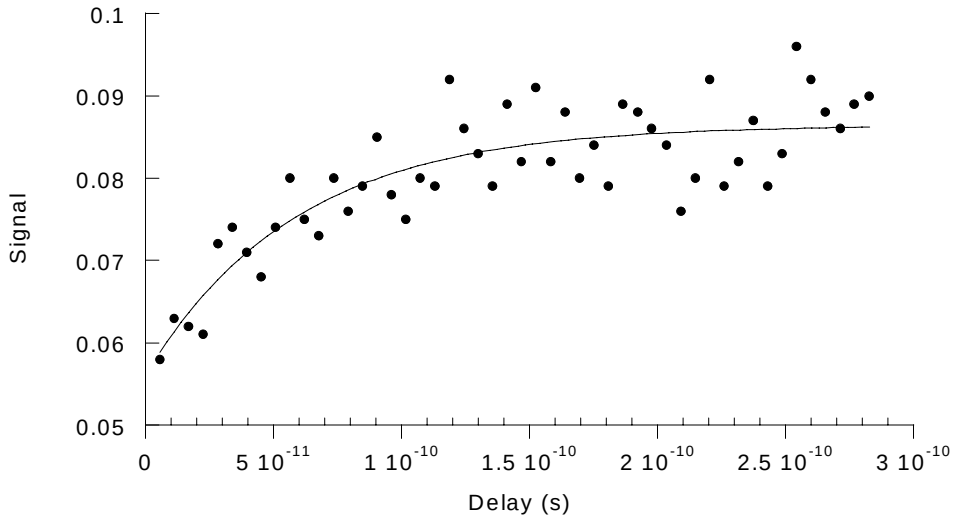

Figure 5.5. Plot of fluorescence signal vs. probe delay for appearance of triplet **18** in a 3:2 mixture of 3-methylpentane/Xe (l) at –60 °C. The solid line is a single exponential fit giving $k = 1.7 (\pm 0.4) \times 10^{10}\ s^{-1}$.

Conclusions

The above results are regrettably fairly inconclusive. The 15-20 % margins of error associated with the rate measurements preclude a sound judgment on the impact of added Xe in these experiments. As previously mentioned, the ISC rates of **18** in hydrocarbon and acetonitrile differ by only 30 %; consequently, xenon was not expected to alter the rate by more than 20 %, particularly in a solvent mixture. Detection of a Xe-carbene interaction in this context thus requires a greatly-improved signal-to-noise ratio, unlikely to be gained by switching detection modes from fluorescence to absorption. The most significant improvement in experimental design would be adoption of a high-pressure flow system to permit a larger sample reservoir and opportunity for extended signal averaging. At the same time, it is possible that unfluorinated carbenes simply lack the strong electrophilicity or high polarizability necessary for xenon binding.

Notes and References

1) Bartlett, N. *Proc. Chem. Soc.* **1962**, 218.

2) Cotton, F. A.; Wilkinson, G.; Murillo, C. A.; Bochmann, M. *Advanced Inorganic Chemistry*; 6th ed.; Wiley: New York, 1999.

3) Frohn, H.-J.; Bardin, V. V. *Chem. Commun.* **1999**, *10*, 919.

4) Frohn, H.-J.; LeBlond, N.; Lutar, K.; Zemva, B. *Angew. Chem. Int. Ed.* **2000**, *39*, 391.

5) Perutz, R. N.; Turner, J. J. *J. Am. Chem. Soc.* **1975**, *97*, 4791.

6) Jyo-O, M.; Takeda, H.; Omiya, K.; Ishikawa, Y.; Arai , S. *Bull. Chem. Soc. Jpn.* **1993**, *66*, 3618.

7) Wells, J. R.; Weitz, E. *J. Am. Chem. Soc.* **1992**, *114*, 2783.

8) Weiller, B. H.; Wasserman, E. P.; Bergman, R. G.; Moore, C. B.; Pimentel, G. C. *J. Am. Chem. Soc.* **1989**, *111*, 8288.

9) Weiller, B. H. *J. Am. Chem. Soc.* **1992**, *114*, 10910.

10) Weiller, B. H.; Wasserman, E. P.; Moore, C. B.; Bergman, R. G. *J. Am. Chem. Soc.* **1993**, *115*, 4326.

11) Schultz, R. H.; Bengali, A. A.; Tauber, M. J.; Weiller, B. H.; Wasserman, E. P.; Kyle, K. R.; Moore, C. B.; Bergman, R. G. *J. Am. Chem. Soc.* **1994**, *116*, 7369.

12) Sun, X. Z.; George, M. W.; Kazarian, S. G.; Nikiforov, S. M.; Poliakoff, M. *J. Am. Chem. Soc.* **1996**, *118*, 10525 and references therein.

13) Sun, X. Z.; Grills, D. C.; Nikiforov, S. M.; Poliakoff, M.; George, M. W. *J. Am. Chem. Soc.* **1997**, *119*, 7521.

14) Grills, D. C.; Sun, X. Z.; Childs, G. I.; George, M. W. *J. Phys. Chem. A* **2000**, *104*, 4300.

15) Parr, R. G.; Pearson, R. G. *J. Am. Chem. Soc.* **1983**, *105*, 7512.

16) Pearson, R. G. *J. Am. Chem. Soc.* **1988**, *110*, 7684.

17) For a theoretical treatment of the bonding in transition metal rare gas complexes, see this and the subsequent reference: Ehlers, A. W.; Frenking, G.; Baerends, E. J. *Organometallics* **1997**, *16*, 4896.

18) Hu, W.-P.; Huang, C.-H. *J. Am. Chem. Soc.* **2001**, *123*, 2340.

19) Kotting, C.; Sander, W.; Breidung, J.; Thiel, W.; Senzlober, M.; Burger, H. *J. Am. Chem. Soc.* **1998**, *120*, 219.

20) Sander, W.; Kotting, C. *Chem. - Eur. J.* **1999**, *5*, 24.

21) Platz, M. Personal Communication.

22) Dupuy, C.; Korenowski, G. M.; McAuliffe, M.; Hetherington, W. M. I.; Eisenthal, K. B. *Chem. Phys. Lett.* **1981**, *77*, 272.

23) Sitzmann, E. V.; Langan, J. G.; Eisenthal, K. B. *Chem. Phys. Lett.* **1984**, *112*, 111.

24) Langan, J. G.; Sitzmann, E. V.; Eisenthal, K. B. *Chem. Phys. Lett.* **1984**, *110*, 521.

25) Eisenthal, K. B.; Moss, R. A.; Turro, N. J. *Science* **1984**, *225*, 1439.

26) Eisenthal, K. B.; Turro, N. J.; Sitzmann, E. V.; Gould, I. R.; Hefferon, G.; Langan, J.; Cha, Y. *Tetrahedron* **1985**, *41*, 1543.

27) Turro, N. *Modern Molecular Photochemistry*; University Science Books: Sausalito, 1991 pp. 191-193.

28) Siegel, S.; Judeikis, H. S. *J. Chem. Phys.* **1968**, *48*, 1613.

29) Head, D. A.; Singh, A.; Cook, M. G.; Quinn, M. J. *Can. J. Chem.* **1973**, *51*, 1624.

30) Anderson, M. A.; Grissom, C. B. *J. Am. Chem. Soc.* **1996**, *118*, 9552.

31) Robinson, G. W. *J. Chem. Phys.* **1967**, *46*, 572.

32) Humphreys, R. W. R.; Arnold, D. R. *Can. J. Chem.* **1977**, *55*, 2286.

33) Moritani, I.; Murahashi, S.-I.; Yoshinga, K.; Ashitaka, H. *Bull. Chem. Soc. Jpn.* **1967**, *40*, 1506.

34) Lakowicz, J. R.; Gryczynski, I.; Nowaczyk, K. *Spectrochim. Acta A* **1997**, *53*, 1637.

35) The commercial specifications of the laser indicate a pulsewidth of 20-30 ps, based on measurement of the autocorrelation of the fundamental pulse (1064 nm) by second harmonic generation. This methodology offers improved signal-to-noise compared to

detection of dioxane fluorescence and therefore likely affords a more accurate pulsewidth value. Nonetheless, determination of time zero in the present experiment necessitated a UV/UV cross-correlation measurement, hence the method described in the text. For a discussion of autocorrelation and cross-correlation and their use in measuring pulse duration, see: Demtroder, W. *Laser Spectroscopy: Basic Concepts and Instrumentation*; 2nd ed.; Springer-Verlag: Berlin, 1998 pp. 627-630.

36) A possible quenching mechanism could involve Xe-enhanced ISC from T_1 to the lowest singlet state, followed by ISC to T_0. Note that this Xe quenching mechanism is unrelated to the fundamental question addressed in these experiments, i.e. interaction of Xe with the singlet carbene.